GRAN SASSO
SCIENCE INSTITUTE

Ph.D. programme in

Astroparticle Physics

Cycle XXXIV

Measurement of the cosmic p+He energy spectrum from 50 GeV to 300 TeV with the DAMPE space mission

Supervisor:
Prof. Ivan De Mitri

Ph.D. Candidate:
Francesca Alemanno

L'Aquila, thesis submitted in March 2023

Abstract

Recent observations of proton and helium in galactic cosmic rays (CRs) have revealed intriguing spectral features that motivate further direct measurements extending up to the multi-TeV energy region. Specifically, a first deviation (*hardening*) from the single power law describing the galactic CR spectrum has been found at hundreds of GeV, interpreted as a change in the diffusion coefficient. A second structure manifested by a spectral *softening* has been recently detected at tens of TeV although its origin remains unclear. Consequently, more measurements are needed in order to clarify the nature of such features.

Current-generation space-based detectors are well-suited for performing the aforementioned measurements. Specifically, DAMPE (DArk Matter Particle Explorer) was designed to study galactic cosmic rays up to hundreds of TeV (among its various scientific objectives) with extremely good energy resolution and excellent particle identification capabilities.

This thesis focuses on the spectral measurement of proton+helium in the energy range of 46 GeV to 316 TeV with the DAMPE detector. Combining proton and helium leads to increased statistics while maintaining an exceptional sample purity, as opposed to single proton or helium spectral measurements which are affected by cross-contamination and larger uncertainties at high energies (above 100 TeV). Moreover, the proton+helium measurement is also performed by ground-based experiments, although with large systematic uncertainties concerning the mass composition. Consequently, a direct measurement of the aforementioned spectrum from space, will provide a bridge between experimental results obtained with diverse techniques.

As a result of this work, a hardening feature at $\sim$600 GeV has been observed in the p+He spectrum, confirming previous direct observations. Then, at $\sim$26 TeV, a spectral softening has been found with an unprecedented significance of 6.7σ. This observation provides a valuable cross-check for the individual proton and helium analyses with increased statistics, while minimizing possible contamination effects. Finally, by measuring the energy spectrum up to 316 TeV, a strong link is established between space- and ground-based experiments.

Contents

Introduction

Throughout history, human beings always gazed at the night sky trying to give meaning to the small lights adorning the dark above us. The resulting interpretations have progressed from magical, religious, and philosophical reflections, to scientific explanations of celestial objects as other planets, burning stars, or complex, catastrophic events occurring hundreds of light-years distant from our planet. What we can easily perceive with our senses is the light that they emit or reflect but our innate curiosity could not be satisfied and we developed instruments to improve our vision and detectors to see the previously invisible. Despite our efforts, we have yet to explore the vast majority of our universe, and it is uncertain whether such exploration is even possible. Remarkably, what we can't reach, is coming to us. Every second numerous *messengers* are traveling across the cosmos, carrying precious information on the extreme phenomena taking place in unreachable corners of the universe. These messengers are manifested in the form of elementary particles, nuclei, and gravitational waves, which we are capable of detecting through the use of sophisticated instruments developed throughout the recent decades. The focus of this thesis is on messengers called *cosmic rays*, which have captured the attention of scientists over the last century.

Cosmic rays (CRs) are particles and nuclei accelerated in extreme regions of the universe. These particles can either originate inside our galaxy (GCRs) or outside of it, and they carry information about the astrophysical particle accelerators where they were generated and the interstellar medium through which they travel. Cosmic rays consist of various nuclear species and they cover the vast energy range up to 10^{20} eV, beyond the limits explored with human-made particle accelerators.

The CR energy spectrum deviates from the simple power law expected for accelerated particles and displays various unclear features, including the *knee*, a significant steepening of the spectrum at 3×10^{15} eV. Different hypotheses have been raised

to explain this feature, including the maximum energy attainable by galactic accelerators, but they have not been confirmed yet. It is thus essential to study the knee region to confirm or eliminate possible explanations. Last-generation ground-based experiments suggested a transition from light to heavy CRs showing a steepening of the light-element spectra, at energy $\sim$ 700 TeV. This value is below the result obtained by most of the previous measurements, at $\sim$ 3 PeV (i.e. at the all-particle knee). Further studies are thus necessary, as indirect measurements suffer from significant uncertainties, particularly regarding the mass composition. On the other hand, direct measurements are able to discriminate different nuclei with small uncertainties and they could clarify the dominating mass group in the knee region, but the exploration of this high-energy area is difficult to perform from space. Combining the light elements spectra (i.e. measuring the proton+helium spectrum), ground and space-based experiments can bridge their results and clarify possible scenarios. Light elements are indeed the most abundant GCR species, and their combination results in a significant increase in statistics. In addition, light GCRs can be a useful tool for studying the anisotropy of the CR distribution, since their trajectories are less affected by the Galactic magnetic field compared to heavier CRs.

Below $\sim$ 3 $\times 10^{15}$ eV (the knee energy), shock acceleration mechanisms predict a single power-law energy spectrum for GCRs, resulting in an $E^{-2.6}$ - $E^{-2.7}$ energy spectrum detected on Earth [1]. Nevertheless, several experiments have reported unexpected spectral features in protons, helium, and heavier nuclei in recent years [2–17]. The spectrum of GCRs becomes harder around several hundreds of GeV but softens again above 10 TeV [3, 9, 18], deviating from the expected single power law. These deviations inspire a need for a deeper understanding of CR acceleration and propagation mechanisms. While space-borne magnetic spectrometers such as PAMELA and AMS offer precise measurements of various CR species, they can only reach rigidities up to a few TV [11–17]. Previous generation space and balloon-borne experiments (e.g., CREAM, NUCLEON, ATIC [5–7]) have directly measured higher-energy cosmic rays, but their data suffer from significant statistical and instrumental uncertainties. In this context, additional precise direct measurements from new-generation instruments were needed, especially in the high-energy region of the GCR spectrum, where the picture is still unclear.

DAMPE (the DArk Matter Particle Explorer), is a calorimetric space-borne detector designed to search for signs of dark matter and observe cosmic rays. It is

operational since December 2015 and can detect e^-- e^+ and γ-rays up to $\sim$ 10 TeV, while reaching hundreds of TeV for protons and ions. The instrument is composed of four sub-detectors, including a plastic scintillator detector to distinguish between electrons and γ-rays and to measure the absolute charge of impinging particles, a silicon-tungsten tracker-converter for reconstructing the direction of charged particles and converting photons in electron-positron pairs, a bismuth germanium oxide imaging calorimeter for measuring the energy of particles and distinguishing between hadronic and electromagnetic showers, and a neutron detector for collecting neutrons from hadronic showers further refining the event identification. DAMPE has a large acceptance, a deep calorimeter, and good energy resolution ($\sim$1.5% for electrons and $\sim$30% for protons), making it suitable for measuring cosmic rays up to a few hundred TeV [19].

In this thesis, the energy spectrum for p+He up to $\sim$ 300 TeV is measured, using six years of data collected by the DAMPE satellite. By selecting a combined sample of protons and helium nuclei, the event selection criteria can be relaxed (with respect to the case of p alone or He alone) while keeping a low contamination, resulting in higher statistics and extending the energy range up to $\sim$ 300 TeV with remarkably good precision. This measurement is a valuable cross-check for the single proton and helium analyses, allowing measuring the softening structure at tens of TeV with unprecedentedly high significance, while also providing for the first time a bridge between space-based and ground-based results with small uncertainties. The results obtained with this work have been submitted for publication and can be found at [20].

As part of the efforts to explore the PeV energy region of the CR spectrum, in the framework of my Ph.D. project, I worked also on the HERD experiment [21], which aims to develop a space-based instrument for this purpose. Specifically, I focused on the simulation of the light production and propagation inside the plastic scintillator detector (PSD) bars using the GEANT-4 software. In the simulations, I tested various dimensions, scintillator materials, and wrapping materials for the PSD, as well as different positioning and sizes for the read-out sensors (Silicon Photomultipliers, SiPMs). I also simulated the response of the scintillator coupled with SiPMs to various particles, including cosmic muons, radioactive sources and particles from accelerated beams, and evaluated the hermeticity of the full HERD PSD. In addi-

tion, I contributed to laboratory measurements on the PSD, the assembly of the full HERD PSD prototype, and the test beam at CERN SPS, which provided valuable insights into the performance of the HERD experiment. These activities are not reported in this thesis, focusing here on the p+He spectral measurement with DAMPE data, which was the main project of my Ph.D. The HERD work resulted in several contributions to papers, as well as presentations in conferences and collaboration meetings, as reported in Appendix D.

The work on the p+He measurement will be presented in four chapters and appendices briefly summarized here below.

- In the first chapter CR physics will be briefly introduced. The starting point will be a historical overview, followed by the theories formulated to explain sources and acceleration mechanisms of CRs in our galaxy, continuing with the expected and measured energy spectrum and CR composition, revealing the stellar origin of CRs and suggesting their diffusive propagation in the interstellar medium. Afterwards, the CR detection techniques will be briefly portrayed, characterizing direct and indirect measurements, and addressing the strength and weaknesses of the two approaches. Finally, a report of the main results regarding the study of the light CR component, namely proton and helium, will be given, presenting the most recent unexpected features detected in the two spectra. The final part of the chapter will review the results of the combined p+He energy spectrum measured by both ground- and space-based experiments and will follow up with a concluding section explaining the motivations behind the combined light component (p+He) study made in this thesis.

- This work is based on the measurement made using the DAMPE detector, therefore a description of the experiment will be given in the second chapter. This part will open with a list of the main scientific goals, followed by a characterization of the full DAMPE instrument, going to the specifics of each sub-detector. Afterwards, the method employed for the data acquisition and the trigger logic will be introduced, continuing with the presentation of the software used for data processing and MC simulations. The second chapter

ends with a review of the main results achieved by the DAMPE experiment regarding its primary scientific objectives.

- The third chapter will focus on the selection of proton+helium nuclei, using the data detected with the DAMPE satellite. Specifically, it will begin with a description of the sample used in the analysis including real events and a list of MC simulations. The selection procedure will be thoroughly described, from the classification of good-quality CR events up to the identification of p+He candidates. The efficiency of the applied selection cuts will be evaluated resulting in the effective acceptance, presented in this chapter as well. Finally, the contribution from possible backgrounds entering the selected p+He data sample will be evaluated.

- With the events of interest being defined in the third chapter, the fourth chapter is dedicated to what concerns the p+He energy spectrum. The starting point will be the energy measurement method, discussing identified problems and valid solutions, leading to the reconstruction of the primary particle energy and the measurement of the p+He energy spectrum. A detailed discussion of the statistical and systematic uncertainties will follow, characterizing all the possible contributions and including them in the final result. The closing part of this work will see the result on the p+He energy spectrum, including the statistical and systematic uncertainties, the study of its most distinctive feature through a fit and a cross-check with other DAMPE measurements on the proton and helium spectra. Finally, a comparison with other direct and indirect p+He experimental results will be presented and analyzed.

- Appendices will follow. Two of them include a series of figures intended to clarify and better understand some steps of the analysis. The other one describes a method used in the energy reconstruction procedure, fundamental to reach the high energy of 300 TeV with the DAMPE detector. Finally, my Ph.D. activities will be reported in the last appendix.

Chapter 1

Cosmic Rays and measurements of light nuclei

From their discovery more than 100 years ago until today, cosmic rays revealed unexpected properties of the smallest and the biggest components of our universe, guiding the way toward understanding fundamental particle physics and astrophysics phenomena. Regardless of the numerous breakthroughs in CR physics resulting from constant advancement in measurement precision, many peculiarities of these particles and nuclei are still unclear. Recent results demonstrated that the more we advance our knowledge of CRs, the more they can amaze us, opening new challenges while providing answers. It is thus fundamental to keep exploring the experimental and theoretical side of the CR endeavor.

This chapter will be starting with the historical facts from the discovery of CRs up to the first ground-based detector arrays and space-borne instruments, continuing with a description of candidate sources, acceleration and propagation theories, along with a discussion on the CR composition, the energy spectrum and its features. An explanation of detection techniques will follow, before concluding with the study of the light CR component (proton, helium and p+He), reporting the most recent results and the motivations behind the p+He study.

1.1 Historical overview

The history of Cosmic Rays (CRs) starts at the beginning of the 20th century, a few years after the discovery of radioactivity. The initial hint of their presence

was provided by measurements of ionizing radiation made with electroscopes, which were discharged for unknown reasons. In the beginning, the aforesaid phenomenon was attributed to the presence of radon in the air, which was a well-known natural source of γ-rays. The confutation of this hypothesis was presented in 1912 by Victor Hess who measured the ionizing radiation up to more than 5 km altitude during his balloon flights. Using an electroscope, he demonstrated that the ionization rate increases with increasing altitude, suggesting an extraterrestrial origin of the observed radiation [22]. Similar evidence had been found the year before by Domenico Pacini, who measured a decreasing radiation rate while going deeper underwater [23]. However, his results didn't have great resonance and the discovery of CRs was attributed to Victor Hess, with the subsequent win of the Nobel Prize in 1936 (after Pacini's death). The term "cosmic rays" was given by Robert Millikan who believed CRs were γ-rays of cosmic origin and can be dated back to these days. In the following years, more balloon flights were performed up to 16 km altitudes highlighting a drop in the ionization rate when surpassing a certain elevation, which led to the identification of the previously detected radiation as constituted by secondary particles, generated by primary CRs interacting in the Earth's atmosphere. Later on, Blackett and Occhialini collected pictures of particles interacting in cloud chambers revealing the charged nature of the cosmic radiation by evaluating their deflection in a magnetic field [24]. Thereupon, the matter-antimatter theory of Dirac was also confirmed with the first observation of a positron in a cloud chamber made by Anderson in 1932 [25], who consequently obtained the Nobel Prize, shared with Hess, in 1936. More physicists fascinated by the newly discovered particles carried out experiments aiming at further investigation and comprehension of cosmic radiation. Among these, Bruno Rossi discovered that CRs are mostly constituted by positively charged particles through the investigation of their deflection in the geomagnetic field [26]. Additionally, he found out that primary CRs generate showers in the atmosphere by putting in coincidence detectors covering large areas. Afterwards, Pierre Auger performed more detailed studies on *extensive air showers* (EAS) using detector arrays [27].

In the meantime, also the theoretical perspectives of CR research were flourishing, attracting the interest of many physicists of the period (more details will be given in the next section).

Besides investigating cosmic radiation from the ground, scientists wanted to go

beyond their limits by exploring the universe from a different perspective: in the political climate of the Cold War, the first artificial satellite, *Sputnik* (which is the Russian term for satellite), was sent to space by the Soviet Union on the 4th of October 1957, opening the era of space exploration. One month later, on the 3rd of November 1957, the Sputnik II was sent to space, with on board the dog Laika, the first living being in space, also carrying scientific instruments to measure UV, X-rays, and cosmic rays (Geiger tube). The first space-based CR observations were then made and a new age of space exploration (which is nowadays still far from its limit) began.

The floor was open for conceiving and realizing new experiments both ground- and space-based, along with visualizing and formulating specific models aiming to clarify the nature of cosmic particles.

1.2 Candidate sources and acceleration mechanisms

In 1934 the theory of CRs generated and accelerated in Supernova (SN) explosions was proposed for the first time [28]. The theory was based on the following assumptions: the rate of SN explosions in the Galaxy is 1 over ~ 100 years and the energy released is of $\sim 10^{51}$ erg per SN event. Given the estimated CR energy density of $\sim 3 \times 10^{40}$ erg s^{-1}, it could be efficiently produced by a SN explosion simply assuming that 10% of the energy released would provide accelerated particles [29]. This idea was quantitatively formulated by Fermi in 1949-54 [30, 31] (the so-called 2^{nd} order Fermi mechanism) and later framed independently in 1977-78 by several scientists [32–35] (called 1^{st} order Fermi mechanism).

Second order acceleration mechanism

The idea formulated by Fermi is based on the consideration that energetic particles could encounter magnetized moving clouds and change their direction of motion by scattering on the irregularities of the magnetic field, as shown in Fig. 1.1. The resulting particles' energy will be larger or smaller after every scattering depending on the dynamics of the collision (head-on or tail-on). On average, head-on collisions are more probable than the tail-on, causing a gain in energy after many particle-cloud interactions. The average energy gain will be $\sim (\Delta E/E) = (4/3)(V/c)^2$, where V represents the clouds' velocity and c the speed of light. The velocity of the clouds

is in general much smaller than the speed of light, meaning that the resulting acceleration in this formulation is very slow.

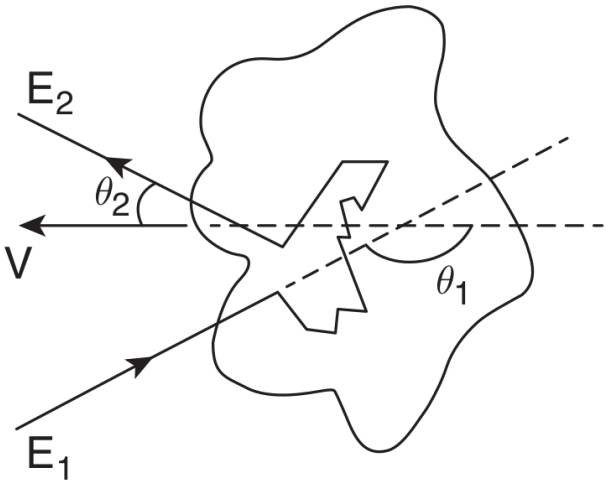

Figure 1.1: Representation of acceleration in magnetized moving clouds. A particle with initial energy E_1 enters a magnetized cloud, undergoes multiple scatterings on the magnetic field irregularities inside the moving (with velocity V) cloud and exits with energy $E_2 > E_1$. Picture taken from [36].

First order acceleration mechanism

When a SN explosion is considered, the shock front with magnetic inhomogeneities on both sides represents what was a magnetic cloud in the previous formulation of the theory. The particles will gain energy in an analogous way, by crossing the shock front, as illustrated in Fig. 1.2. However, the velocity of the magnetic irregularities will be negligible with respect to the velocity of the fluid both upstream and downstream (the two sides of the shock). If the reference frame of the shock is considered, a particle moving from downstream to upstream or in the opposite direction will always see the fluid on the other side of the shock moving slower. Consequently, the particle crossing the shock will always undergo head-on collisions with the fluid on the opposite side of the shock. The gain of energy, in this case, is much faster than in the previous case and it is $(\Delta E/E) \propto (V_S/c)$, with V_S indicating the shock velocity. The energy gain is now linear with energy, and for this reason, this acceleration mechanism has been labeled as "Fermi I", in opposition to the previous one, where the energy gain is of the second order in V/c, called "Fermi II".

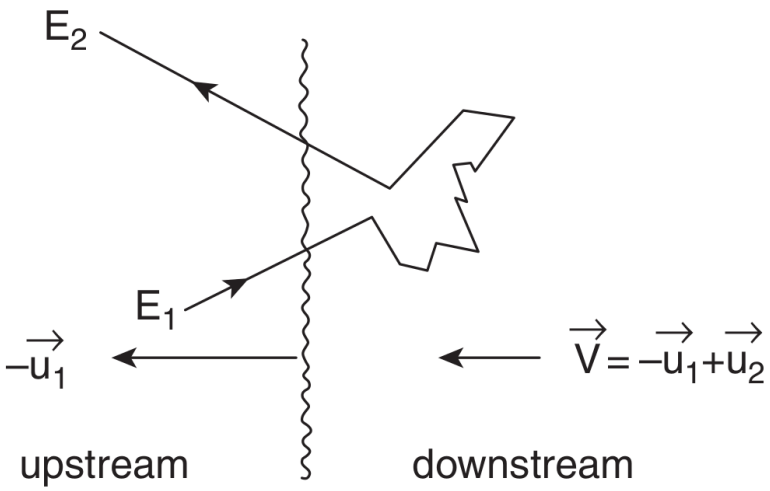

Figure 1.2: Representation of acceleration at the shock front. The shock moves with velocity u_1, while the fluid downstream has a velocity $V = u_2 - u_1$. The particles cross the shock with initial energy E_1 and final energy $E_2 > E_1$. Picture taken from [36].

Expected cosmic ray energy spectrum

The acceleration mechanisms previously described imply a power law energy spectrum with a single slope for cosmic particles. Specifically, the number of particles N with a given momentum p experiencing the shock acceleration process can be expressed as

$$N(p) \propto p^{-\gamma_p}, \tag{1.1}$$

with

$$\gamma_p = 3R_T/(R_T - 1), \tag{1.2}$$

where $R_T = u_1/u_2$ is the compression ratio of the shock, with u_1 and u_2 representing respectively the fluid velocities upstream and downstream of the shock. The compression factor can also be expressed, using the Rankine-Hugoniot relations, as:

$$R_T = \frac{4M_s^2}{3 + M_s^2}, \tag{1.3}$$

where M_s is the shock Mach number, $M_s = u_1/c_{s1}$, with $c_{s1} \approx 10\sqrt{\mathrm{T}_4}$ km/s sound speed in the Interstellar Medium (ISM) with temperature in units of 10^4 K. If a strong shock ($M_s \gg 1$) is considered, this would imply $R_T \approx 4$ and therefore $\gamma_p = 4$. To obtain the slope in energy γ_e, starting from the obtained slope in momentum

γ_p, the following formula can be used for relativistic particles ($E \gg mc^2$):

$$E^{-\gamma_e} dE \propto 4\pi p^2 p^{-\gamma_p} dp. \tag{1.4}$$

The outcome is what is expected for cosmic rays up to $\sim$ PeV energies, i.e. $\gamma_e = 2$, considering that propagation effects (see later) will give an additional contribution of ~ 0.7 to the spectral index.

Beyond the standard SN paradigm

Following the assumptions described above, the maximum achievable energy for CRs accelerated from SN explosions is of $E_{max} \leq 1$ GeV, which is definitely not sufficient to account for the observations. It follows that some other process should be considered. Recent observations proved that the magnetic field near the shock is amplified by a factor $\sim$ 10-100, which makes the acceleration possible up to $\sim$ 100 TeV-1 PeV energies. Additionally, assuming that SNRs are the main sources of galactic CRs, $\sim 10\%$ of the blast wave kinetic energy should go into accelerated particles which requires the formulation of new theories that are able to give a better description of the observations. Consequently, the so-called Non-Linear Diffusive Shock Acceleration (NLDSA) with Magnetic Field Amplification (MFA) theory has been proposed and developed. More information on this topic can be found in [1] and references therein.

In this context, experimental measurements are crucial to determine the maximum energy reachable by cosmic accelerators (for different nuclear species) eventually confirming the predictions and shedding light on cosmic ray properties.

1.3 Propagation in the Galaxy and composition

Another fundamental question on the nature of cosmic radiation is what are CRs made of. Direct measurements made with space-borne instruments allow for the separation of different galactic cosmic ray (GCR) nuclear species. An example is given in Fig. 1.3, where the measured GCR composition is compared with the solar system one, providing a clear indication of the stellar origin of cosmic particles, considering the similarity in the element's abundance. However, it can be noticed that some elements are more numerous in GCRs than in the solar system (e.g. Li,

Be, B, Mn, V, Sc, ...): they are identified as *secondary* CRs, produced from *primary* CRs (e.g. C, O, Fe, ...) through the fragmentation or spallation processes.

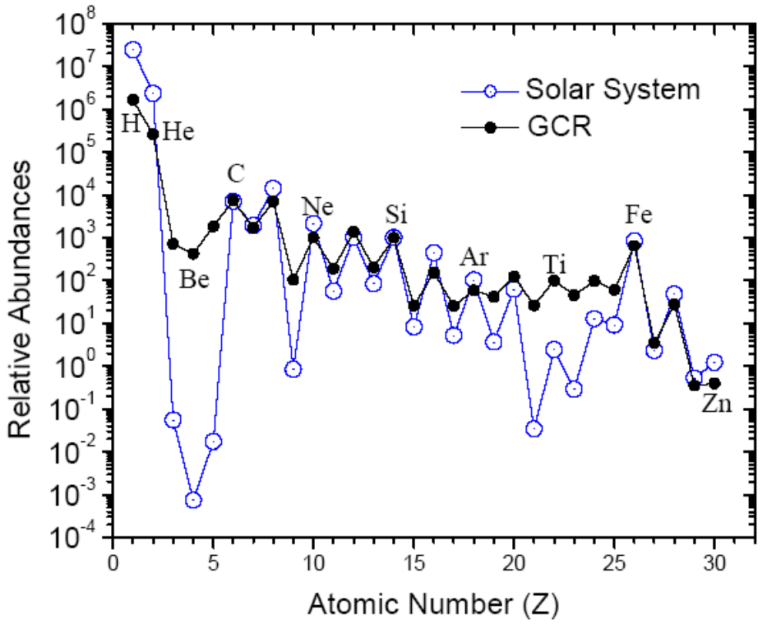

Figure 1.3: Galactic cosmic ray and solar system material abundances, normalized to Silicon (Si=10^3), at 1 GeV/n [1].

The observed primary-to-secondary ratios (such as B/C), demonstrate that GCRs propagate in a diffusive way. If the propagation was ballistic, CRs would escape from the Galaxy in a shorter time than the one needed to justify the observations. From the experimental results, it's also evident that the traversed grammage decreases with increasing energy, which implies also less time spent in the Galaxy for highly energetic particles. To conclude, measuring secondary-to-primary ratios provides an indication of the way CRs propagate and also of the grammage they traverse before leaving the Galaxy.

1.4 The energy spectrum and its features

Cosmic rays' precise measurements provided crucial information about the nature of these particles. The main result is represented by the measurement of the cosmic ray spectrum (in Fig. 1.4), which covers an energy range extending from a few GeV to $\sim$ 100 EeV. In the low-energy part, the spectral shape is characteristic of thermal emission and it is attributed to the influence of the Sun. From tens of

[1] https://izw1.caltech.edu/ACE/ACENews/ACENews83.html

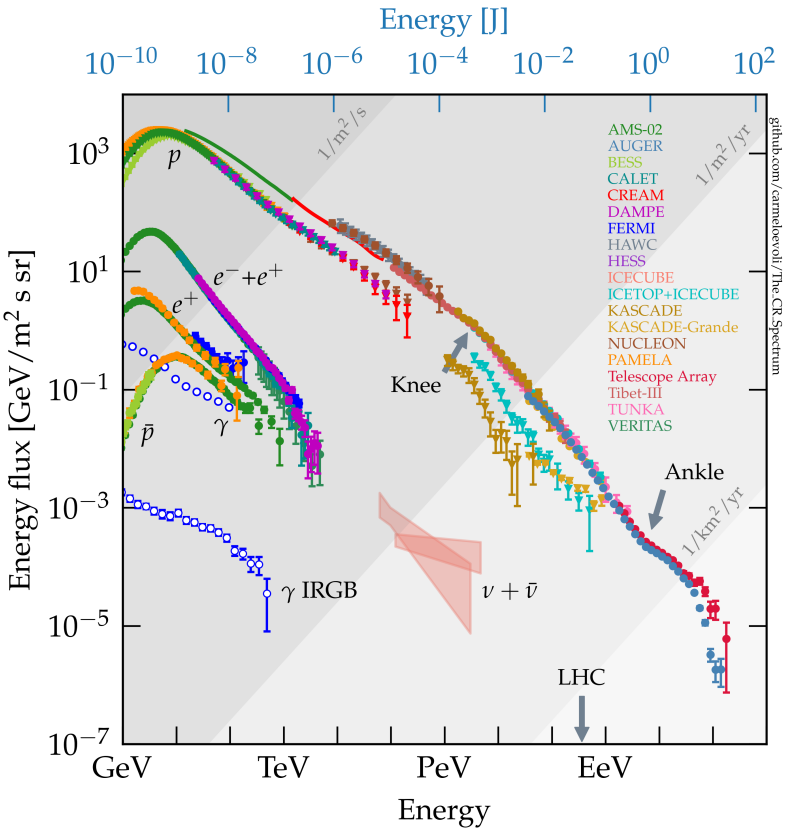

Figure 1.4: Cosmic ray energy spectrum [37].

GeV onward, the power-law shape indicates the presence of an acceleration process, meaning that these particles are produced and accelerated in astrophysical objects (such as SN) either inside or outside our galaxy. The power-law part of the spectrum is characterized by two distinctive features: the so-called *knee* at $\sim$ 3 PeV, where there is a change of spectral index from $\sim$ -2.7 to $\sim$ -3.1 and the *ankle* at $\sim$ 5 EeV where the spectrum becomes harder and then softer again (see Fig. 1.4). The power-law energy spectrum illustrates a particle's abundance that is decreasing with increasing energy. Consequently, at low energies (up to $\sim$ hundreds of TeV) it is possible to have good-quality measurements using relatively small detectors (order of m^2) while in the high energy region, in order to have significant results, big detectors (or detectors' arrays) covering large surfaces ($\sim$ km^2 and more) are needed. Such a diverse flux implies that at low energy it is possible to have more precise measurements and to separate different particles by measuring them directly in space, while from the sub-knee region onwards, the experiments are located at ground and CRs are measured after their interaction with the Earth's atmosphere, making their energy reconstruction and particle's identification more difficult.

1.5 Detection techniques

In the low energy part of the spectrum (up to tens of TeV), CRs are measured directly by means of space-based instruments or high-altitude long-flying balloons. As the energy increases, the CR flux becomes lower, making the direct measurements hard or even impossible (considering current technologies). It follows that extended arrays of CR detectors are used to perform indirect measurements from ground. These experiments observe extensive air showers (EAS) developing in the atmosphere to infer the properties of the primary particles, using different techniques. Several experiments were operated over the years in order to investigate and clarify different aspects of cosmic ray physics. Direct measurements have the advantage of measuring the primary particles before they interact with the Earth's atmosphere but are limited by their small exposure due to payload dimensions and weight constraints. On the other hand, indirect measurements can be performed on large areas, allowing to measure CRs up to the highest energy (where the flux is very low), but they cannot achieve the same precision as direct measurements in determining the spectra of individual nuclei. Furthermore, detecting EAS means relying on simulations that, in most cases, are not yet verified in the energy range and kinematic region of interest. Specifically, man-made accelerators are not able to reach the energy of the highest CRs, and the interactions and cross-sections of various nuclei (even at lower energies) haven't been investigated with good precision and in the very forward direction. Thus, the hadronic interaction models used to describe the particle's interactions and the EAS development in the atmosphere, sometimes differ in their predictions leading to large uncertainties in the determination of the CR spectra. In the following sections, some experiments relevant to the work presented in this thesis will be introduced separating direct and indirect measurements.

1.5.1 Direct measurements

Previous generation direct CR detectors provided information on the spectra of different nuclei up to tens of TeV. This energy limit was overcome by current generation experiments (e.g. DAMPE, described in the next chapter) which are able to achieve hundreds of TeV energy. Looking at the future, direct CR detectors could reach PeV energies, thus approaching the knee region (e.g. HERD [21, 38]). They

are divided into spectrometers, measuring the particle's rigidity, and calorimetric experiments, measuring the kinetic energy of incoming particles. The advantage of spectrometers is the better accuracy in the low rigidity range but, since these instruments are limited by the maximum detectable rigidity, they can reach only up to a few TeV energy per nucleon, considering current technologies. On the other hand, calorimetric experiments are able to measure CRs up to tens of TeV but their results are affected by the uncertainties coming from the hadronic interaction model used in the shower reconstruction. In the next section, some direct-detection experiments will be briefly described and their results on the light component (p+He) energy spectrum will be reported.

1.5.2 Indirect measurements

Indirect measurements are usually performed by combining different experimental techniques (summarized in Fig. 1.5) in order to get more information on the shower generated in the Earth's atmosphere. Ground-based experiments also try to estimate the CR composition by using one or more characteristics of the EAS, such as the number of muons or the longitudinal development of the shower and others. These results are affected by the poor mass resolution and large uncertainties mainly coming from the chosen interaction models. Nonetheless, several experiments reported results on the spectra of different CR mass groups including the combined light component (p+He). These experiments and their results on p+He will be presented in the next section.

1.6 Study of the light CR component

The most abundant component of CRs is represented by proton and helium nuclei (as shown in section 1.3). It follows that the study of these nuclei could aid in answering open questions on the CR nature. Recent results on the proton and helium spectra will be shown in this section, along with the status of the combined proton and helium spectral measurements and a description of the experiments that provided the p+He results. Finally, the motivations for studying proton and helium together will be illustrated.

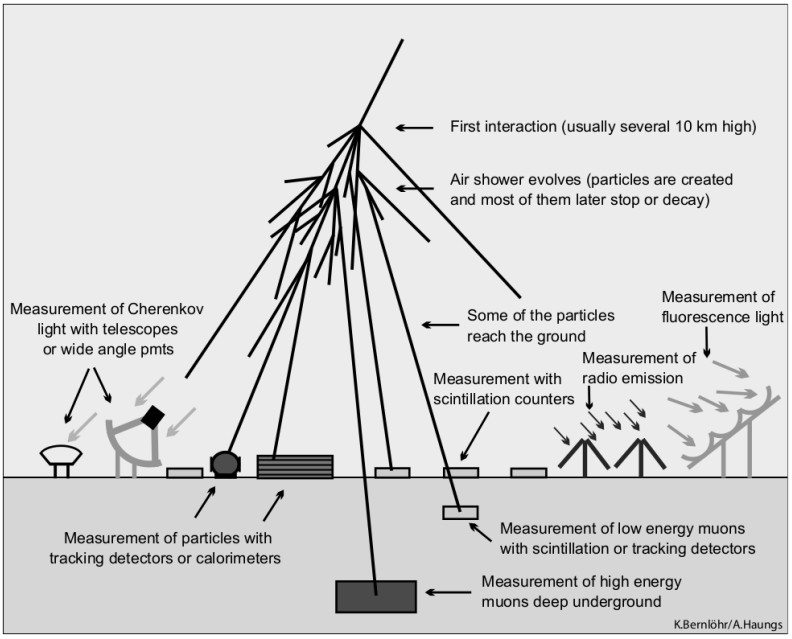

Figure 1.5: Several experimental techniques used on the ground for the study of extensive air showers [39].

1.6.1 Results on proton and helium spectra

In recent years, precise measurements made by space-based experiments showed interesting results on the proton and helium spectra. In particular, the deviation from the single power-law energy spectrum above tens of GeV is now confirmed. First, a hardening structure at $\sim$ hundreds of GeV has been found and confirmed by several experiments in both the proton and helium spectra [2–6, 9–17, 40]. Second, a softening feature was recently detected by the DAMPE experiment in the proton spectrum at $\sim$ 14 TeV [3] later confirmed by the CALET collaboration [18]. Moreover, a similar softening structure has also been found in the DAMPE helium spectrum, at $\sim$ 34 TeV [9]. The novel results on the softening opened new challenges in understanding the CR nature, guided by the recent DAMPE p and He spectra (shown in Fig. 1.6 and 1.7, compared with other direct measurements made by space-based experiments), proposing a possible rigidity-dependent feature, even though this is not yet a definitive answer considering the statistical and systematic uncertainties associated to the measurement. In the next chapter, the DAMPE experiment will be described and additional details on the achieved results will be illustrated.

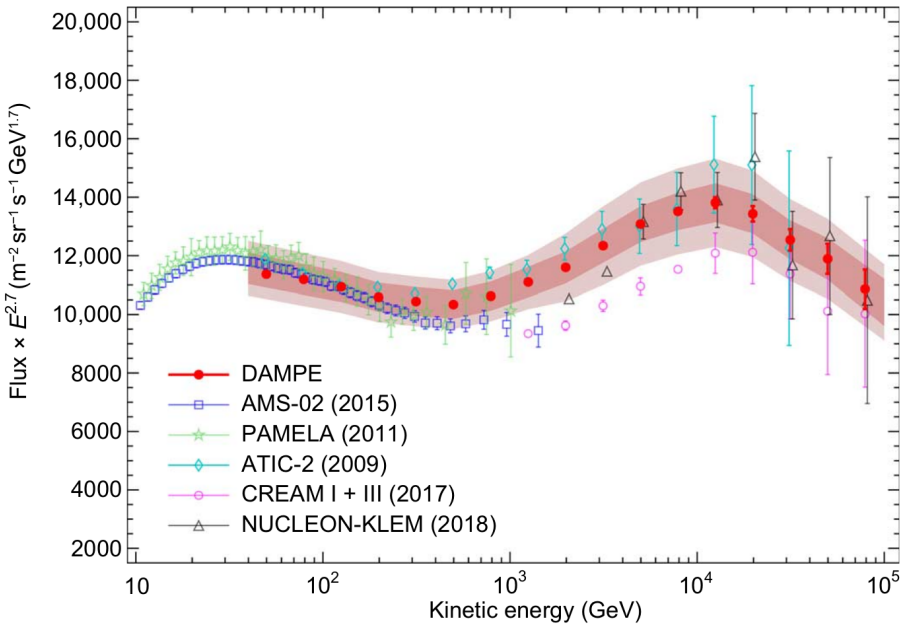

Figure 1.6: The DAMPE proton spectrum is shown with red-filled circles compared with other experiments' results. Statistical uncertainties are represented by error bars, and the systematics are divided into two bands: the outer band including all the contributions, and the inner band without the uncertainties coming from the chosen hadronic interaction models (which are the dominant ones) [3].

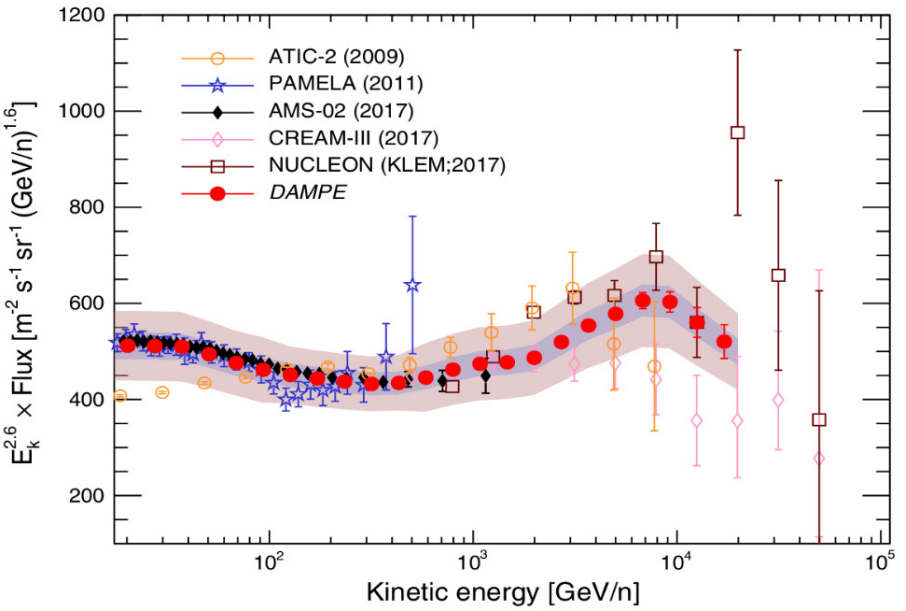

Figure 1.7: The DAMPE helium spectrum is presented with red-filled circles, compared with other experimental results. Error bars indicate the statistical uncertainties, while the systematic uncertainties are shown with the outer band for all the systematic uncertainties and the inner band excluding the ones on the hadronic interaction model [9].

1.6.2 The p+He spectrum: previous results

Proton and helium can be reasonably separated using direct-detection techniques, with a high energy limit of tens of TeV because of experimental limitations and low statistics. These limitations can be (partially) overcome by combining the two nuclei in a single spectrum (p+He). Indeed, selecting the two nuclei together means an increase in statistics and lack of cross-contamination which affects the single proton and helium spectra, thus allowing the extension to higher energy by space-based instruments. Moreover, if proton and helium are combined, ground-based experiments are less affected by limitations given by models and simulations making them able to provide their combined spectral measurement, thus separating light from medium- or high-mass nuclei. The p+He spectrum measured with several detectors (briefly described below) is presented in Fig. 1.10 and 1.11. As can be seen, direct and indirect CR detection could overlap in the energy region from tens of TeV to hundreds of TeV, which needs to be better explored with more precise measurements.

ATIC

ATIC was a balloon experiment that aimed at measuring CRs with charge Z between 1 and 28 in the energy range from tens of GeV to $\sim$ 100 TeV. ATIC was instrumented with a silicon matrix used to measure the particle's charge, a graphite target (0.75 nuclear interaction lengths) in which hadronic showers were produced, three layers of scintillator strips reconstructing the track, and additionally used as trigger, and finally, a BGO crystal calorimeter of 18 radiation lengths measuring the particle's energy [7].

NUCLEON

NUCLEON was a payload of the Russian satellite Resource-P 2, designed to study CR spectra from protons to zinc in the energy range from $\sim$ 100 GeV to $\sim$ PeV. NUCLEON used two methods for measuring the particle's energy: (a) an ionization calorimeter, and (b) a kinematic method (called Kinematic Lightweight Energy Meter, KLEM), measuring the number of secondary particles produced after the interaction of a particle with a spectrometer. The detector was composed of two planes of charge measurement system, a carbon target, six planes of energy

measurement system (with KLEM), three planes of trigger system (employing a scintillator), and a small aperture calorimeter [6].

CREAM

CREAM was a balloon-borne experiment that was launched several times from McMurdo, Antarctica, to circumnavigate two or three times the South Pole and to measure cosmic ray elemental spectra. The detector components are shown in the scheme in Fig. 1.8, where the redundancy and complementarity of sub-detectors for charge and energy measurement are evident. Specifically, the CREAM experiment was instrumented with a Timing Charge Detector (TCD) at the top, followed by a Transition Radiation Detector (TRD), a Cherenkov Detector (CD), and a few sub-detectors constituting the calorimeter module: a Silicon Charge Detector (SCD), carbon targets, scintillating fiber hodoscope (S0/S1 and S2), and an ionization calorimeter (W-scn) [5]. The configuration described above (and shown in Fig. 1.8) represents the first CREAM detector (CREAM-I). Other payloads followed, with their generation indicated by a Roman number. Specifically, from CREAM-II to CREAM-V the configuration was similar but the TRD was removed and an aerogel Cherenkov detector (CherCam) was added [10]. The CREAM-VI flight followed, where in addition to the previous modifications, the CD was also removed [41].

ARGO-YBJ

The ARGO-YBJ detector was located at the Yangbajing Cosmic Ray Observatory in Tibet, at an altitude of 4300 m asl. The detector consisted of a Resistive Plate Counter (RPC) carpet with dimensions $\sim 78 \times 74$ m^2 with $\sim$93% active area. It was used to study the cosmic ray spectrum starting from energies lower than a few hundred TeV. To more precisely measure the p+He spectrum, the measurements of the ARGO-YBJ detector and of a single wide field of view Cherenkov telescope (WFCT) were combined. The WFCT was a prototype of the LHAASO experiment [42].

HAWC

The HAWC experiment is detecting CRs and γ-rays from $\sim$ TeV energies, by measuring the product of their interaction with the Earth's atmosphere manifested

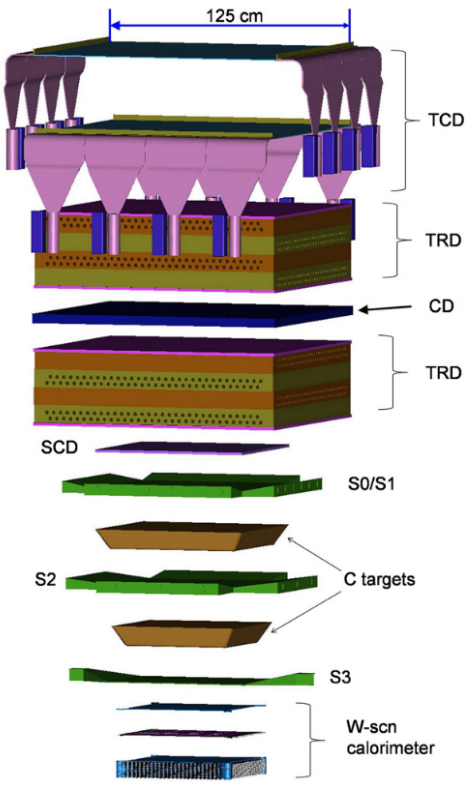

Figure 1.8: Scheme of the CREAM experiments with its subdetectors [5].

through EAS. It is located at the high altitude of $\sim$ 4100 m on the Sierra Negra Volcano in Mexico and covers a surface larger than 22000 m^2 composed of an array of 300 Cherenkov detectors. The detectors have a cylindrical shape with a 7.3 m diameter and 4.5 m height, detecting the signal using 4 photomultipliers (PMT) [43].

KASCADE

The KASCADE experiment measured CR showers in the primary energy range from $\sim$ 100 TeV to $\sim$ 100 PeV. The detector was placed in Karlsruhe (Germany) and it was composed of a so-called field array, a central detector, and a muon-tracking detector. The field array was the apparatus employed for measuring proton and helium spectra and it consisted of 252 detectors organized in a 200 $\times$ 200 m^2 grid with 13 m spacing, used to measure and separate electrons and muons. Furthermore, the reported results on the proton and helium spectra are based on two different hadronic interaction models: QGSJet and SIBYLL [44].

MACRO and EAS-TOP

Two experimental apparatuses, MACRO and EAS-TOP, were used together to measure CR proton, helium, and CNO in the energy range $\sim$ 80 TeV to $\sim$ 300 TeV. EAS-TOP was placed at 2005 m asl, on the Campo Imperatore plateau and it detected charged particles with an array of scintillators and a hadronic calorimeter, and atmospheric Cherenkov light (CL). EAS-TOP was composed of a CL array consisting of 5 telescopes placed at distances of 60 m or 80 m, comprising two wide-angle detectors with 7 photomultipliers each. MACRO was placed at the National Gran Sasso Laboratories, deep underground (3100 m w.e.) and it was a multi-purpose apparatus of 76.6 $\times$ 12 $\times$ 4.8 m^3 that could detect penetrating cosmic radiation. As shown in Fig. 1.9, around 1100 to 1300 m of rock separated MACRO and EAS-TOP, depending on the angle [45].

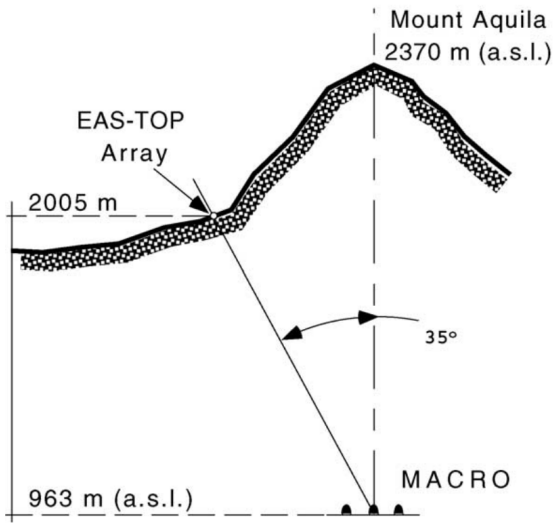

Figure 1.9: Scheme of the EAS-TOP array located on the Campo Imperatore plateau and the MACRO experiment placed underground [45].

1.6.3 Precise measurement of the p+He spectrum: motivations

The all-particle CR spectrum exhibits several features that are not yet understood (see section 1.4). A well-known prominent feature is the so-called "knee", a clear steepening of the spectrum around 3 $\times$ 10^{15} eV. Over the years, various hypotheses were raised regarding the reason behind the presence of this structure [46] and several experiments tried to approach the knee energy region, in their mea-

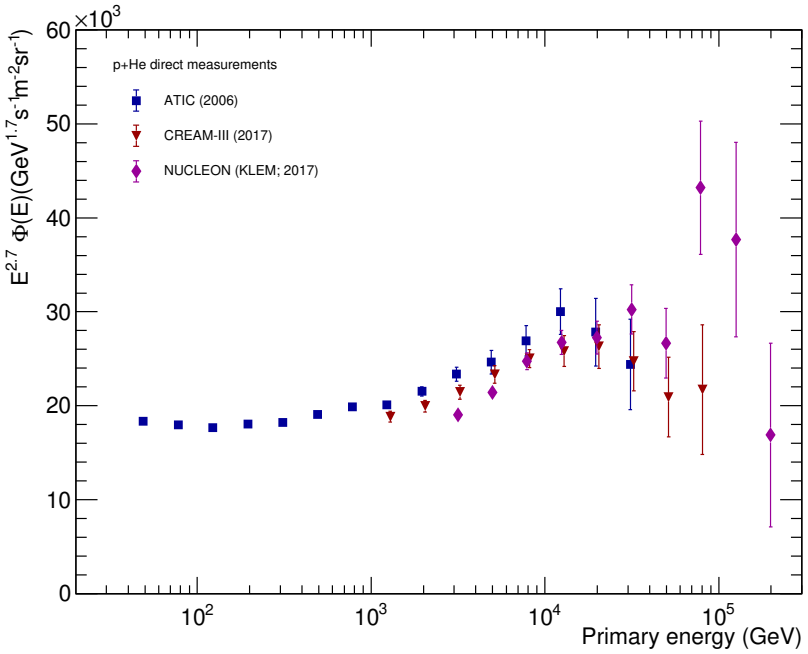

Figure 1.10: Results on the proton+helium spectrum from direct [6, 7, 10] detection experiments. Error bars represent both statistical and systematic uncertainties added in quadrature.

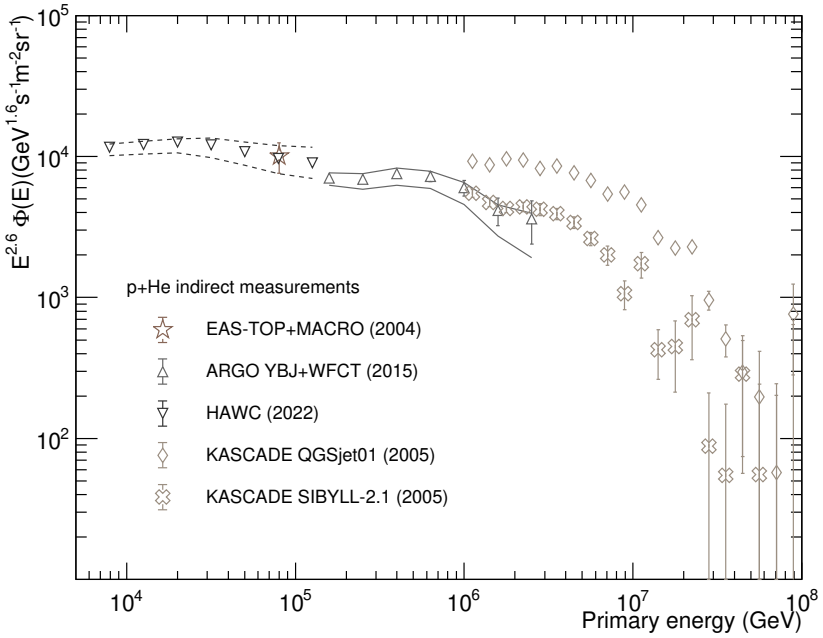

Figure 1.11: Results on the proton+helium spectrum from indirect [42–45] detection experiments. Error bars represent statistical and systematic uncertainties added in quadrature for EAS-TOP+MACRO and KASCADE. For HAWC and ARGO-YBJ they indicate only the statistical uncertainties, while the systematics are represented by the dashed and continuous lines respectively.

surements of the CR spectrum. One theoretical scenario interprets the knee as the maximum reachable energy for galactic particle accelerators, meaning that the knee energy represents the transition between galactic and extra-galactic CRs. An additional factor is the CR propagation in the interstellar medium, which could also play a role in shaping the spectrum. Noticeably, the steepening of the spectrum in the knee region does not occur sharply, probably meaning that distinct nuclear species are accelerated up to different energies (implying the presence of several knees, depending on the particle charge, or mass). It is thus crucial to study accurately the knee region and its mass composition in order to validate or reject various possible interpretations. As explained above, the knee region is difficult to approach with direct measurements, while the separation of different species is a hard task for indirect measurements. Nevertheless, KASCADE [47] and ARGO-YBJ [42] suggested a light-component knee in their measurement of the p+He spectrum, opening the possibility of a transition between light and heavy CR abundance in the knee region, and suggesting the interpretation of the knee as steepening of the light-element spectra. Unfortunately, these measurements give different indications on the precise energy of the knee which is a consequence of ground-based experiments suffering from large uncertainties (mainly coming from the adopted EAS models), thus the mass group dominating the knee region is still unclear. If direct measurements can approach the knee region, the enigma could be solved, or at least some options could be discarded. With currently operating experiments, the exploration of such a high-energy region is challenging or even impossible. To overcome these difficulties, the aforementioned measurements performed with ground-based experiments can also be done from space. Measuring proton and helium together, having the advantage of larger statistics, can lead to directly measuring the spectrum up to the highest achievable energies and bridge ground and space-based experiments' results, eventually clarifying one or the other scenario.

Focusing on precise low-energy measurements, as shown in the previous section, the presence of a hardening feature at $\sim$ hundreds GeV/n is well established. Moreover, DAMPE revealed the presence of a softening structure at $\sim$ 14 TeV for protons and $\sim$ 34 TeV for helium, which is still puzzling the researchers. The better purity achieved by selecting a combined proton and helium sample and the increased statistics will allow further confirmation of the presence of the two features while acting as a cross-check for the results obtained with the separate analyses of protons

and helium.

A p+He spectral measurement is a promising tool for exploring the region connecting ground- and space-based experiments, and for significantly evaluating and confirming the spectral features detected in the proton and helium spectra.

The description of the DAMPE experiment will be given in the next chapter, followed by the p+He analysis procedure and the spectral measurement resulting from this work.

Chapter 2

The DAMPE experiment

The analysis presented in this thesis is based on direct CR measurements performed by the DAMPE experiment. Therefore, this chapter will focus on DAMPE and, in particular, will describe the scientific objectives, the detector structure, and its sub-detectors, continuing with an overview of the software used for data processing and Monte Carlo production and concluding with a review of selected scientific results.

The DAMPE (DArk Matter Particle Explorer) satellite was sent into space on December 17th, 2015 from the Jiuquan Satellite Launch Center (China) on a Long March 2-D rocket (Fig. 2.1)[1]. It is taking data in a Sun-synchronous orbit, at 500 km altitude for more than 7 years, while more than 100 scientists from Italy, Switzerland, and China, are constantly monitoring its performance and analyzing the collected data.

2.1 Scientific goals

DAMPE was mainly designed to search for signatures of Dark Matter (DM) candidates through their annihilation or decay into Standard Model particles. The detector is indeed well suited for this purpose thanks to its very good energy resolution for electrons, positrons, and γ-rays ($\sim$ 1 % at 100 GeV, as shown in Fig. 2.2), which results in excellent capabilities of detecting even line-like structures in the energy spectra of e^-- e^+ and γ-rays.

[1]Link to the launch: `https://www.youtube.com/watch?v=Iyy_A4cQzgE`

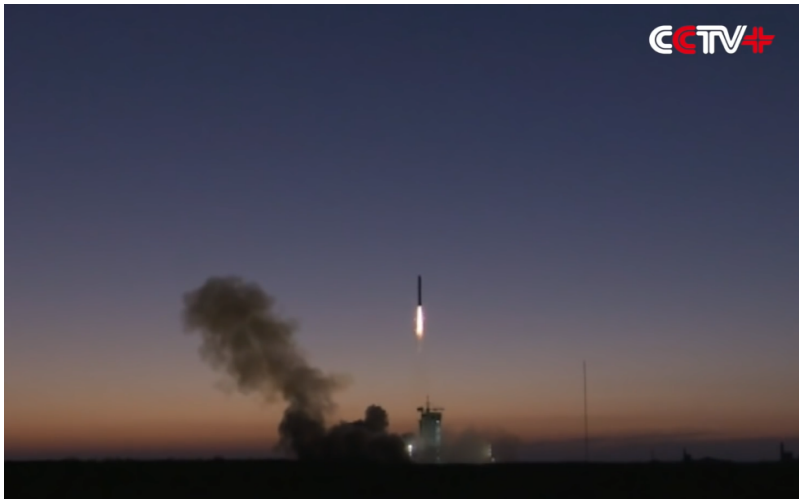

Figure 2.1: The launch of the DAMPE satellite from the Jiuquan Satellite Launch Center (China) on a Long March 2-D rocket.

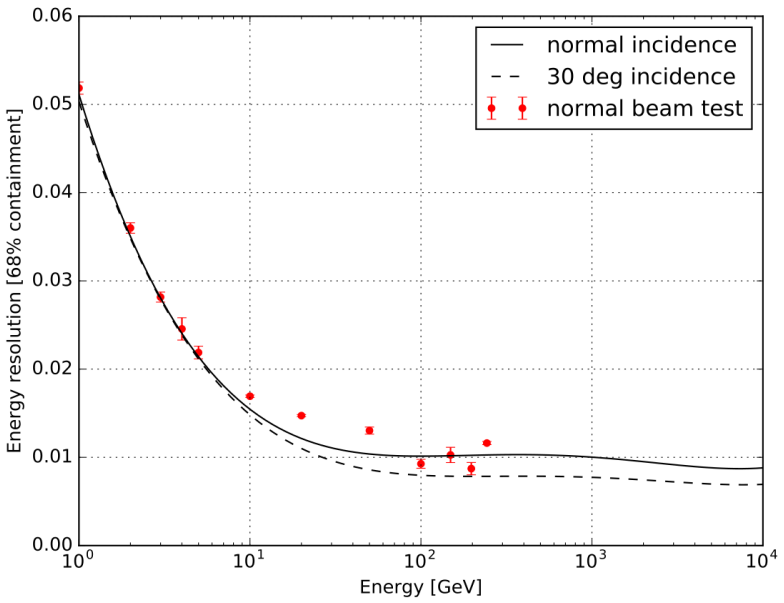

Figure 2.2: Energy resolution of the DAMPE detector for electrons/positrons and γ-rays, simulated at normal incidence (solid line) and 30° angle (dashed line), compared with test beam electron results, in red [19]

.

Considering the above-stated good energy resolution, DAMPE is an optimal instrument also for performing γ-ray astronomy, looking for sources and studying the diffuse emission, and for detecting electrons and positrons, eventually revealing structures in their combined spectrum, thus helping in the clarification of their nature and origin.

This work focuses on an additional primary goal of the DAMPE space mission: the measurement of galactic cosmic rays (GCRs) spectra, from tens of GeV to hundreds of TeV. The study of primary and secondary GCRs, along with their ratios, can shed light on CRs acceleration and propagation mechanisms inside our galaxy (as discussed in the previous chapter), and DAMPE has the capability of exploring for the first time the high-energy region of the CR spectra with relatively small uncertainties.

Other DAMPE scientific objectives include the study of the Forbush decrease and time evolution of the electron and positron fluxes, cosmic-ray anisotropies, multimessenger astronomy, and exotic physics (e.g. search for fractionally charged particles in space).

The measured DAMPE proton and helium spectra are shown in section 1.6.1, while a summary of results regarding the aforementioned main scientific goals will be given in section 2.9.

2.2 The detector

The DAMPE satellite is composed of 4 sub-detectors, working together to identify particles and nuclei and reconstruct their energy. In figure 2.3 a schematic view of the DAMPE instrument, with its sub-detectors, can be seen. A typical event accepted in the analyses is represented by a particle impinging on the top of the plastic scintillator detector (PSD), and crossing the other sub-detectors: the silicon tungsten tracker (STK), the bismuth germanium oxide (BGO) imaging calorimeter, and the neutron detector (NUD). The PSD is used to identify the charge of the particle and as a veto for γ-rays. The silicon strips of the STK help in reconstructing the track of charged particles, while the tungsten layers of the same detector convert photons in electron-positron pairs, allowing the γ-ray direction measurement as well. When the particles enter the BGO, they initiate a hadronic or electromagnetic shower discriminated one from the other, thanks to the imaging capabilities of the

BGO, which also measures the total energy deposited in its volume. Finally, the NUD detects neutrons from the hadronic showers, further separating them from the electromagnetic ones. In the following sections, the 4 sub-detectors will be described in more detail. For additional information, see [19].

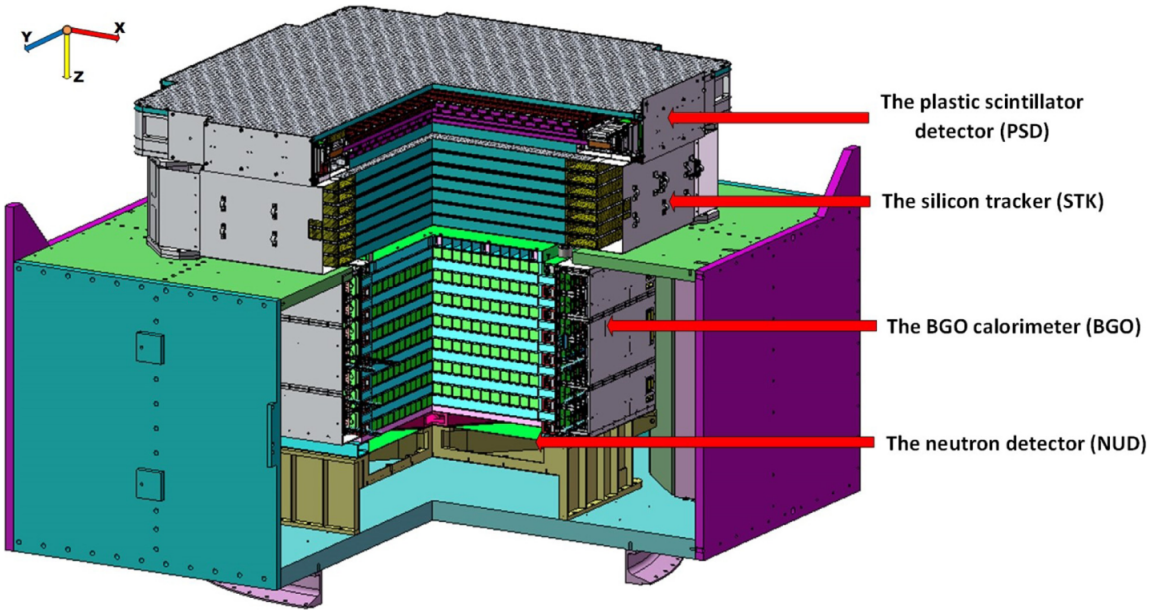

Figure 2.3: The DArk Matter Particle Explorer with its four sub-detectors [19].

2.3 The Plastic Scintillator Detector (PSD)

The PSD is placed at the top of the DAMPE satellite and it's used to measure the absolute value of the electric charge (hereafter indicated with *charge*) of particles and nuclei, thus discriminating different nuclear species with charge (Z) ranging from 1 to 26, and possibly even beyond. The PSD is also well suited for separating electrons from γ-rays. In fact charged particles release energy when crossing a given material thickness, according to the Bethe-Bloch formula [48] producing a detectable signal in the PSD. Considering the energy range of interest for DAMPE, incoming γ-rays could produce e^--e^+ pairs if the medium is dense and thick enough. Given that the plastic scintillator is made of light material (typically with density $\rho \simeq 1 \frac{g}{cm^3}$) the required thickness for pair production ($\sim$ 50 cm) is much larger than the DAMPE PSD dimension and γ-rays will therefore not release any signal in this sub-detector. This characteristic is fundamental to separate electrons from γ-rays since these two particles will behave in a similar way in the following sub-detectors.

After crossing the PSD, particles and nuclei will hit other sub-detectors, eventually producing secondaries and fragments. Some of the secondary particles might be backscattered and then cross the PSD again (back-splash effect), thus being misidentified as primaries. The detector structure was optimized in order to reduce this effect as much as possible. The PSD comprises 82 plastic bars with dimensions 884 mm × 28 mm × 10 mm and scintillator material EJ-200, from Eljen Technology Corporation[2]. The bars are placed on two orthogonal layers, called X-layer and Y-layer, composed of 2 planes of parallel bars each. In Fig. 2.4 a schematic view of the PSD shows the staggered configuration (of 8 mm) in which the 82 bars are organized, reducing the back-splash effect. Furthermore, the fake events due to the back-splash effect can be reduced by combining the PSD signal with the one recorded by other sub-detectors (i.e. STK and BGO). The total active area resulting from this configuration is 825 mm × 825 mm. At both ends of each bar Photo

Figure 2.4: Schematic view of the PSD [49]

Multiplier-Tubes (PMTs) are used to read the signals resulting from the energy released from the ionizing particles. Specifically, the devices used for the PSD are R4443 PMTs, from Hamamatsu Photonics[3]. The total detection efficiency of the PSD is ≥ 0.9975 [49]. An ultra-relativistic particle with $|Z| = 1$ crossing a PSD bar perpendicularly will release a signal of ~ 2 MeV, which will be referred to as 1 MIP (Minimum Ionizing Particle) signal. In general, the energy released by any nucleus with charge Z is proportional to Z^2 in the relativistic energy regime (as described by the Bethe-Bloch formula [48]) making their identification and separation possible. In order to cover a broad dynamic range while keeping a good charge resolution, a double-dynodes readout scheme is used for each PMT. Dynodes with lower gain are used to read the signals in the range from 4 MIPs to 1600 MIPs, while higher gain is used for the range of 0.1 MIPs to 40 MIPs. The overlapping region is used for inter-calibration purposes [50]. Several beam tests were performed on the DAMPE Engineering Qualified Model (EQM), to study the performance of each sub-detector. Specifically, a heavy-ion beam test was carried out at CERN SPS in March 2015.

[2]Eljen technology, `http://www.eljentechnology.com/`
[3]Hamamatsu photonics k.k., `http://hamamatsu.com/`

The PSD charge spectrum was obtained using the test beam data, and fit using a multi-Gaussian function in order to extrapolate the charge resolution values (shown in Fig. 2.5 for the PSD bottom layer) which is ~ 0.22 for He and it increases linearly with Z. The charge resolution obtained with the EQM is expected to be worse than

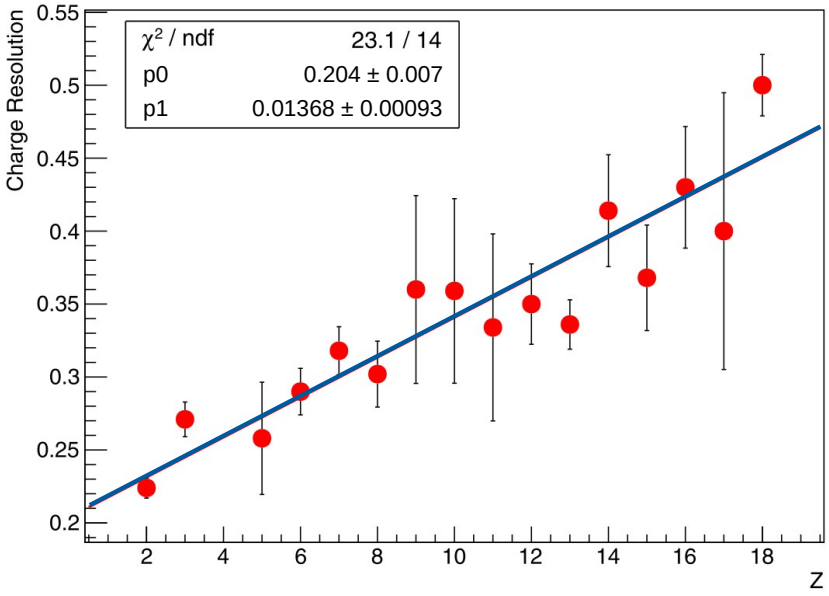

Figure 2.5: Charge resolution of the PSD bottom layer with respect to the charge (Z) of the incoming particle, as obtained with heavy-ion beam tests at CERN SPS [51].

the real case because the STK was not completely assembled, and this prevented from having a good track reconstruction, thus applying all the needed corrections to the signal in the PSD (such as traversing length and light attenuation correction) [51]. After two years of on-orbit operation, the charge resolution was measured again by using flight data and was found to be 0.18 for Carbon and 0.30 for Iron [52]. The charge spectrum obtained using the PSD of DAMPE, with a sample of two years of collected data, is shown in Fig. 2.6. The obtained spectrum highlights the DAMPE capabilities of separating different nuclear species with very good charge resolution. Indeed, the peaks are very well separated starting from hydrogen (which is more abundant and shows a sharper peak), up to iron and nickel (less present, broader peaks). As shown in section 1.3, the GCR composition is similar to the solar system one, and it is thus fundamental to identify different nuclei in order to better investigate the cosmic ray origin and the acceleration and propagation mechanisms.

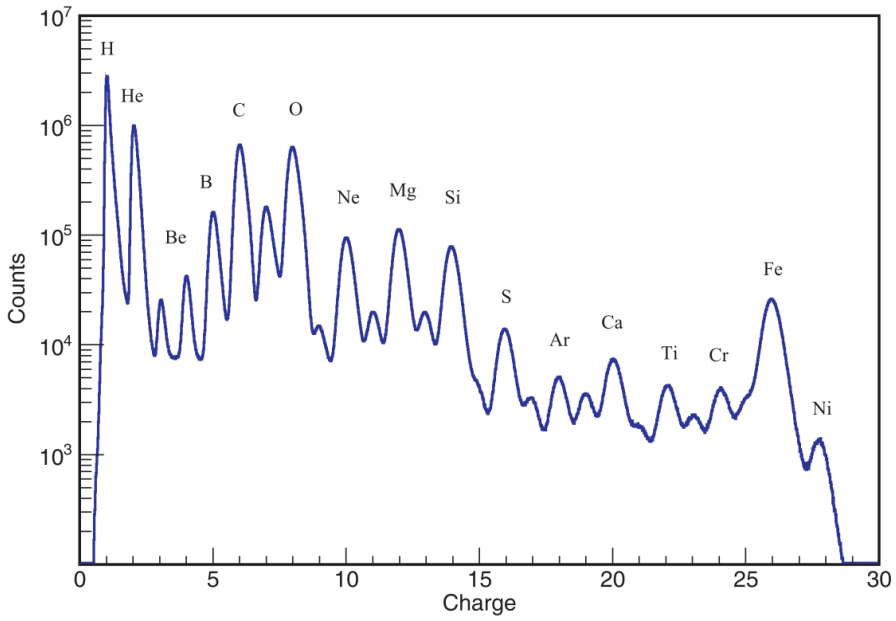

Figure 2.6: The DAMPE PSD charge spectrum obtained with two years of on-orbit data acquisition, for CR integrated energy above the trigger threshold [52]. The nuclei peaks from hydrogen to nickel are clearly visible and well separated.

2.4 The Silicon Tungsten Tracker (STK)

Starting from the top, the second DAMPE sub-detector is the Silicon Tungsten Tracker (STK), which is fundamental for precise track reconstruction of the incoming particles. The STK is composed of 6 planes, each one made of 2 orthogonal layers of silicon micro-strip detectors. This configuration allows measuring the X-Y coordinates (see Fig. 2.3). Between the 2nd, 3rd and 4th silicon layers, 1mm-thick tungsten plates are installed, in order to convert the impinging photons into electron-positron pairs, allowing their tracking as well (see Fig. 2.7). The first tracking plane is used

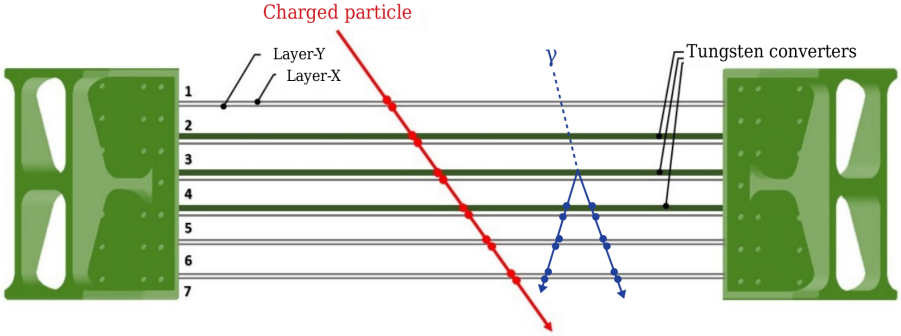

Figure 2.7: A scheme of the Silicon Tungsten Tracker (STK) is presented in this picture. The 6 planes, each one composed of 2 layers (X and Y) are shown, along with the 3 tungsten converters, used for photon pair-production.

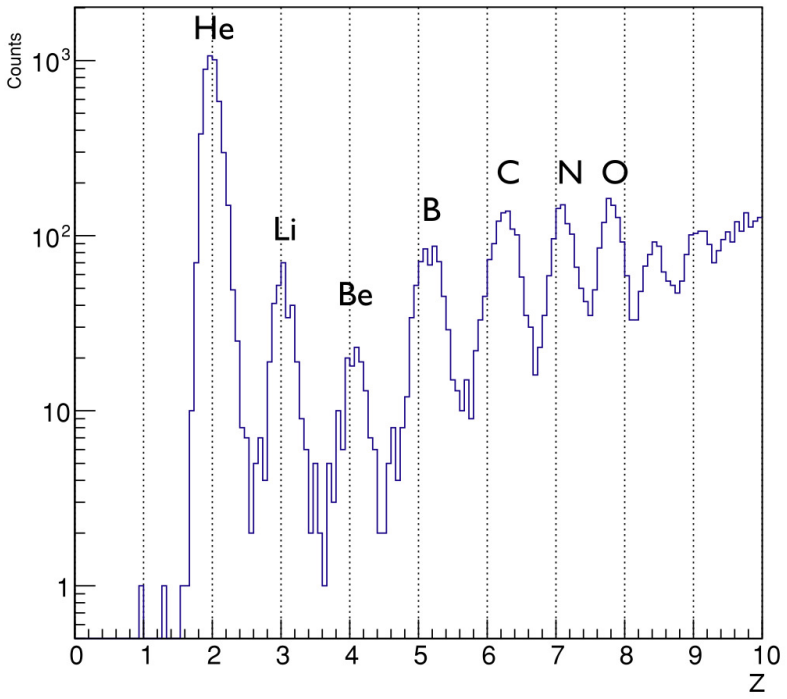

Figure 2.8: Signal recorded after exposing the STK to a lead beam, and after removing particles with charge Z=1 [19]. Various fragments of lead nuclei ranging from Hydrogen up to Oxygen can be identified using the STK, even if with a lower resolution with respect to the PSD.

to measure the coordinate of the entering particle and to link this measurement with the one of the PSD, placed above the STK. The tungsten converters are placed only on 3 layers, in order to ease the tracking of the e^+-e^- pairs produced by γ-rays, using the subsequent layers. Charged particles could undergo multiple scattering while crossing the tungsten layers, but if their energy is larger than 5 GeV, considering the thickness of the tungsten layers ($\sim$ 1 mm), this effect is negligible ($\theta_0 \simeq 0.08°$). Furthermore, the signal acquired by the STK is proportional to the charge |Z| of the nuclei, which implies a possible additional usage of the STK to complement the PSD measurement (even if with lower resolution and dynamic range) and separate nuclei from helium up to oxygen. In Fig. 2.8 the charge identification capabilities of the STK are shown.

The STK comprises 192 modules (called ladders), made of 4 single-sided micro-strip detectors from Hamamatsu Photonics[4]. Each micro-strip is 48 μm wide and 93.196 mm long, with a pitch of 121 μm. The ladders are instrumented on 7 support trays produced from Composite Design Sàrl[5], forming the full detector (see Fig.

[4] http://hamamatsu.com/
[5] http://www.compositedesign.ch

2.9), for a total dimension of $95 \times 95 \times 0.32$ mm^3. The EQM of the STK was exposed

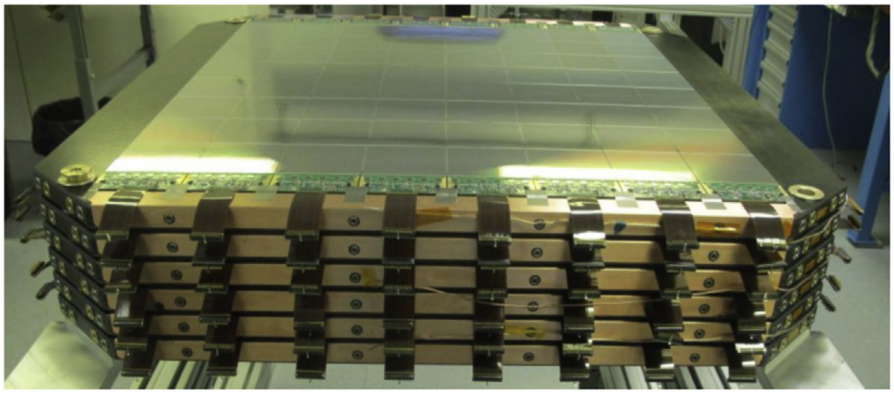

Figure 2.9: Picture of the Silicon Tungsten Tracker (STK), taken from [53]. The 6 planes can be seen, along with the 64 silicon detectors on the top layer.

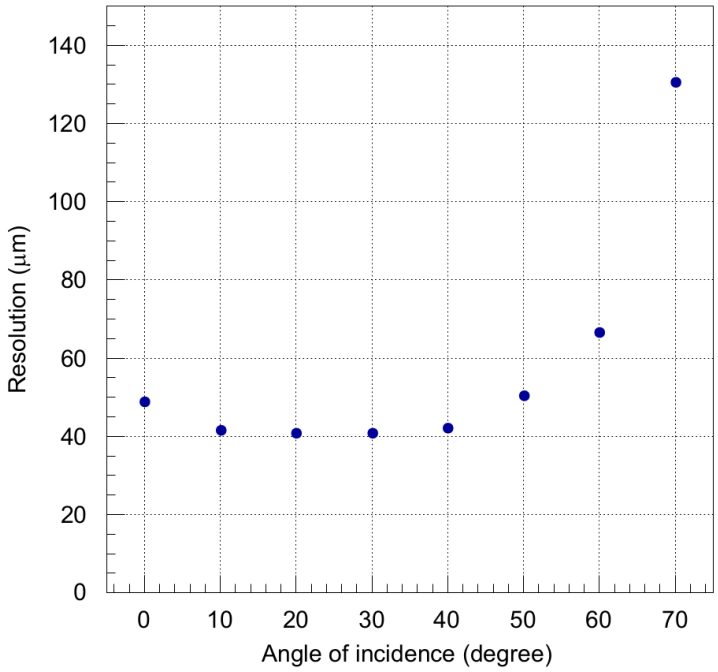

Figure 2.10: Position resolution of the STK, measured using a 400 GeV proton beam with different incident angles. The measured STK resolution is ~ 40 μm for incident angles from 10° up to 40°, ~ 50 μm for 0° and 50°, and it increases with increasing inclination.

to 400 GeV proton beams during the test beam campaign at CERN, in order to evaluate the performance of the detector and its position resolution. The results from the test beam are shown in Fig. 2.10, for various incident angles from 0° to 70°. The obtained results show that the position resolution is quite constant and it is ~ 40 μm for incident angles from 10° up to 40°, while it becomes a bit higher (~ 50 μm) for incident angles of 0° and 50°. The resolution increases even more

for larger angles which are anyway less relevant since more inclined events will be rejected during the data analysis procedure.

The aforementioned results demonstrate that the STK is an excellent instrument for track reconstruction and it also performs very well as a complementary detector (to the PSD) for charge measurement of CR nuclei up to oxygen.

2.5 The Bismuth Germanium Oxide imaging calorimeter (BGO)

After crossing PSD and STK, a particle impinging on the DAMPE satellite will encounter the Bismuth Germanium Oxide imaging calorimeter (BGO). The BGO is used to measure the energy deposition of particles and nuclei and to discriminate electromagnetic showers from hadronic ones by reconstructing their 3D image. The BGO is made of 14 layers with 22 bars of Bismuth Germanium Oxide crystal each. The bars in one layer are parallel to each other, and perpendicular to the one of the next (or previous) layer (see Fig. 2.11). The size of one bar is $25 \times 25 \times 600$ mm^3, forming a total active area of the calorimeter of 60×60 cm^2.

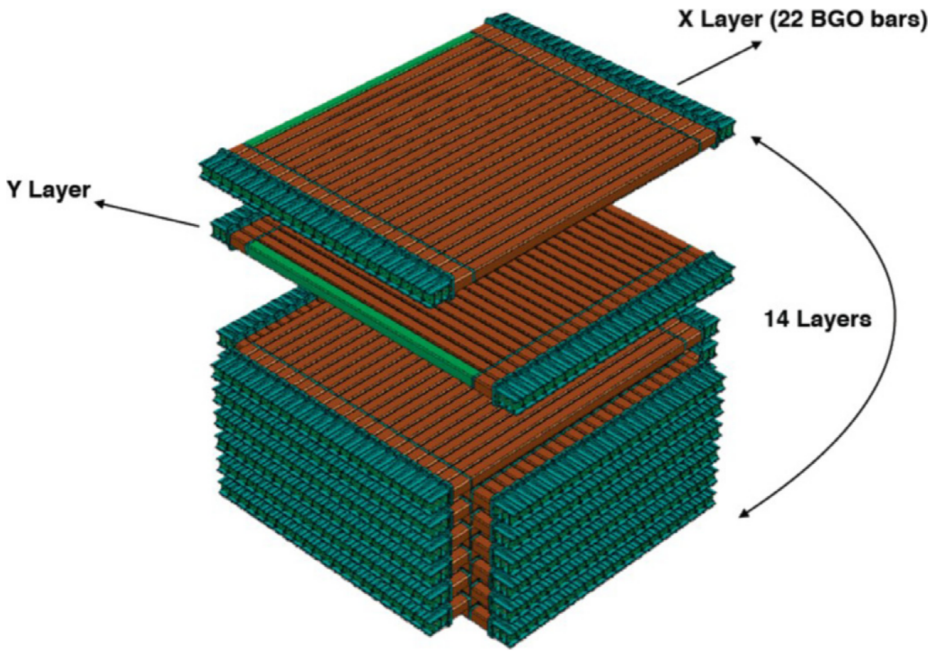

Figure 2.11: Scheme of the Bismuth Germanium Oxide imaging calorimeter (BGO). The 14 layers (divided into X and Y layers) can be seen, along with the 22 BGO bars composing each one of them [19].

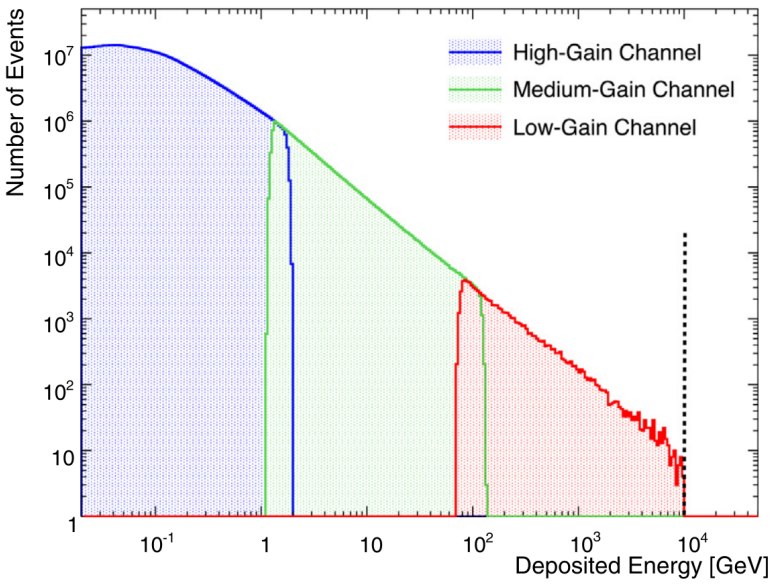

Figure 2.12: Energy deposited in the BGO, read by the three different dynodes on the S1 end of one bar. The (blue) high-gain channel corresponds to dy8, the (green) medium-gain to dy5, and the (red) low-gain to dy2. The upper limit for the measurements is represented with the dashed black line [54].

Two Hamamatsu R5610A-01 PMTs (called S0 and S1) are placed at both ends of the bars to collect the scintillation light produced in the BGO crystals. Having a reading on both sides allows the measurement of the position in which the energy is deposited. Furthermore, in order to increase the dynamic range, the signal read-out is performed using three dynodes (dy2, dy5, dy8) with different gains: (a) dy8 covers the range [2 - 500] MeV on S0 and [10 MeV - 2.5 GeV] on S1; (b) dy5 covers the range [80 MeV - 20 GeV] on S0 and [400 MeV - 100 GeV] on S1; (c) dy2 covers the range [3.2 - 800] GeV on S0 and [16 - 4000] GeV on S1. In Fig. 2.12, the energy read by the three dynodes on the S1 side is shown.

In order to separate electrons and positrons from protons, the 3D image of the shower is used. In general, showers initiated by electrons (and γ-rays) or protons (and heavier nuclei), will have a different development in the BGO material. Specifically, the radiation length (X_0) of the BGO is 1.12 cm and the nuclear interaction length (λ_I) is 22.8 cm, for a total of $\sim$ 32 X_0 and $\sim$ 1.6 λ_I, considering the full BGO detector. Consequently, electromagnetic and hadronic showers will exhibit different behaviors in the BGO both longitudinally and transversally. The electron/proton separation was studied using MC simulations and test beam data, resulting in a proton rejection power at the level of 10^5, in the GeV-TeV regime, with at least 90% electron identification efficiency. More details on this topic will be given in the next

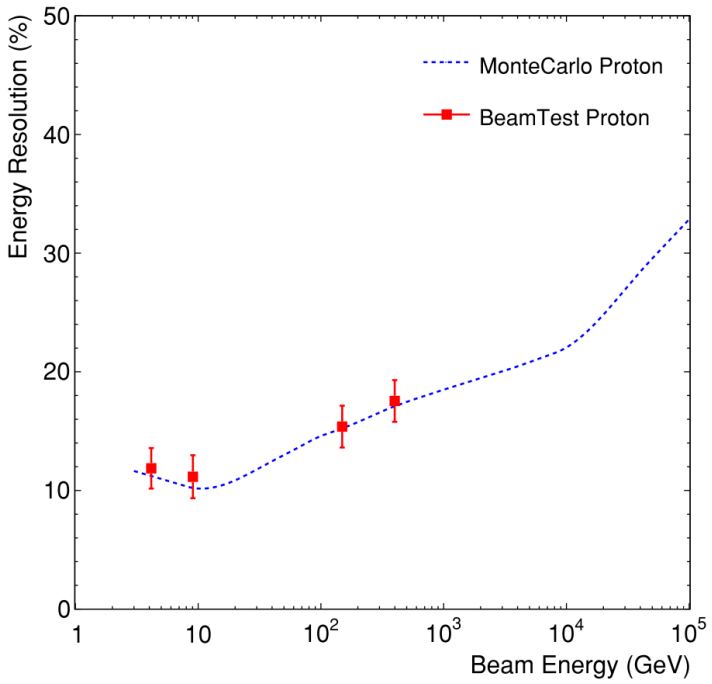

Figure 2.13: BGO energy resolution for protons. MC (blue dashed line) and beam test results (red filled squares) are compared [19].

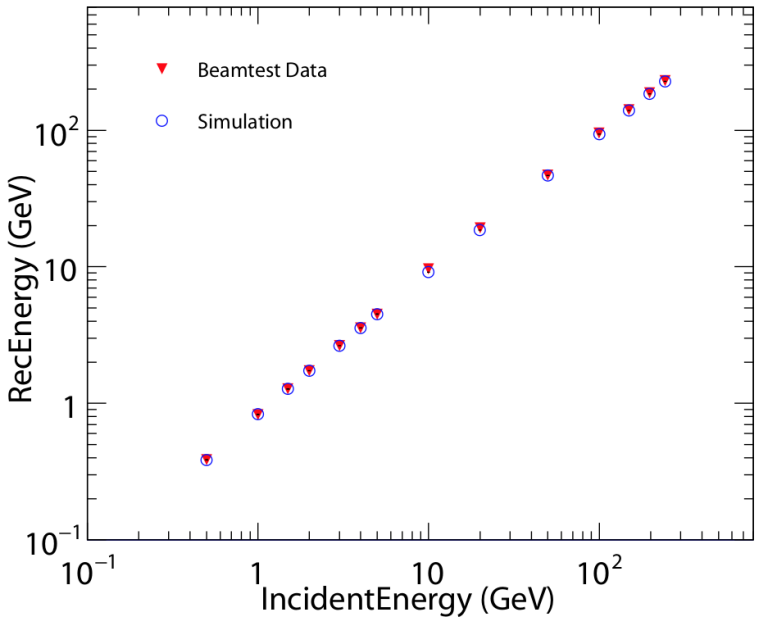

Figure 2.14: Energy linearity of the DAMPE BGO calorimeter. Beam test data (red inverted triangles) refer to electrons data taken during the beam test at CERN in 2014, and they are compared with simulated data (blue empty circles) [55].

chapter.
The energy resolution was evaluated during the test beam campaign, and compared with MC results. For electrons and γ-rays, this is found to be better than 1.2% for energy larger than 100 GeV (see Fig. 2.2). For protons, the energy resolution has a minimum value of $\sim$ 10 % at $\sim$ 10 GeV and it worsens with increasing energy, as shown in Fig. 2.13 [19].

Furthermore, the linearity of response of the BGO was tested and compared with simulated data (see Fig. 2.14) showing a positive result from both linearity and MC-data agreement perspectives. A description of the software used to produce MC simulations and process the data from the satellite will be given in section 2.8.

In addition to the main purpose of energy measurement and shower image reconstruction, the BGO can also be used to reconstruct the particle's track, with a lower resolution with respect to the STK. This information can eventually be used to complement the STK measurement and to provide a seed for the STK track reconstruction.

2.6 The Neutron Detector (NUD)

Placed at the bottom of the DAMPE satellite, the NeUtron Detector (NUD) is used to detect neutrons coming from hadronic showers initiated in the BGO calorimeter. In general, the neutron content in hadronic showers is $\sim$ one order of magnitude larger than the electromagnetic showers' one. This translates to better electron-proton separation capabilities of the DAMPE detector, thanks to the NUD.

The NUD is composed of four boron-loaded plastic scintillators EJ-254 produced from Eljen Technologies, with 5% boron concentration. In order to increment the photon collection efficiency, wavelength shift fibers are inserted in each scintillator. The signal is then read out using four Hamamatsu R5610A-01 PMTs placed at the corners. The structure of the NUD is shown in Fig. 2.15.

Neutrons produced in the BGO, will reach the NUD after $\sim$ 2 μs, and will possibly be captured by the ^{10}B in the scintillators, through the following process: $^{10}\mathrm{B} + \mathrm{n} \rightarrow {}^{7}\mathrm{Li} + \alpha + \gamma$. Each capture process will produce $\sim$ 600 photons and will occur with a probability inversely proportional to the neutrons' speed, and a time constant inversely proportional to the ^{10}B loading.

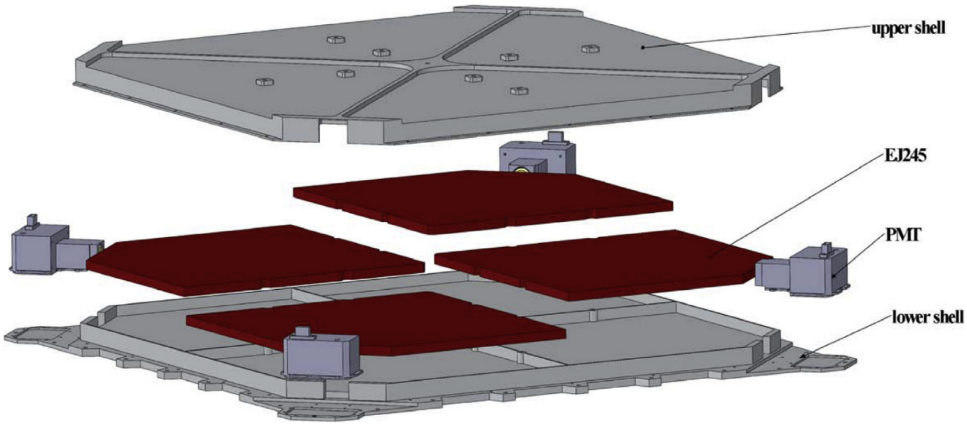

Figure 2.15: Structure of the NeUtron Detector (NUD) [19].

The proton rejection capabilities of the NUD were studied during the test beam at CERN. Usually, the shower containment in the BGO is total for electrons and $\sim$ 30%-40% for protons (in the energy range of interest for DAMPE). Consequently, for this study, 450 GeV proton events were compared with 150 GeV electron events. The results are reported in Fig. 2.16, where it can be seen that the proton signal is always larger than the electron one. Specifically, the electron signal is below 2 channels most of the time, and always below $\sim$ 26 channels.

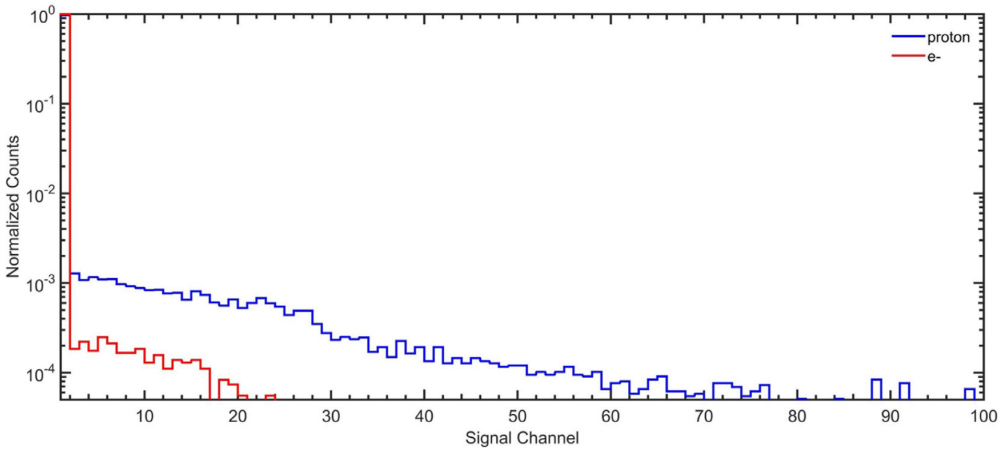

Figure 2.16: NUD signal for 150 GeV electrons and 450 GeV protons (expected to deposit $\sim$ 150 GeV in the BGO calorimeter) [19].

Besides the test beam results, the NUD response was also studied using MC simulations. With the requirement of electron detection efficiency of 0.95, the proton rejection is found to be of a factor of $\sim$ 10. After the launch, the collected data result in a rejection power of $\sim$ 12.5, for 800 GeV energy deposited in the BGO [19].

2.7 Data acquisition and trigger logic

In DAMPE, the data are acquired thanks to a combined work of BGO and trigger board. When the signal recorded by the BGO meets the trigger criteria, a signal will be sent from the trigger board to the data acquisition (DAQ) system. Specifically, the DAQ system is composed of two electronic crates: the Payload Data Processing Unit (PDPU) and the Payload Management Unit (PMU). Science data and housekeeping data are collected on the +X/+Y side of DAMPE from the PDPU and on the -X/-Y from the PMU. The latter has a memory of $\sim$ 16 GB used for the temporary storage of the collected data, which will be finally sent to the ground stations from the PMU.

Three types of triggers were designed for DAMPE: external trigger, periodical trigger, and event trigger. The external trigger has been used for testing the detector before the launch. The periodical trigger generates a fixed number of events with a specific rate, with the purpose of pedestal calibration and electronics linearity calibration. Finally, the event trigger is used for collecting science data and comprises four different trigger configurations: Unbiased Trigger (UNBT), Minimum Ionizing Particles Trigger (MIPT), High Energy Trigger (HET), and Low Energy Trigger (LET). A scheme of the DAMPE trigger system is shown in Fig. 2.17.

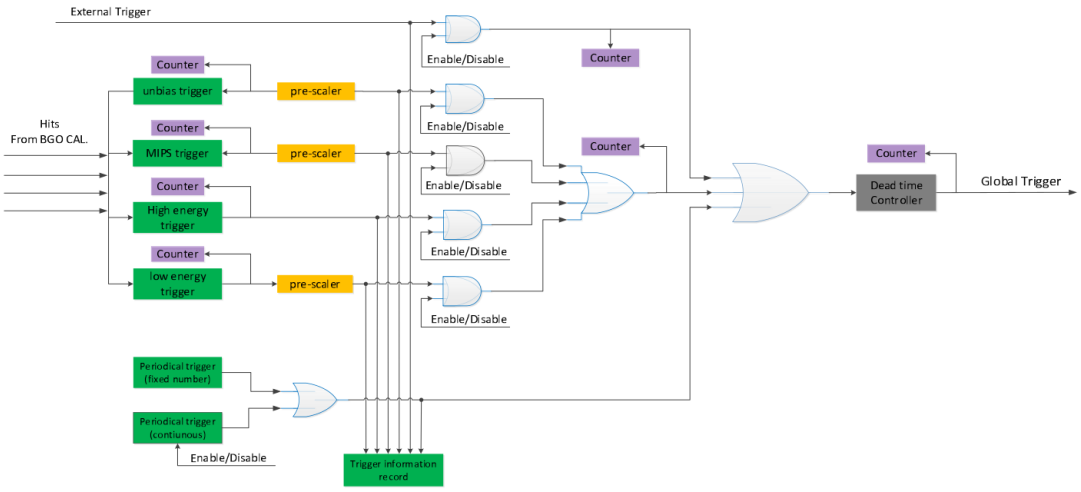

Figure 2.17: Schematic view of the trigger logic of DAMPE [56].

The least restrictive trigger is the UNBT, with the request of $\sim$ 0.4 MIPs in the top two BGO layers. This choice results in $\sim$ 100% trigger efficiency to high energy electrons and γ-rays (with energy larger than 5 GeV), and it allows using the UNBT to estimate the HET efficiency. Apart from collecting data for science results, event

triggers can also be used for energy calibration of the BGO calorimeter on orbit. In particular, the MIPT was designed for this purpose. The MIPT is activated when the threshold of $\sim$ 0.4 MIPs is achieved in the top and bottom layers of the BGO (layers 3, 11, and 13 or layers 4, 12, and 14), ensuring that the incoming particle will cross the BGO from top to bottom, without initiating a shower, and depositing a MIP energy ($\sim$ 23 MeV for a 25 mm-thick BGO bar). Incoming particles and nuclei will initiate a shower either before (in the case of electrons and γ-rays) or in the top layers (protons, nuclei, and part of electrons and γ-rays) of the calorimeter. In order to select these events, a higher energy threshold is required, in the top BGO layers. This is done with the HET, which requires deposited energy larger than 10 MIPs in the first three layers, and larger than 2 MIPs in the fourth layer of the BGO. Finally, the LET has the lower threshold of 0.4 MIPs in the first two BGO layers and 2 MIPs in the third and fourth layers, to select shower initiated by low energy electrons and γ-rays (starting from $\sim$ 1 GeV energy).

Considering the high event rate during on-orbit operations (see Fig. 2.18) combined with the dead time of the DAQ (3.0725 ms), UNBT, LET and MIPT are pre-scaled.

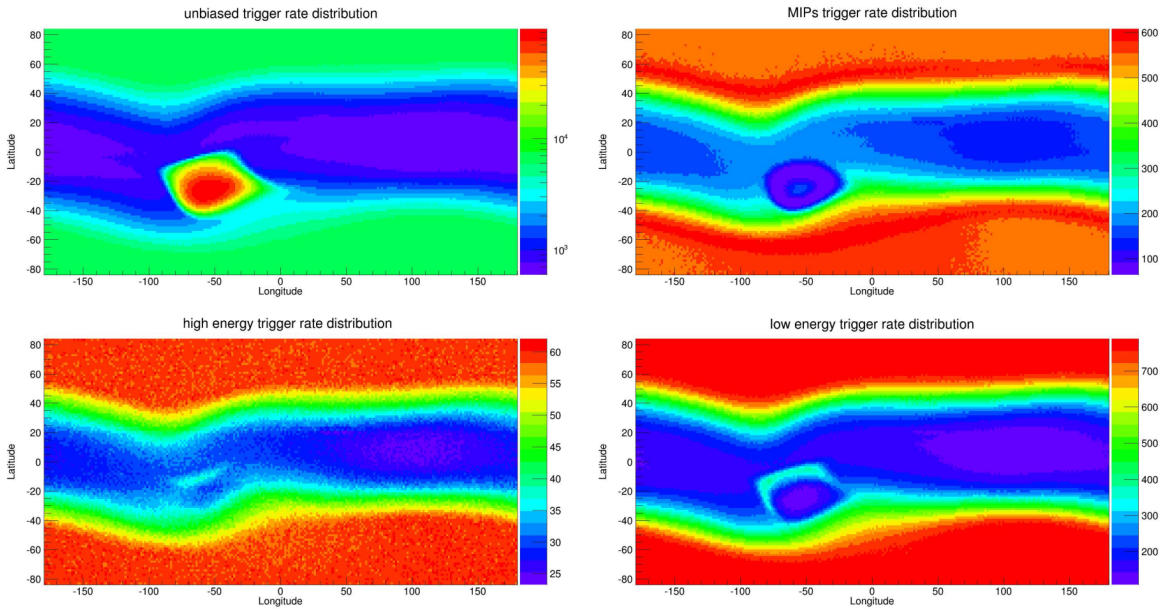

Figure 2.18: Trigger rate (color code in Hz) of the four event triggers of DAMPE, for various regions of the sky, in galactic coordinates. The trigger rate shown here is before pre-scaling [56].

The regions with the highest event rate are the South Atlantic Anomaly (SAA), clearly visible as the red region in the UNBT rate distribution in Fig. 2.18, and

the polar radiation zone (roughly outside the -20° and +20° latitude region). In particular, in the SAA the rate is so high (up to 100 kHz for UNBT) that it can interfere with normal operations of the satellite, such as the performance of the electronics, pedestal, and dynode linearity. For this reason, events collected in the SAA, are excluded from the analyses. The pre-scaling factors are set as described in Table 2.1.

Table 2.1: DAMPE triggers during on-orbit operation.

Trigger	Operation	Pre-scaling factor	Trigger rate
UNBT	Enabled (E)	512 in (-20°; +20°); 2048 for other Lat.	∼2 Hz
MIPT	E in (-20°; +20°); Disabled for other Lat.	4 in (-20°; +20°)	∼40 Hz
HET	E	Not pre-scaled	40 Hz to 60 Hz
LET	E	8 in (-20°; +20°); 64 for other Lat.	10 Hz to 20 Hz

Thanks to the pre-scaling, the trigger rate is less than 100 Hz in most areas, as shown in Fig. 2.19, ensuring appropriate data collection considering the DAMPE science goal, and alleviating the pressure on data storage and transmission.

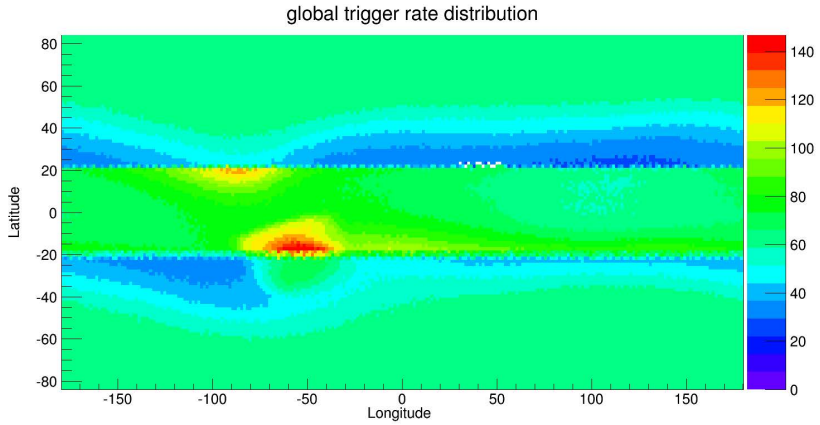

Figure 2.19: Global trigger rate (Hz) after pre-scaling [56].

2.8 DAMPE software tools

Along with detector design and optimization followed by numerous hardware tests, also a software infrastructure is required for adequate data collection and

analysis, and to perform Monte Carlo (MC) simulations. The latter is fundamental for predicting and better understanding the response of the DAMPE detector to different particles, with various energies and incoming directions. The DAMPE offline software [55] was developed for this purpose, based on C++ with the possibility of running in ROOT [57].

2.8.1 MC simulations

The DAMPE detector, with its sub-detectors and mechanical structure, is built into the software reading Geometry Description Makeup Language (GDML) files and is shown in Fig. 2.20. The simulations of CR interacting in the detector are based on

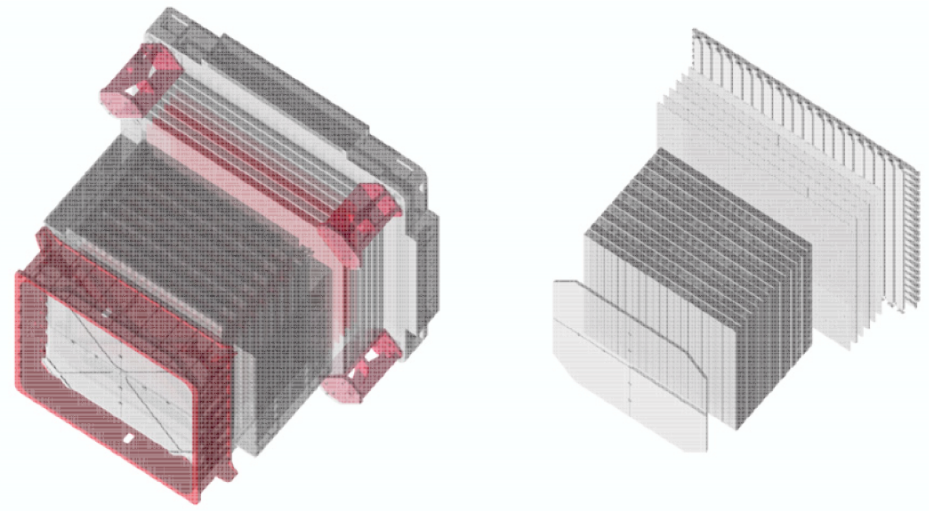

Figure 2.20: Geometry of the detector in the DAMPE software. On the left, the entire detector, including the supporting structures, can be seen. On the right, only the sensitive parts of each sub-detector are shown [55].

the Geant4 software [58], which is commonly used for particle physics experiments. The signal digitization is also implemented in the software, taking into account electronic fluctuations, noise from the pedestal, and PMT gains. Finally, the trigger conditions used during the on-orbit operations, are implemented in the simulation as well. At the end of the simulation and digitization process, MC data and flight data are stored in the same format, allowing the usage of the same reconstruction algorithms for both real and simulated samples. This implies that the simulation can actually provide an accurate representation of the detector response to incoming particles, and MC data can be processed using the same selection cuts that are applied to the flight data (more details on this topic will follow in the next chapter).

2.8.2 Flight data

Starting from the collected flight data, three data levels will follow:

- Level 0: data in binary format, sent to ground stations from the satellite ($\sim$ 12 GB per day).
- Level 1: level 0 data are organized in 13 batches comprising 12 packages for housekeeping data and 1 package for science data.
- Level 2: science data are reconstructed using the DAMPE offline software. Specifically, level 1 science data are divided into calibration files and science-data files, subsequently stored in ROOT files. Calibration files are used to extract the constants given to the reconstruction algorithm. Finally, the reconstruction is used to convert ADC counts into physical variables (energy, charge, etc.).

2.8.3 Beam test data

Several tests have been performed to confirm and further optimize the DAMPE software. Such tests include CR tests on the ground and beam test data analysis. An example of the latter is shown in Fig. 2.14, where beam test data and simulated data are compared. More details on the electron beam test results are given in [59].

Additionally, simulation and beam test data were compared using ion beams with energy of 40 GeV/n, 75 GeV/n and 400 GeV/n [51, 60, 61], showing a general agreement also in this case.

2.9 Selected DAMPE results

In section 2.1 the DAMPE scientific goals have been briefly illustrated. Afterwards, the detector with its sub-detectors, the trigger logic, and the software created for the experiment have been described. To conclude, selected results from the DAMPE space mission will be reported in this section, focusing on CR spectra (and spectral ratios) and γ-ray analysis, including dark matter search.

As can be inferred from what was previously reported (in particular in section 2.5), the DAMPE detector configuration is optimal for the detection and energy measurement of electrons and positrons. Consequently, the DAMPE collaboration

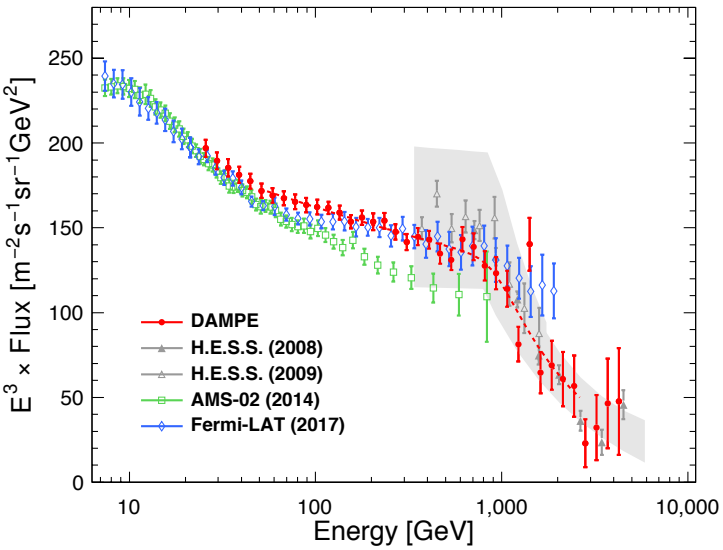

Figure 2.21: The electron-positron energy spectrum measured by DAMPE (red circles) compared with other experimental results from H.E.S.S. [62, 63], AMS-02 [64], Fermi-LAT [65]. Error bars in the DAMPE, AMS-02 and Fermi-LAT spectrum represent both systematic and statistical uncertainties added in quadrature. The error bars in the H.E.S.S. spectrum indicate only the statistical uncertainties, while the grey band corresponds to the systematic uncertainties. The red dashed line shows the fit performed with a smoothly broken power-law function on the DAMPE spectrum.

published the e^-- e^+ flux in 2017, using a sample of $\sim$ 530 days of collected data [66]. The spectrum is reported in Fig. 2.21, measured in the energy range from 25 GeV to 4.6 TeV, with high energy resolution and low background. This study led to the unprecedentedly precise detection of a spectral break at $\sim$ 0.9 TeV, evaluated by using a smoothly broken power-law fit shown in Fig. 2.21 with a red dashed line, which is favored over the single power-law fit. The main source of uncertainties from about $\sim$ 380 GeV onwards is represented by the statistics. It follows that DAMPE can provide a more precise result reaching also higher energy for the e^-- e^+ spectrum by the end of the mission. Consequently, different models can be explored and eventually confirmed (e.g. the presence of nearby sources such as pulsars and supernova remnants), by precisely measuring the spectral cutoff energy, possibly indicating the maximum energy reachable by the astrophysical accelerators. Additionally, improving this spectral measurement can help in giving further constraints on the parameter space of dark matter (DM) models, by defining new limits on DM mass or annihilation and decay cross-section.

Various models have been developed to describe the DM that is evidently per-

meating our universe. Considering particle physics models, the so-called WIMP theory has been proposed, postulating that DM might be made of Weakly Interactive Massive Particles (WIMP). Space-borne experiments can test this hypothesis by investigating the γ-ray spectrum and looking for (almost) monochromatic structures which could be generated by the annihilation of two WIMPs into a photon and another Standard Model particle. If this is the case, a spectral line should be manifested in the γ-ray spectrum with an energy value dependent on the mass of the WIMP and of the Standard Model particle produced by the aforementioned annihilation.

The DAMPE DM studies were performed by searching for possible monochromatic lines in the γ-ray spectrum covering the energy range from 10 GeV to 300 GeV, with a sample of 5 years of data [67]. The results showed no evidence of DM but they led to the definition of 95% confidence level constraints on the DM decay lifetime and annihilation cross-section. The 5-year DAMPE results are shown in Fig. 2.22, compared with the 5.8-year Fermi-LAT results [68]. Thanks to the optimal energy resolution, the DAMPE analysis provided more stringent lower limits for decaying DM with mass $\leq$ 100 GeV with respect to Fermi-LAT, demonstrating the capabilities of a thick BGO calorimeter (and excellent energy resolution) to perform DM studies in space.

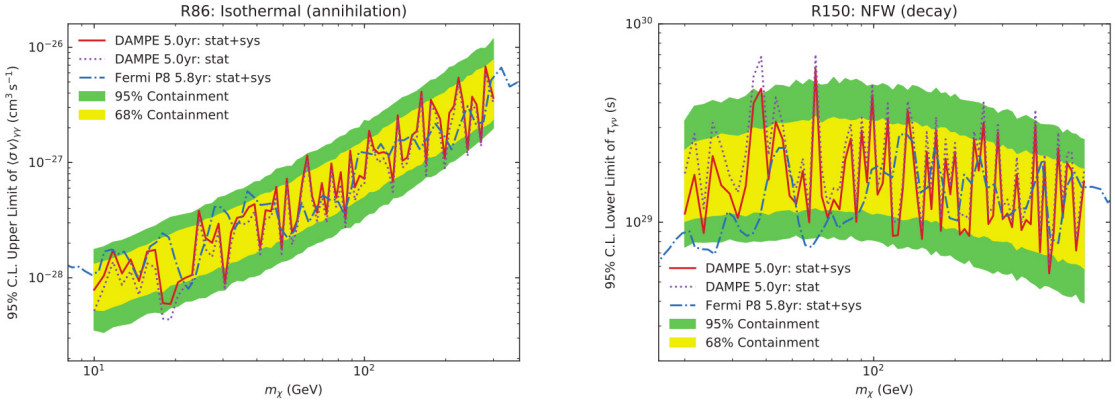

Figure 2.22: 95% confidence level upper limits for annihilating dark matter (left panel) and lower limits for the lifetime of decaying dark matter (right panel) obtained with 5 years of DAMPE data, with and without systematic uncertainties (red solid and purple dotted lines) compared with the 5.8-year Fermi-LAT results (blue dot-dashed line). Yellow and green bands show the 68% and 95% expected containment [67].

Along with searching for DM signatures, γ-ray data are also used to look for possible γ-ray sources. Specifically, 5 years of DAMPE data were used for a total of more than 2.2×10^5 photons detected above 2 GeV, leading to the preliminary

result reported in Fig. 2.23 [69]. A total of 222 γ-ray sources were identified (mostly favoring a power-law spectral interpretation) and associated with the Fermi catalog (4FGL [70]), showing that the majority of γ-rays are produced by AGNs and Pulsars.

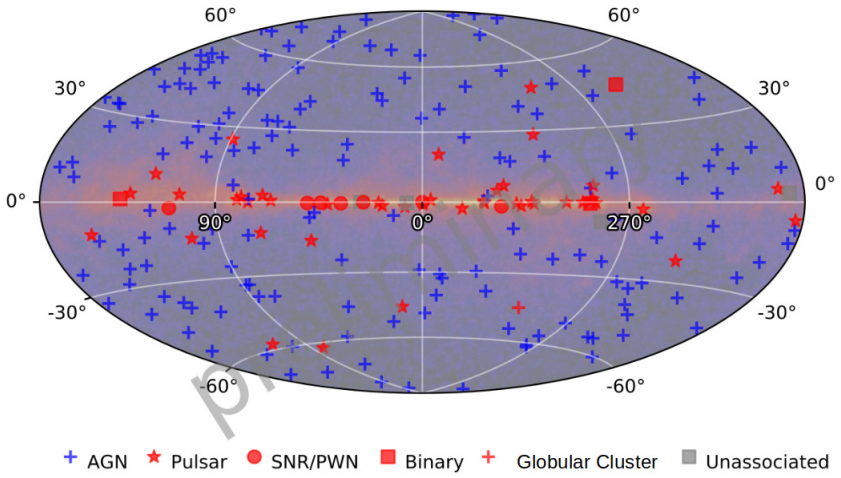

AGN	Pulsar	SNR and/or PWN	Binary	Globular Cluster	Unassociated	Total
163	44	7	3	1	4	222

Figure 2.23: γ-ray sources observed by DAMPE, after association with the 4FGL [69]. The majority of the detected γ-ray sources have been associated with AGNs and Pulsars.

The DAMPE instrument capabilities extend also to the identification and energy measurement of CR nuclei (see previous sections and in particular 2.3 and 2.5). Therefore, the proton and helium energy spectra were precisely measured, as reported in section 1.6.1 and shown in Fig. 1.6 and 1.7, resulting in new interesting results. Specifically, the spectral hardening at $\sim$ hundreds of GeV, previously observed by other experiments [2, 4–6, 10–17, 40] has been confirmed, followed by a softening at $13.6^{+4.1}_{-4.8}$ TeV in the proton spectrum and at $34.4^{+6.7}_{-9.8}$ TeV in the helium spectrum, detected for the first time with high significance [3, 9].

Further clarifications on the CR nature can be given by combining proton and helium in a single energy spectrum (p+He). The background level in this case would be much lower than the one affecting the single proton and helium samples, allowing the use of looser selection cuts when performing the analysis of satellite data. Moreover, given that proton and helium are the most abundant GCR nuclei, their combination in a single spectrum means a considerable increase in statistics, which is even more significant when applying less stringent analysis cuts. The p+He energy spectrum can thus definitely confirm the observed softening at tens of TeV and ex-

tend the covered energy range up to hundreds of TeV, finally defining the connection between direct and indirect CR measurements. More details on the motivations for this analysis are given in section 1.6.3, while the p+He spectral measurement will be described in the following chapters.

Considering the PSD identification capabilities, DAMPE is able to extend the study of CR spectra to nuclei heavier than proton and helium, starting from lithium up to iron and more. It follows that several CR analyses on medium and heavy mass nuclei are currently in progress, while recent novel results were achieved in the primary to secondary ratios. The importance of investigating spectral ratios, in addition to single nuclei spectra is delineated in section 1.3. Specifically, the boron-over-carbon and boron-over-oxygen flux ratios were recently published in the energy range from 10 GeV/n to 5.6 TeV/n, using 6 years of accumulated statistics, and are reported in Fig. 2.24 [8]. Boron nuclei are considered *secondary* CRs, produced through the spallation process from heavier *primaries* such as carbon and oxygen when they interact with the interstellar medium. Consequently, the B/C and B/O flux ratios carry crucial information on the propagation mechanisms of CRs in the Galaxy. Previous results reported the hint of a deviation from a single power law model in the aforementioned spectral ratios, but with low significance. The DAMPE results show for the first time the evidence of a hardening in both spectra at around 100 GeV/n, evaluated performing a broken power law fit, shown in Fig. 2.24 with a red dashed line. The aforementioned fits result in a significance of 5.6σ and 6.9σ for the presence of a break in the B/C and B/O flux ratios respectively. Considering these results, apart from delineating the propagation mechanisms, the study of B/C and B/O gives indications on the nature of CR sources (e.g. hints about the grammage accumulated in the SNR) and eventual re-acceleration processes happening while high-energy particles travel in the interstellar medium.

With more than 7 years of operation, the DAMPE experiment provided valuable insights into DM models, γ-ray physics, and electron-positron sources. Moreover, results on charged nuclei opened new challenges in our understanding of CR physics and of our galaxy. The DAMPE satellite is currently taking data and its sub-detectors are fully functional, promising more breakthrough results to come in the next months and years. The next chapter will focus on the p+He spectral measurement, specifically describing data selection and acceptance evaluation.

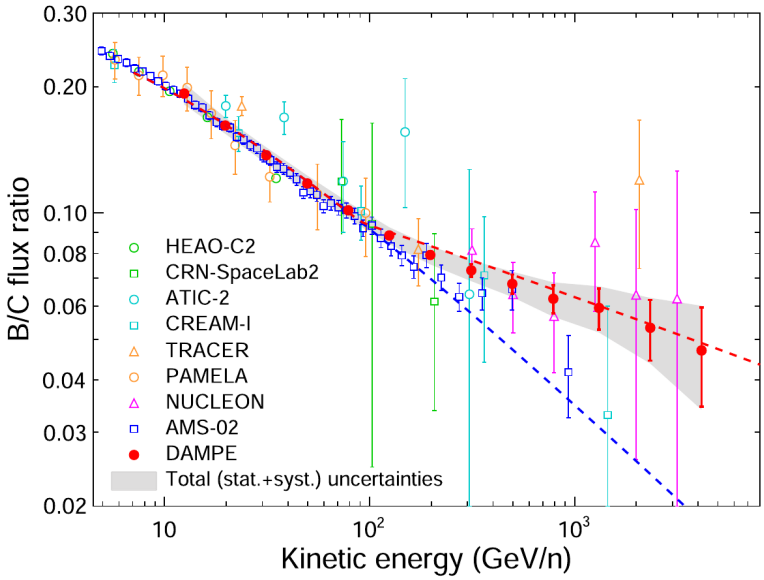

(a)

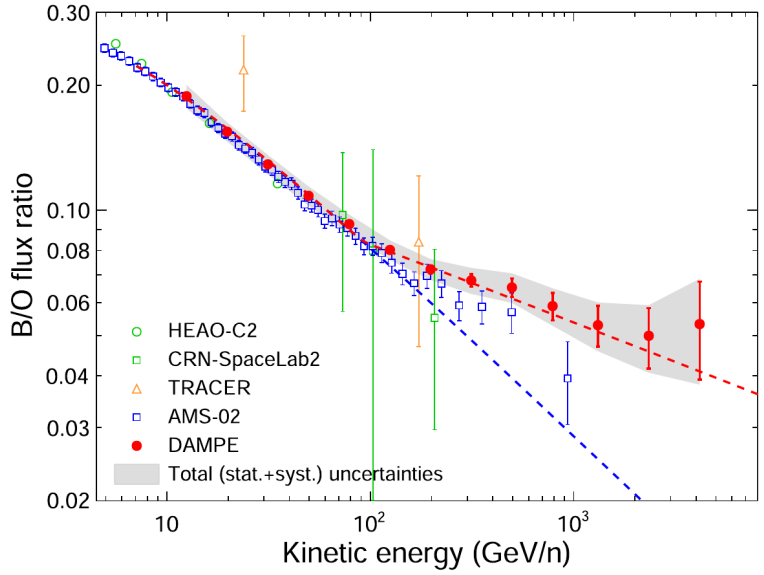

(b)

Figure 2.24: DAMPE results on (a) Boron-over-Carbon and (b) Boron-over-Oxygen flux ratios in red circles, compared with previous experimental results. Statistical uncertainties are represented by error bars, while the grey-shaded band represents the quadratic sum of statistical and systematic uncertainties. The spectral fit is performed using a broken power law (red dashed line) and a single power law (blue dashed line) functions, showing the evidence of a break at $\sim$ 100 GeV/n [8].

Chapter 3

Proton+helium event selection

In the energy range of interest for DAMPE, proton and helium are the most abundant species. Their combined selection allows having higher statistics with respect to selecting proton or helium alone, without encountering any particular issues with contamination/purity of the data sample. High statistics imply the possibility of extending the energy spectrum to the highest energies achievable by the DAMPE instrument. In order to perform the p+He spectral measurement, it's fundamental to select a sample of interest among all the events collected from the satellite during its operation. Afterwards, the identification of proton+helium will follow.

The proton+helium event selection procedure will be the subject of this chapter, starting from a description of the data used, continuing with the definition of good-quality CR events, and concluding with the identification of protons and helium nuclei while quantifying also the possible background in the selected sample.

3.1 Data samples

DAMPE is able to collect $\sim$ 5 million of cosmic-ray events per day in the energy range from a few GeV to hundreds of TeV. In Fig. 3.1 the daily event count of DAMPE is shown, with a few spikes representing the days in which the data acquisition has some interruptions or excess of triggers. The same event count plot is presented in Fig. 3.2 divided by energy range.

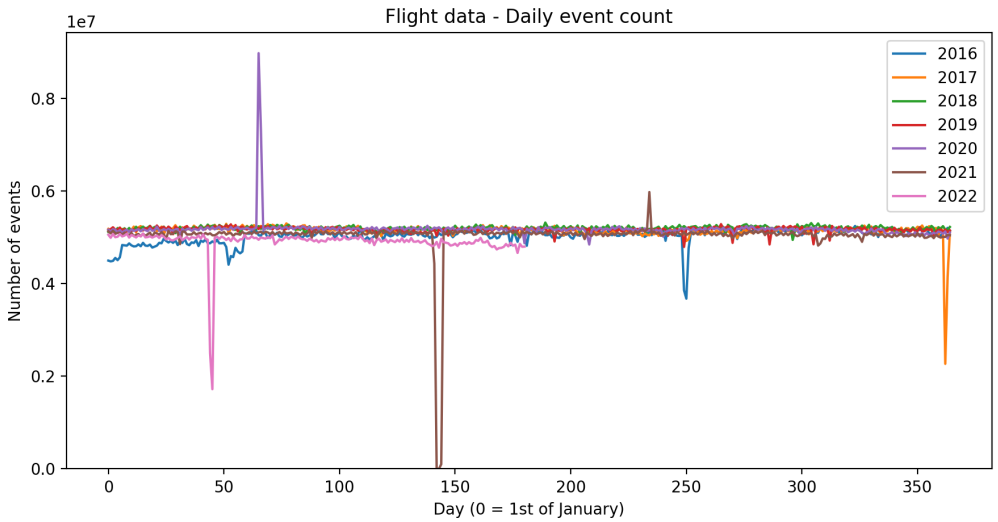

Figure 3.1: DAMPE daily event count, divided per year. The spikes indicate days in which the DAMPE instrument was under test or calibration, as well as a few instances where the data acquisition was interrupted.

3.1.1 Flight data

This work is based on 72 months of flight data, namely the period from the beginning of January 2016 until the end of December 2021. From this data sample, the events collected while crossing the South Atlantic Anomaly (SAA) region are excluded (more details on this topic can be found in section 2.7 and in Fig. 2.18). Additionally, the total operation time is affected by other factors such as the instrumental dead time, which is 3.0725 ms per event corresponding to $\sim$ 18% of the operation time, and the on-orbit calibration time, which is $\sim$ 1.6% of the operation time. Furthermore, a giant solar flare was recorded in the period between September 9 and September 13, 2017[1], influencing the normal operation of the satellite. Considering all these contributions, the remaining total live time in the analysis is $\sim 14.5\times 10^7$ s, which corresponds to $\sim$ 76% of the total operation time.

3.1.2 Monte Carlo simulations

As mentioned before, MC data are important to understand and predict the detector response to different particles, thus they are fundamental for physics analyses. For this work, MC data are produced using the DAMPE software with GEANT4 version 4.10.5 [58]. The GEANT4 toolkit gives the possibility to use various hadronic interaction models. Specifically, two models are used for the computation of the p+He

[1] `https://solarflare.njit.edu/datasources.html`

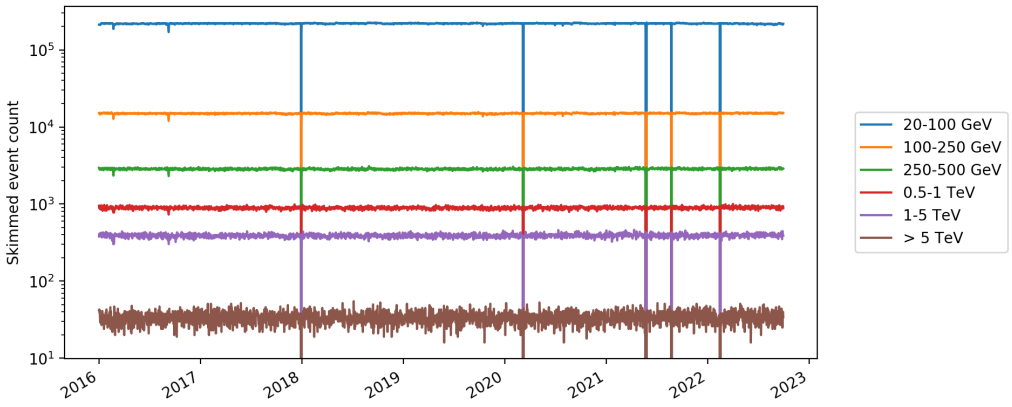

Figure 3.2: DAMPE daily event count, divided per BGO energy range.

energy spectrum: the FTFP_BERT[2] GEANT4 physics list, and EPOS-LHC [71] by linking it to GEANT4 with the Cosmic Ray Monte Carlo (CRMC) package[3] [72]. The MC samples used in this analysis are listed in table 3.1 and 3.2.

Table 3.1: Proton and helium MC FTFP_BERT samples used in this analysis.

	Energy range (TeV)	Number of events (M)
Helium	0.01 – 0.1	204.2
	0.1 – 1.0	101.5
	1.0 – 10	99.5
	10 – 100	99.4
	100 – 500	18.7
Proton	0.01 – 0.1	2068.2
	0.1 – 1	1056.8
	1 – 10	252.6
	10 – 100	117.4

Table 3.2: Proton and helium MC EPOS-LHC samples used in this analysis.

	Energy range (PeV)	Number of events (M)
Helium	0.5 – 1	6.1
Proton	0.1 – 1	15.1

Additionally, in order to evaluate the effect of using these specific hadronic models, more MC samples were produced: the FLUKA 2011.2x [73] software is

[2] https://geant4-userdoc.web.cern.ch/UsersGuides/PhysicsListGuide/html/reference_PL/FTFP_BERT.html

[3] https://web.ikp.kit.edu/rulrich/crmc.html

used for helium with the DPMJET3 model [74–76], and the QGSP_FTFP_BERT GEANT4[4] physics list is used for protons. These samples are listed in table 3.3 and 3.4. More details will follow in the section dedicated to the systematic uncertainty evaluation.

Table 3.3: Helium MC FLUKA samples used to evaluate the uncertainty on the hadronic model.

	Energy range (TeV)	Number of events (M)
Helium	0.01 – 0.1	168.7
	0.1 – 1	94.1
	1 – 10	86.6
	10 – 100	148.9
	100 – 500	19.7

Table 3.4: Proton MC QGSP_FTFP_BERT samples used to evaluate the uncertainty on the hadronic model.

	Energy range (TeV)	Number of events (M)
Proton	0.01 – 0.1	2029.5
	0.1 – 1	1186.8
	1 – 10	233.2
	10 – 100	22.9

3.2 Event selection

Flight data and MC data are stored in the same format and reconstructed using the same algorithms (see section 2.8.1). This implies that the same event selection can be applied to both of them. Specifically, starting from the data sets described in the previous paragraphs (3.1.1 and 3.1.2), a so-called *pre-selection* is applied to select good-quality events. The pre-selection is followed by the reconstruction and selection of the best track among many candidates, thus identifying the same event in different sub-detectors. The data sample surviving pre-selection and track selection will be used to identify the proton+helium candidate. A detailed description of the event selection procedure will follow.

[4] `https://geant4-userdoc.web.cern.ch/UsersGuides/PhysicsListGuide/html/reference_PL/QGSP_BERT.html`

3.2.1 Preselection

The first level of event filtration is the pre-selection which is mainly determined by the energy deposited in the BGO and consists of the following criteria:

- The high energy trigger (HET) activation is required in order to ensure the selection of events initiating a shower at the top of the calorimeter. More details on the trigger are given in section 2.7;
- The effect of the geomagnetic rigidity cutoff on the DAMPE data taking was studied [77, 78] and it was found to be relevant for energy lower than ~ 20 GeV when proton and helium are considered. For this reason, the selected events should deposit energy larger than 20 GeV in the BGO;
- Selected particles and nuclei should cross all the DAMPE sub-detectors. Consequently, a criterion is applied to reject most of the side-entering events, which consists of requiring an energy deposition in a single BGO layer lower than 35% of the total energy deposited;
- Another requirement is that the shower should be laterally contained within the BGO. This is achieved by asking that the distance between the calorimeter center and the central axis of the shower is less than 280 mm, which means that the shower axis is contained in a central region that covers 93% of the calorimeter width (see Fig. 3.3);
- Additionally, events with maximum energy deposition at the outermost BGO bars are rejected;
- Finally, a top-down development of the shower is required, with the condition of having an energy deposition in the first two BGO layers smaller than the energy deposited in the third and fourth layers: $E_{L1} + E_{L2} < E_{L3} + E_{L4}$.

3.2.2 Track selection

Events surviving the pre-selection cuts will go through their track reconstruction process using the track pattern recognition algorithm in the STK [79]. Each of these events contains many tracks generated by the primary particle and by the secondaries produced during the interactions with the sub-detectors. In order to select

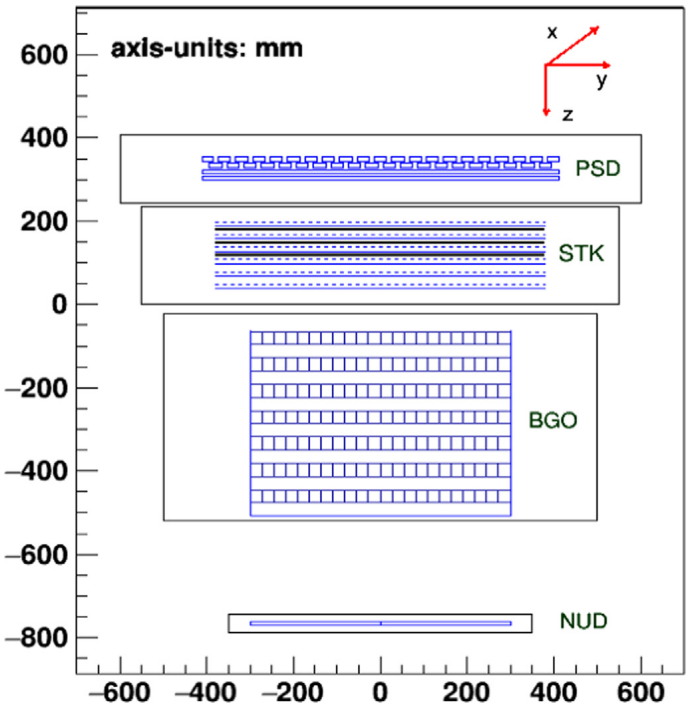

Figure 3.3: Scheme of the DAMPE detector with its dimensions in mm [59].

the best track a series of cuts is applied, including also the combination between the STK signal and the one recorded by other sub-detectors, specifically the BGO and the PSD. The applied cuts are described below:

Good quality track

- Considering that for every event there could be clusters in the STK induced by the interaction of both secondary and primary particles, their combination will result in a high χ^2/ndof (typically mean value of χ^2/ndof $\sim$ 35 and RMS of 25), as shown in Fig. 3.4. The events are selected by requiring that the STK track is reconstructed with a χ^2/ndof lower than 25. This value is chosen as an adequate compromise between keeping the bulk of statistics while ensuring a good quality of the reconstructed track.

- Since the STK can be used also for charge measurement, the presence of at least one cluster in the first STK layer is required, to avoid particle's interaction with the tungsten plate placed on the second layer.

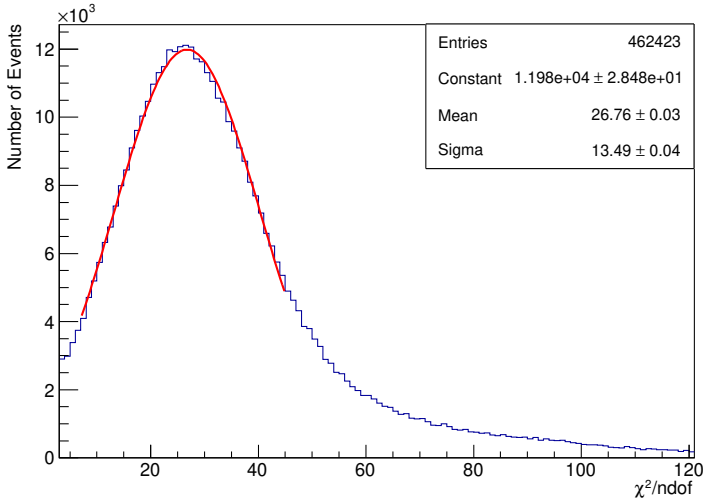

Figure 3.4: Distribution of the χ^2/ndof for reconstructed helium tracks, in the energy range from 10 TeV to 100 TeV. The distribution is similar if different energies are considered, also for protons. A Gaussian fit of the peak is shown with the red line, and the resulting parameters are reported.

BGO-STK match

- The track recorded in the STK and the axis of the shower measured in the BGO should have a difference in zenith angle lower than 25°;
- The distance between the projections of STK track and BGO track on the first layer of the BGO has to be lower than 60 mm;
- The distance between the first cluster in the STK and the projection of the BGO track is required to be lower than 200 mm.

PSD-STK match

- A PSD fiducial volume which covers the $\sim$ 97% of the PSD active area (in the central region) is defined. Specifically, the size of this volume is [-400, 400] mm (see Fig. 3.3), and the STK track projection is required to be contained in this volume.

The effect of the track selection in the X-view is illustrated in Fig. 3.5.

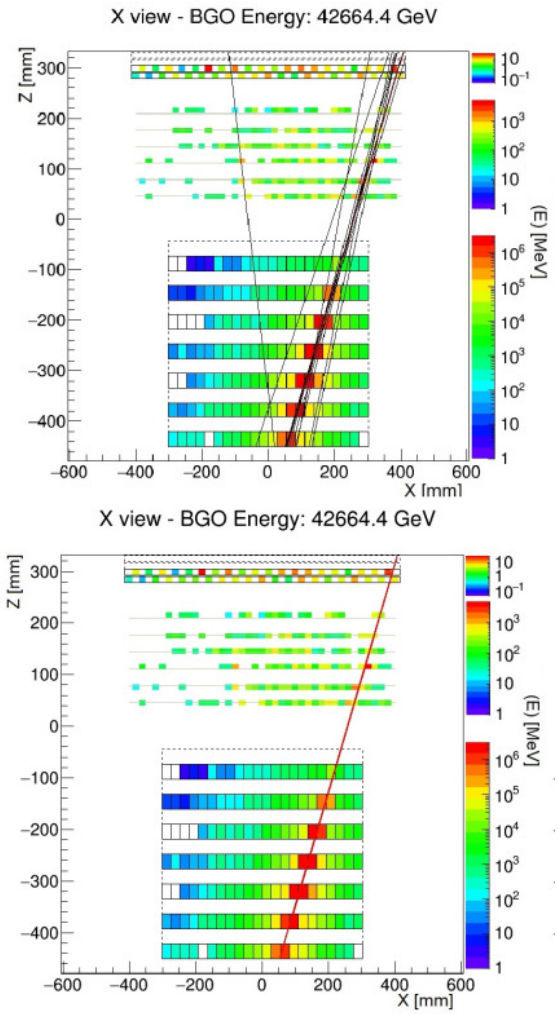

Figure 3.5: Event display of DAMPE, showing an event with deposited energy of $\sim$ 42.66 GeV, in the X-view of the detector. The upper panel shows the numerous reconstructed tracks before the track selection procedure. In the bottom plots, only one track is chosen and it is represented with a red line.

3.2.3 Selection of proton and helium

Proton and helium nuclei are separated from other nuclear species by using the PSD (see section 2.3). For this reason, a specific procedure focused on the PSD is used to select proton and helium candidates:

- Since both PSD layers (PSD_X and PSD_Y) are used for this analysis, the first requirement is to have a signal on both of them. Afterwards, the total PSD deposited energy (hereafter *PSD Global energy*) is defined as follows:

$$\text{PSD Global energy} = \frac{PSD_X + PSD_Y}{2}; \tag{3.1}$$

- Protons and electrons/positrons will behave in the same way in the PSD. Consequently, a specific cut is applied to remove electrons and positrons, using the imaging capabilities of the BGO (more details will follow in section 3.4);

- The signal in the PSD is corrected considering light attenuation, detector alignment, and incident angle [52, 80]. These corrections make the signal proportional to Z^2 (with Z charge of the particle), in accordance with the Bethe-Bloch equation;

- Finally, proton and helium candidates are selected by looking at their energy deposition in the PSD (as described below), also taking into account the increase of the energy loss rate with energy.

Charge selection

The particle's charge and its primary energy determine the signal recorded in the PSD. It follows that the nuclei identification is performed by combining the information taken from the PSD with the one from the BGO. For this analysis, the PSD Global energy (defined in eq. 3.1) distribution is taken in different bins of energy deposited in the BGO (called *BGO Energy*), in a PSD energy window in which the signal of proton and helium is expected to be seen. Furthermore, in order to provide a better description of expected real data, the proton and helium MC samples are weighted with functions obtained by fitting the proton and helium AMS spectra [13, 14] respectively. The two peaks representing the proton and helium signal are fit with a Landau convoluted with a Gaussian function (*LanGaus*) in each BGO

energy bin. The Landau function describes fluctuations in energy loss of ionizing particles and the Gaussian is used to account for detector effects. The PSD Global energy distributions are reported in Appendix A and some representative plots are shown in Fig. 3.6 for MC, and in Fig. 3.7 for flight data, along with their LanGaus fits, in different bins of BGO energy.

The parameters extracted from the LanGaus fits (most probable value (MPV), Landau width and Gaussian sigma) are presented with respect to the BGO energy in Fig. 3.8 and 3.9. The dependence of the energy deposited per path length on the primary energy is taken into account by fitting the aforesaid parameters with a fourth-order polynomial function of the logarithm of the energy. The Gaussian sigma is almost not affected by the primary particle energy and for this reason, this value is fit with a constant function, shown in Fig. 3.10. The aforementioned result suggests that the energy deposit in the case of protons follows a simple Landau distribution, with a negligible Gaussian contribution. Nevertheless, the latter was found to be relevant for helium nuclei and is therefore kept in the fitting and charge selection procedure.

The comparison between the parameters found for MC and flight data shows a disagreement at high BGO energy, probably due to the MC overestimating the back-scattering effect. For this reason, a correction is applied to the MC histograms. A function called *smearing function* is used to fill the MC PSD histograms with a corrected PSD energy ($E_{PSD}^{MC,corr}$) depending on the BGO energy value:

$$E_{PSD}^{MC,corr} = \left(E_{PSD}^{MC} - f'_{MPV,MC}(E_{BGO})\right) \frac{g'_{\sigma,DATA}(E_{BGO})}{g'_{\sigma,MC}(E_{BGO})} + f'_{MPV,DATA}(E_{BGO}) \quad (3.2)$$

where $f'_{MPV,MC}(E_{BGO})$ and $f'_{MPV,DATA}(E_{BGO})$ are the polynomial functions used to fit the MPV values for MC and flight data respectively, $g'_{\sigma,MC}(E_{BGO})$ and $g'_{\sigma,DATA}(E_{BGO})$ represent the sigma value for MC and flight data which is calculated as $\sqrt{Width^2 + \sigma_{Gaus}^2}$. After applying the smearing correction, MC and flight data are in good agreement as can be seen in Figures 3.11, 3.12, 3.13, and in the histograms in Fig. 3.14. The corrected polynomial functions are used to define a charge selection cut for the proton+helium analysis, which is the interval from MPV_p - 2σ to MPV_{He} + 6σ, shown with dashed lines in Fig. 3.14, and in Fig. 3.15 superimposed to the scatter plot of PSD energy versus BGO energy. The chosen interval was optimized to have more proton and helium statistics while keeping low the

contamination from other nuclei (more details will follow in section 3.4).

3.3 Effective acceptance

As described in section 3.1.2, along with data from the satellite, MC data are used in this analysis. Specifically, a certain number of events $N(E_T^i)$ is generated in the i-th bin of primary energy E_T, with a geometrical factor G_{gen} defined as follows:

$$G_{gen} = \int_{S,\Omega} \mathrm{dsd}\Omega, \tag{3.3}$$

where S is the surface and Ω the solid angle. The MC data are generated using a geometrical factor G_{gen} corresponding to a half-sphere, where the DAMPE detector is positioned at the center, and the generation surface assumes an isotropic cosmic ray flux. Afterwards, selection cuts are applied as explained before and only part of these events, called $N(E_T^i, sel)$, will survive. The selection cut efficiencies can be expressed as:

$$\varepsilon^i(E_T^i) = \frac{N(E_T^i, sel)}{N(E_T^i)} \tag{3.4}$$

and are described in section 4.4.1 (next chapter), in order to make a comparison between MC and flight data, eventually evaluating the systematic uncertainty originating from their possible difference. An example of selection cut efficiency is given in Fig. 3.16 where the track reconstruction efficiency is reported for MC and flight data with the MC/data ratio shown in the bottom panel. As aforesaid, additional information on the efficiency evaluation procedure and on their possible influence on the systematic uncertainties will be given later. Combining the efficiencies with the geometrical factor, the effective acceptance A_{acc}^i can be computed as follows:

$$A_{acc}^i(E_T^i) = G_{gen} \times \frac{N(E_T^i, sel)}{N(E_T^i)}. \tag{3.5}$$

The MC generation surface (G_{gen}) has a radius r of 1.38 m for protons and 1.0 m for helium and heavier nuclei. For this reason, in the calculation of the final acceptance for the p+He spectrum a correction factor $G_{gen,He}/G_{gen,p}$, is applied to the helium MC events. The effect of different selection cuts on the acceptance is shown in Fig. 3.17, while the final acceptance used for this analysis is presented in Fig. 3.18, with respect to the primary particle energy.

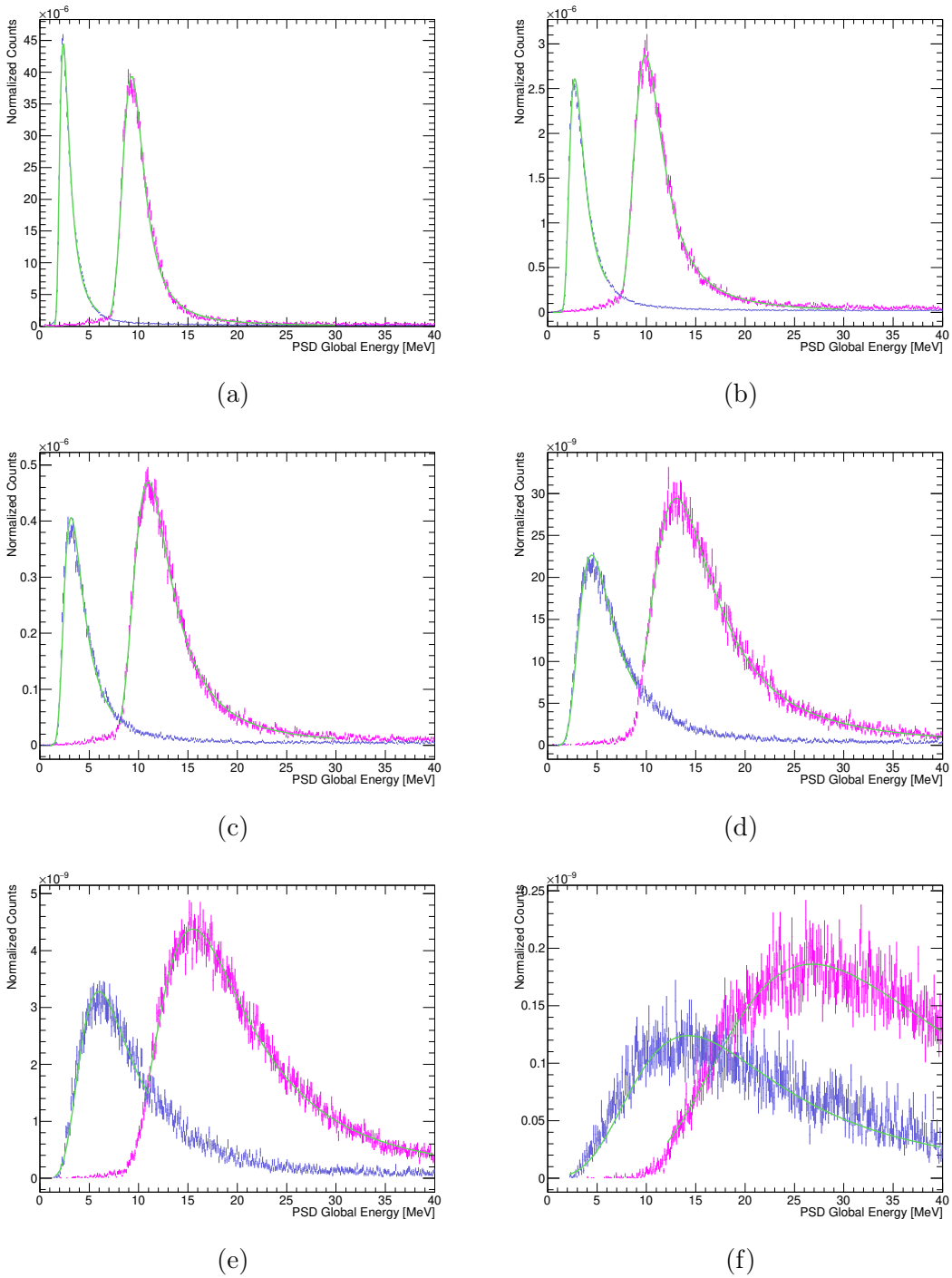

Figure 3.6: Distributions of simulated proton and helium PSD Global energy, for various BGO energy bins: (a) 63 GeV - 100 GeV, (b) 251 GeV - 398 GeV, (c) 630 GeV - 1000 GeV, (d) 2.5 TeV - 4.0 TeV, (e) 6.3 TeV - 10.0 TeV, (f) 31.6 TeV - 100.0 TeV. The MC distributions of proton (in blue) and helium (in magenta) are shown, along with their LanGaus fits (green lines). The average increase of the energy loss rate with primary energy is clearly visible.

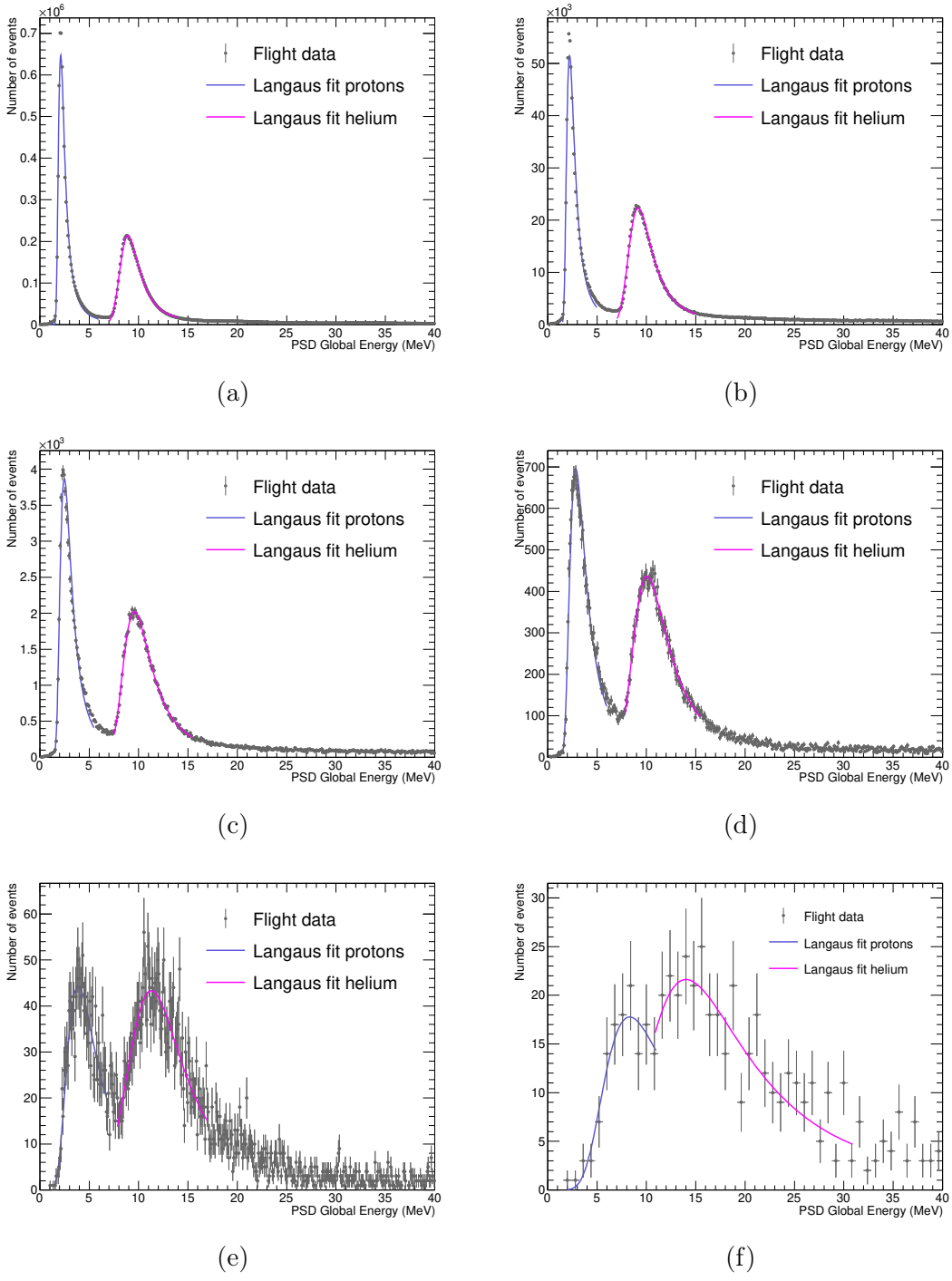

Figure 3.7: Distributions of PSD Global energy in flight data, for various BGO energy bins: (a) 39 GeV - 63 GeV, (b) 158 GeV - 251 GeV, (c) 630 GeV - 1000 GeV, (d) 1.6 TeV - 2.5 TeV, (e) 6.3 TeV - 10.0 TeV, (f) 31.6 TeV - 100.0 TeV. The flight data distributions of proton and helium are shown with grey points, along with their LanGaus fits, in blue for protons and magenta for helium.

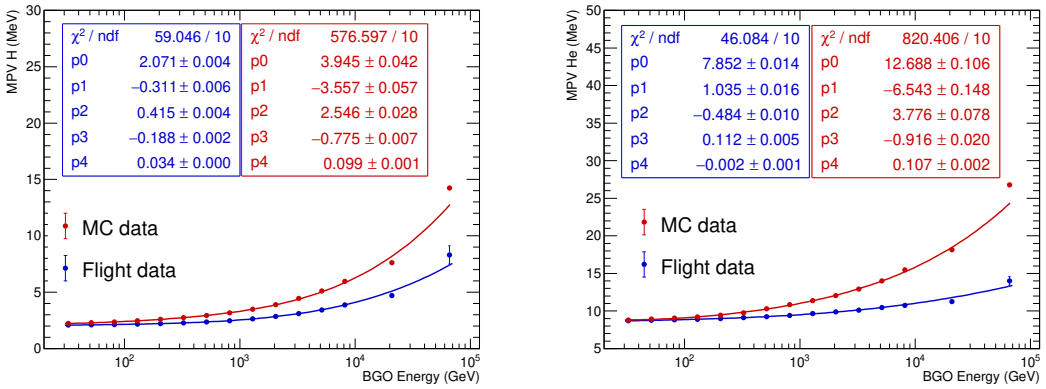

(a) (b)

Figure 3.8: Most probable value (MPV) of the LanGaus fit for (a) protons and (b) helium with respect to the energy deposited in the BGO. MC data (in red) and flight data (in blue) are shown, along with their fit functions and the parameters extracted from the fit.

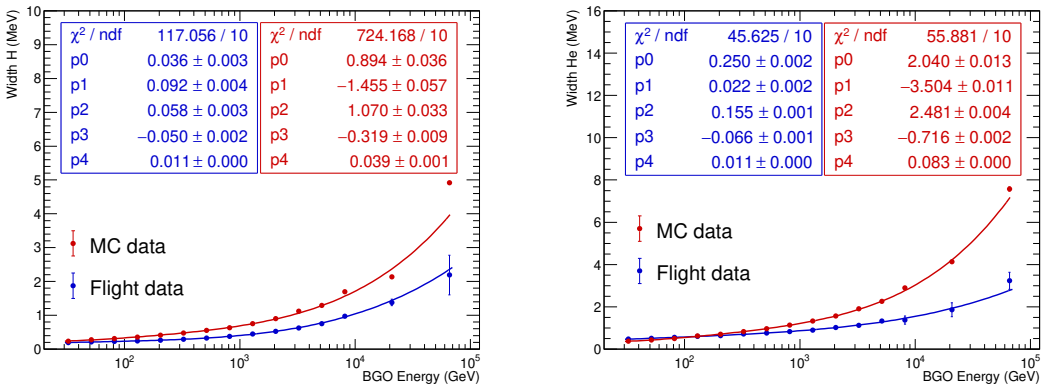

(a) (b)

Figure 3.9: Width of the LanGaus fit for (a) protons and (b) helium with respect to the energy deposited in the BGO. MC data (in red) and flight data (in blue) are shown, along with their fit functions and the parameters extracted from the fit.

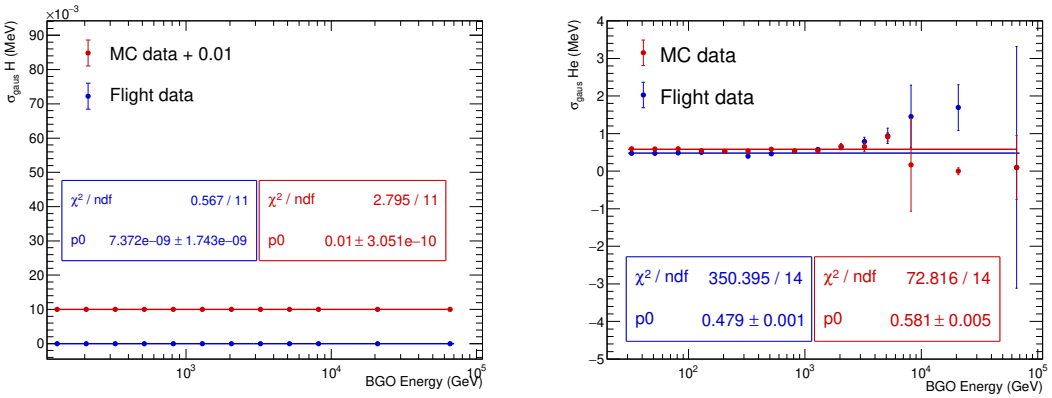

(a) (b)

Figure 3.10: Gaussian sigma of the LanGaus fit for (a) protons and (b) helium with respect to the energy deposited in the BGO calorimeter. MC data (in red) and flight data (in blue) are shown, along with their fit functions and the parameters extracted from the fit. In the case of protons, the MC data are shifted by a constant factor of +0.01 to separate them from flight data. The Gaussian sigma is negligible for protons but significant for helium, and for consistency, the LanGaus method is kept for both nuclei.

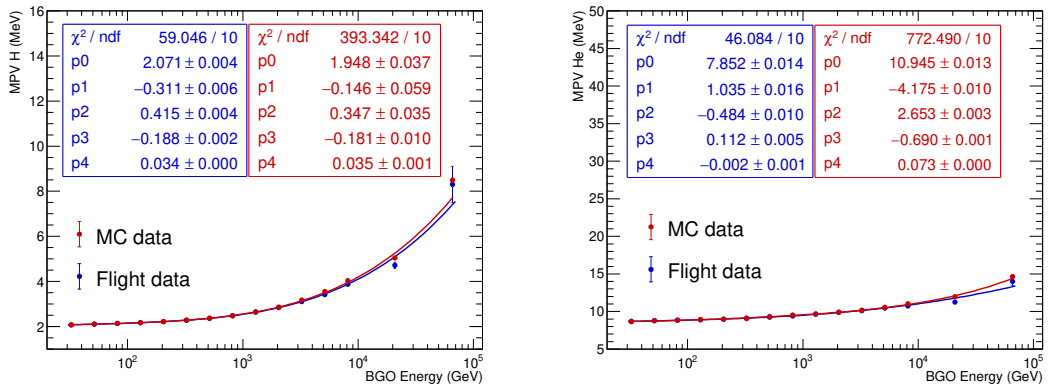

(a) (b)

Figure 3.11: Most probable value (MPV) of the LanGaus fit for (a) protons and (b) helium with respect to the energy deposited in the BGO, after the smearing correction. MC data (in red) and flight data (in blue) are shown, along with their fit functions and the parameters extracted from the fit.

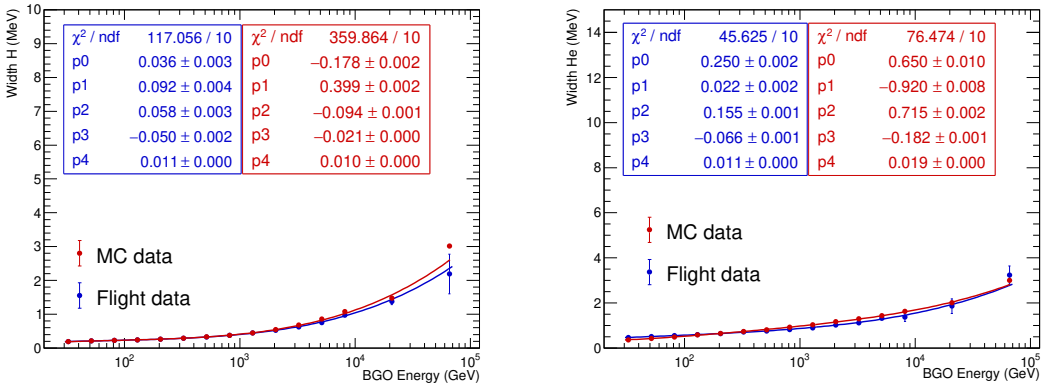

(a) (b)

Figure 3.12: Width of the LanGaus fit for (a) protons and (b) helium with respect to the energy deposited in the BGO, after the smearing correction. MC data (in red) and flight data (in blue) are shown, along with their fit functions and the parameters extracted from the fit.

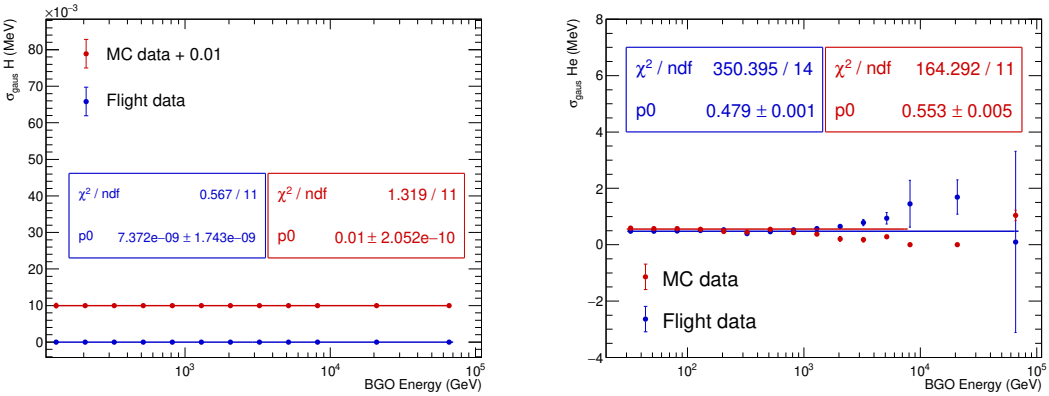

(a) (b)

Figure 3.13: Gaussian sigma of the LanGaus fit for (a) protons and (b) helium with respect to the energy deposited in the BGO calorimeter, after the smearing correction. MC data (in red) and flight data (in blue) are shown, along with their fit functions and the parameters extracted from the fit. In the case of protons, the MC data are shifted by a constant factor of +0.01 to separate them from flight data. The Gaussian sigma is negligible for protons but significant for helium, and for consistency, the LanGaus method is kept for both nuclei.

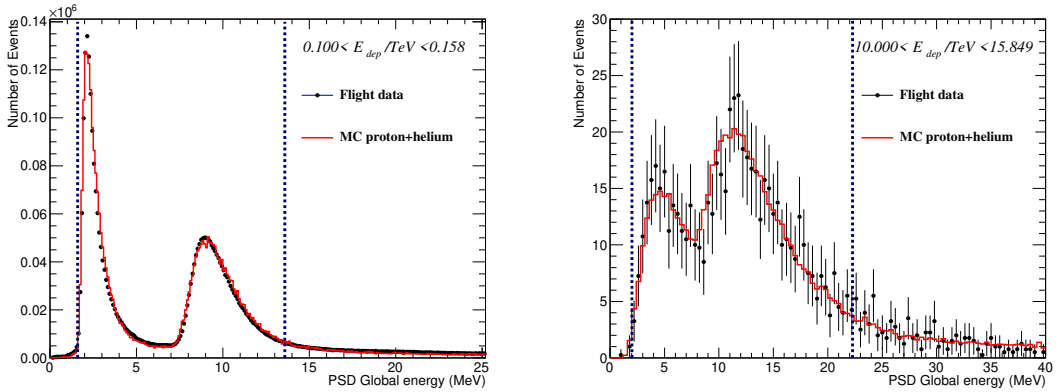

(a) (b)

Figure 3.14: Distributions of PSD global energy for events with deposited energy in the BGO calorimeter in the ranges (a) 100–158 GeV, (b) 10.0–15.8 TeV. Flight data are shown with black points, together with MC data of proton+helium, in red. The blue vertical dashed lines represent the charge selection ranges for p+He.

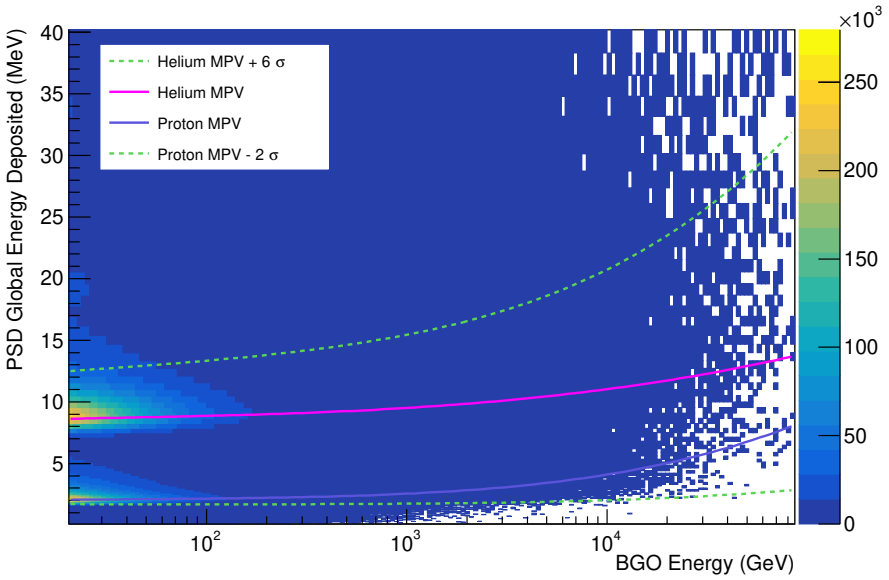

Figure 3.15: Scatter plot of the PSD Global energy with respect to the BGO energy for flight data. The blue and magenta lines represent the polynomial functions used to fit the MPV values of proton and helium respectively, while the green dashed lines represent the p+He charge selection range.

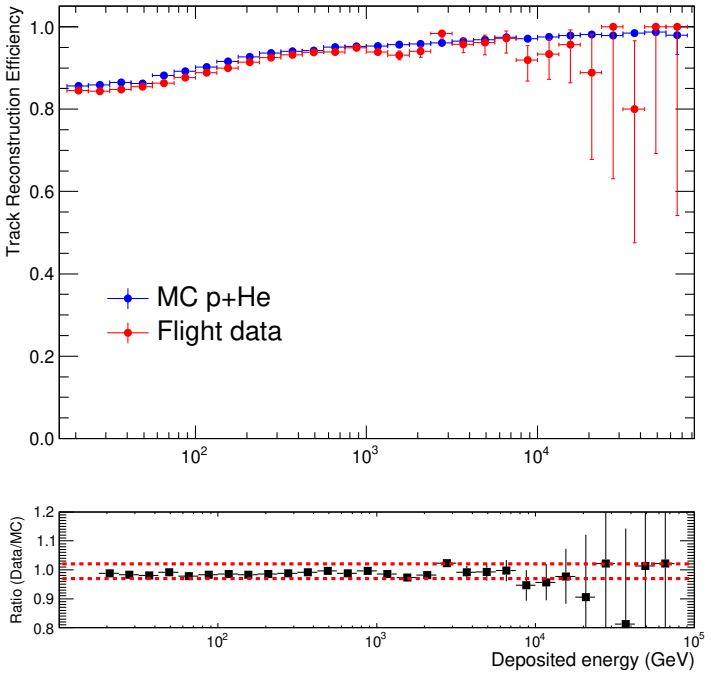

Figure 3.16: Track selection efficiency considering MC (in blue) and flight data (in red) of p+He. In the bottom panel, the ratio between MC and flight data is shown.

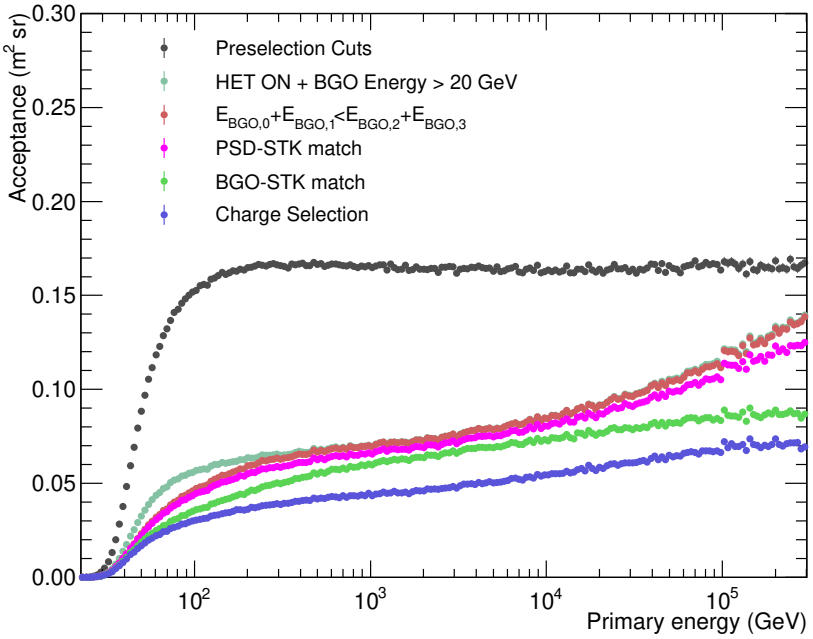

Figure 3.17: Effect of the selection procedure on the effective acceptance, for the proton+helium analysis.

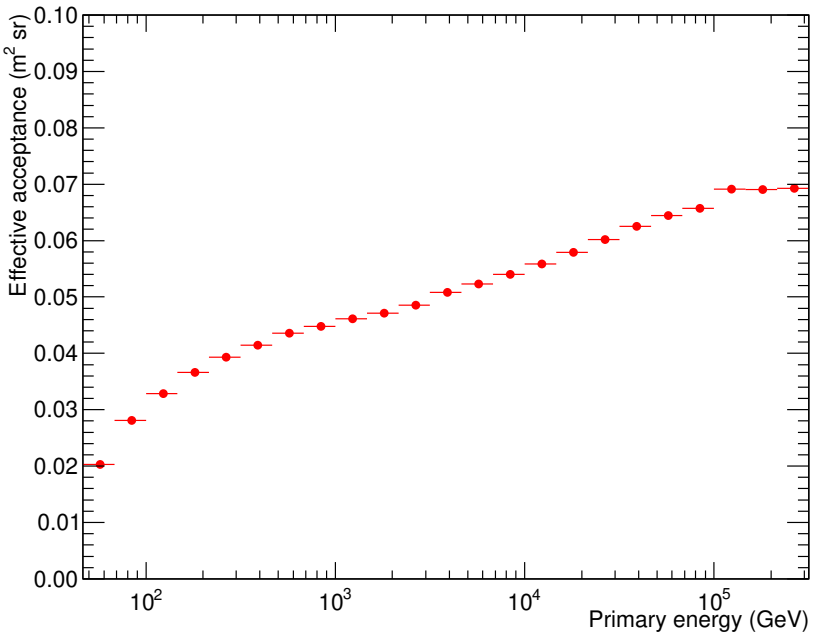

Figure 3.18: Effective acceptance of the p+He analysis obtained by using p and He MC samples, after applying all the selection cuts.

3.4 Background estimation

Selecting proton and helium together leads to having more statistics (with respect to proton and helium alone) while keeping the contamination from other particles low and avoiding the problems coming from helium contamination in the proton sample and viceversa. Specifically, if only protons are considered, the tail of the helium peak would enter the proton charge selection region, imposing the need for a compromise between the efficiency of the charge selection (how many proton events are kept over the total) and the remaining contamination. Additionally, electrons and positrons, which could be misidentified as protons in the PSD, constitute a source of background as well, which is rejected thanks to the BGO imaging capability (this is relevant also for the p+He background estimation and more details will follow in 3.4.1). On the other hand, selecting only helium means having a similar situation as for the proton one but in this case the tail of the proton peak would enter the charge selection region, requiring again to reach a compromise between selected helium events and background level. In this case, the additional background is constituted by heavier nuclei such as Lithium, which is much less abundant than protons and is therefore negligible. Considering the p+He charge selection, the background is composed of electrons, positrons, and Lithium nuclei, which could partially enter the

chosen charge selection window. The background estimation in the p+He analysis will be described in the next subsections.

3.4.1 Electrons/positrons background

The signal recorded in the PSD is the same for protons and electrons/positrons. For this reason, their discrimination is performed by looking at their shower development in the BGO (considering that the electromagnetic shower is expected to have a different morphology with respect to the hadronic one). Specifically for this analysis, events crossing the entire BGO are selected, and the shower spread in the i^{th} layer of the BGO is computed as follows:

$$(\text{Shower spread})_i = \text{RMS}_i = \sqrt{\frac{\sum_j (x_{j,i} - x_{\text{c},i})^2 E_{j,i}}{\sum_j E_{j,i}}}. \tag{3.6}$$

The previous formula represents the energy-weighted root-mean-square value of hit positions in the calorimeter. The terms $x_{j,i}$ and $E_{j,i}$ indicate the coordinates and deposited energy for the j^{th} bar in the i^{th} layer, while $x_{c,i}$ is the coordinate of the shower center for the i^{th} layer. The total shower spread on all 14 layers of the BGO ($\Sigma_i \text{RMS}_i$) is shown in Fig. 3.19 with respect to the fraction of energy deposited in the last BGO layer (F_{last}), after removing heavier nuclei with the PSD charge selection. From this figure, the discrimination capability of the DAMPE detector regarding protons and electrons-positrons using only the image in the BGO, is evident. Nonetheless, a dimensionless variable, ζ, is used to perform a better proton-electron separation, which is defined as:

$$\zeta = \mathcal{F}_{\text{last}} \times (\Sigma_i \text{RMS}_i/\text{mm})^4 \,/\, \left(8 \times 10^6\right) \tag{3.7}$$

An example of ζ distribution for selected events with BGO energy between 500 GeV and 1 TeV is shown in Fig. 3.20, along with the comparison between flight data and MC data, which shows a good agreement.

For this analysis, the condition $\zeta > 16$ is chosen to reject electrons. The contamination was evaluated in various BGO energy bins using flight data and MC simulations of proton, helium and electrons, as shown in Fig. 3.21. The MC data are initially simulated with a power-law energy spectrum following a E^{-1} energy dependence and subsequently re-weighted according to the AMS proton [13], helium [14],

and electron [64] spectra. The resulting background is ∼0.5% at 40 GeV of BGO energy, and it decreases with increasing energy (see Fig. 3.23).

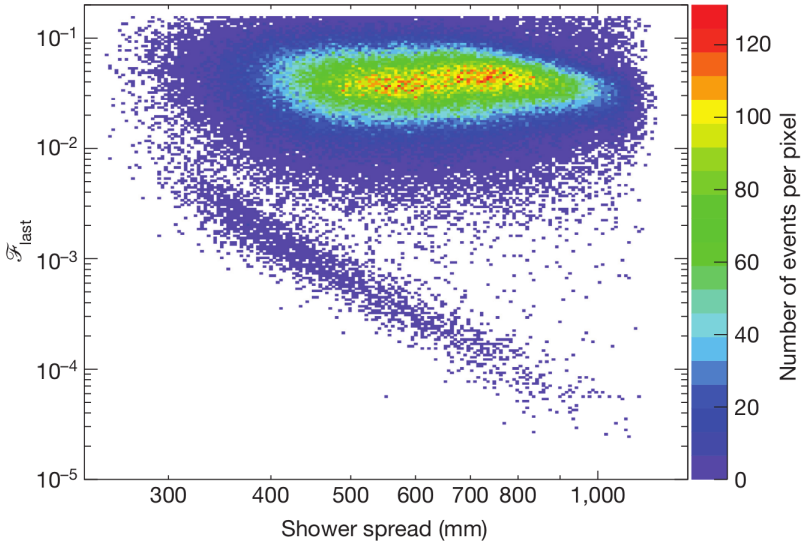

Figure 3.19: The fraction of energy deposited in the last BGO layer is presented with respect to the shower spread in the entire BGO for selected events with BGO energy between 500 GeV and 1 TeV [66].

3.4.2 Lithium background

In addition to electrons, a source of background for the p+He analysis comes from heavier nuclei such as Lithium (with charge Z = 3) which could enter the charge selection region and eventually be misidentified as helium. In order to evaluate the contamination caused by Lithium nuclei, a template fit method based on RooFit is used. Specifically, the entire selection procedure described in this chapter is applied to MC proton, helium, lithium, and flight data up to the charge selection, which is not used. Also in this case, the simulated MC data follow a power-law spectrum with a E^{-1} energy dependence and are re-weighted according to the AMS spectra for proton [13], helium [14], and lithium [16]. Afterwards, the MC histograms are corrected using the charge smearing formula and plotted together with the flight data, as shown in Fig. 3.22. Finally, the charge selection region for the p+He analysis is defined in different BGO energy bins (see red dashed line in Fig. 3.22), and the percentage of Lithium nuclei entering this window is evaluated.

The contamination from Lithium is found to be lower than 0.3% up to 10 TeV, and ∼1.6% for energies higher than 10 TeV as shown in Fig. 3.23. The background level was evaluated also by changing the charge selection window from 6σ to 5.5σ

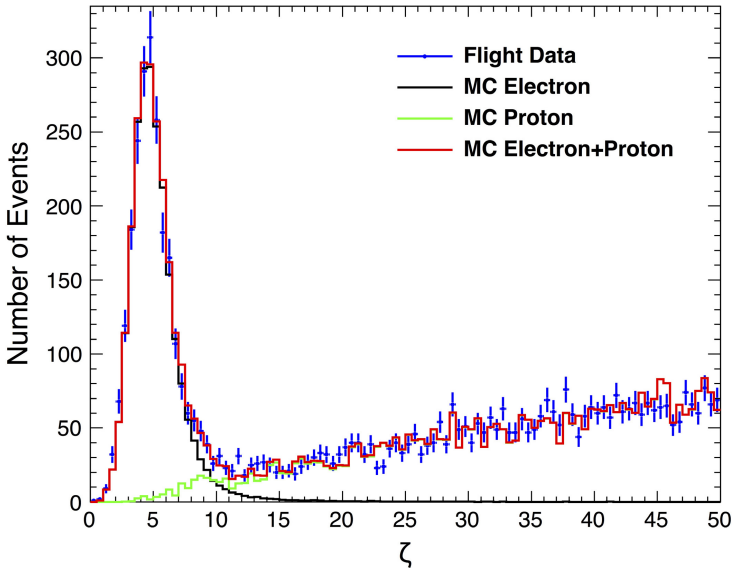

Figure 3.20: The ζ distribution is shown, comparing (blue points) flight data with (green histogram) MC protons, (black) MC electrons, and (red) their sum, for selected events with BGO energy between 500 GeV and 1 TeV [66].

and 5σ, resulting in a negligible difference in spectral shape and contamination level but lower p+He counts at high energy. Consequently, the choice of $+6\sigma$ was kept, as a good compromise between statistics and background level.

At the highest energies, it is difficult to distinguish the lithium peak because of the very low counts of flight data. For this reason, an upper limit is defined, looking at the highest possible contamination value considering 1σ error. The total contamination for this analysis is presented in Fig. 3.23.

This chapter outlined the event selection procedure performed starting from the $\sim$ 5 million CR candidates identified every day with the DAMPE detector and concluding with the selection of proton+helium nuclei, which is the focus of this work. In the next chapter, the detected p+He events will be subject to a further analysis aiming toward the energy reconstruction and the computation of the p+He energy spectrum.

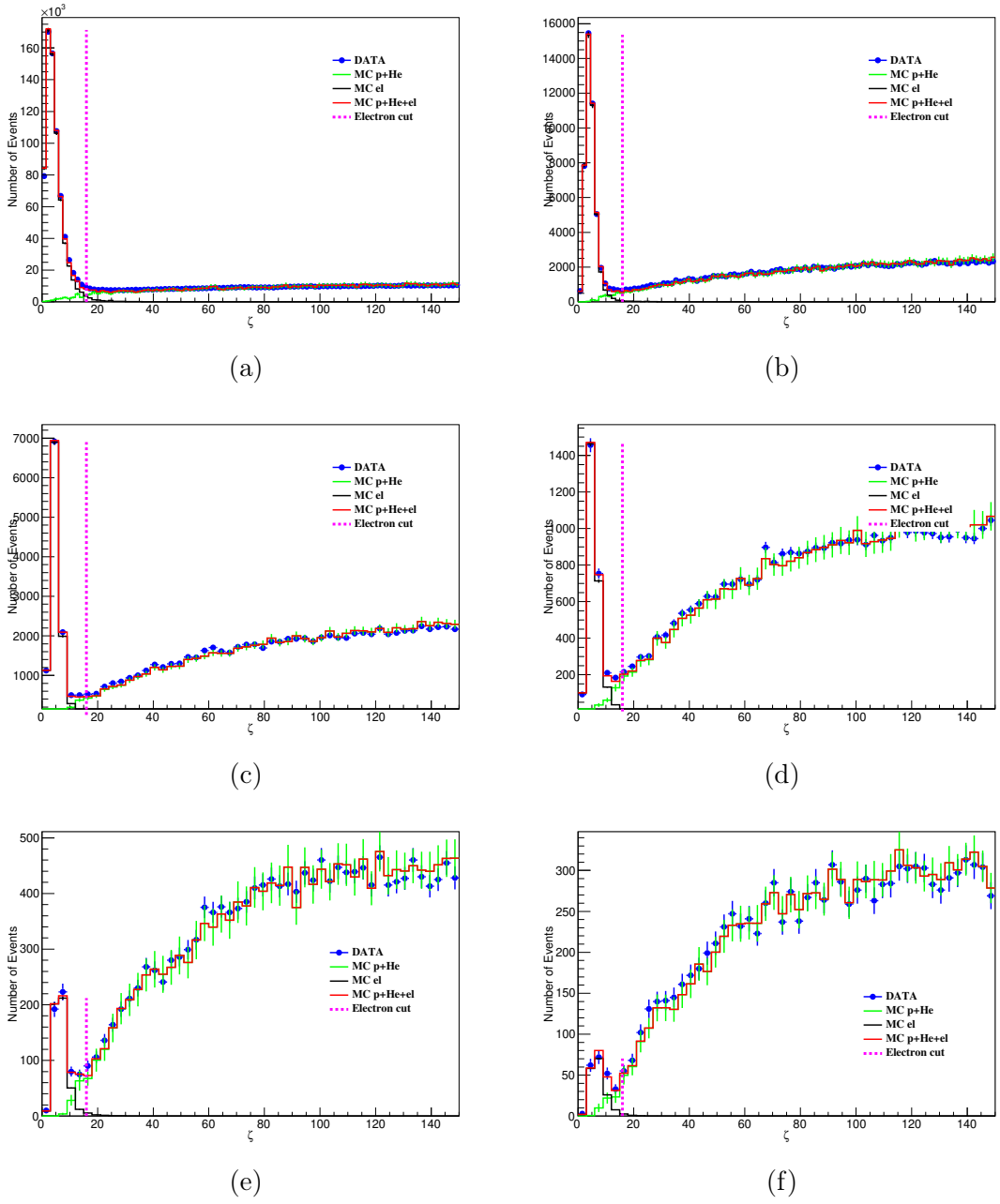

Figure 3.21: Template fits of the ζ distribution in various BGO energy bins: (a) 33 GeV - 47 GeV, (b) 133 GeV - 188 GeV, (c) 266 GeV - 375 GeV, (d) 531 GeV - 749 GeV, (e) 1.06 TeV - 1.50 TeV, (f) 1.5 TeV - 2.1 TeV. Flight data are shown with blue points, and histograms represent MC data for (black) electrons, (green) proton+helium, and (red) p+He+e^-.

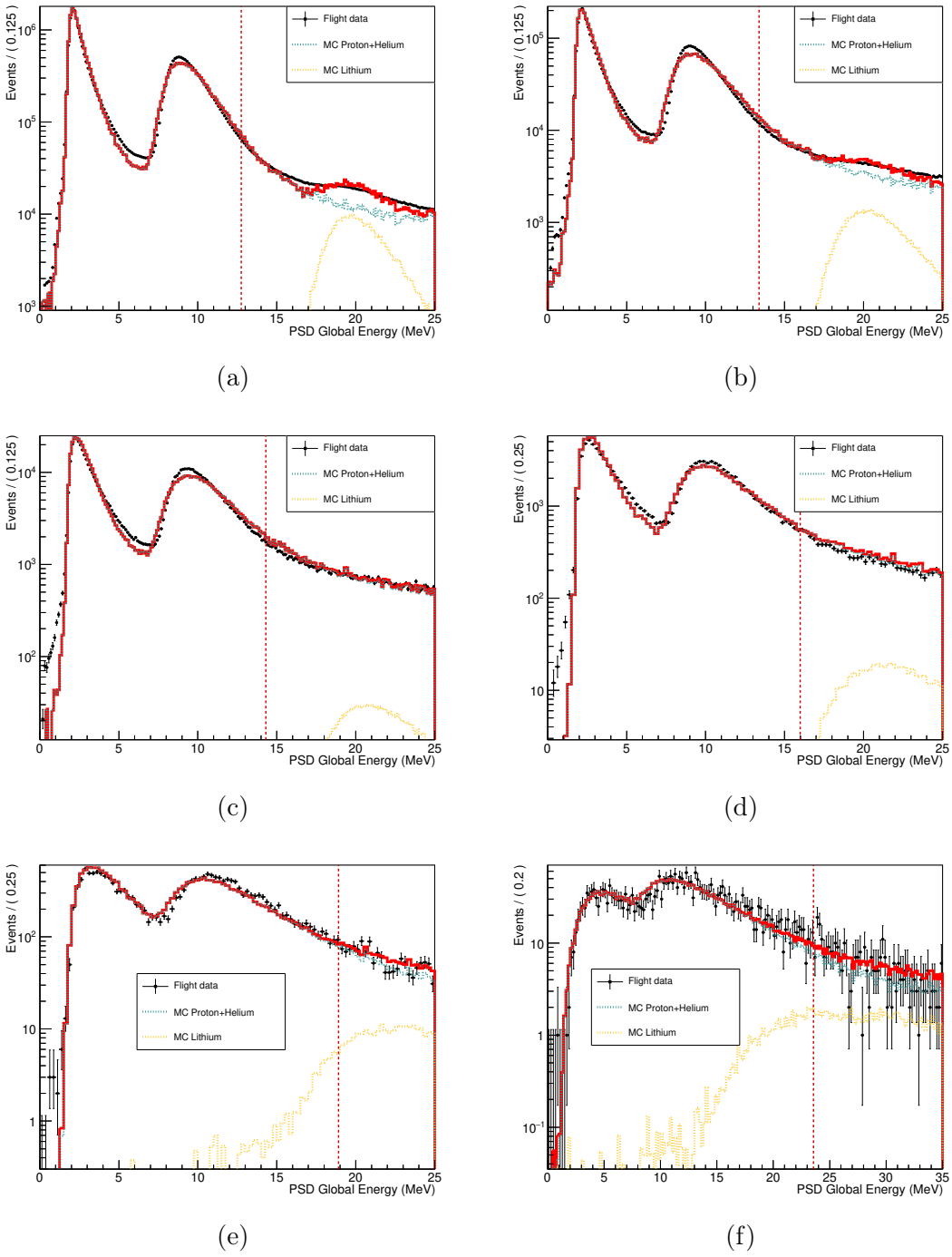

Figure 3.22: Template fit of the distribution of (black points) flight data, (green dashed line) MC p+He, (yellow dashed line) MC lithium, and (red line) MC p+He+Li, in various BGO energy bins: (a) 32 GeV - 100 GeV, (b) 100 GeV - 320 GeV, (c) 320 GeV - 1 TeV, (d) 1.0 TeV - 3.2 TeV, (e) 3.2 TeV - 10.0 TeV, (f) 10.0 TeV - 32.0 TeV.

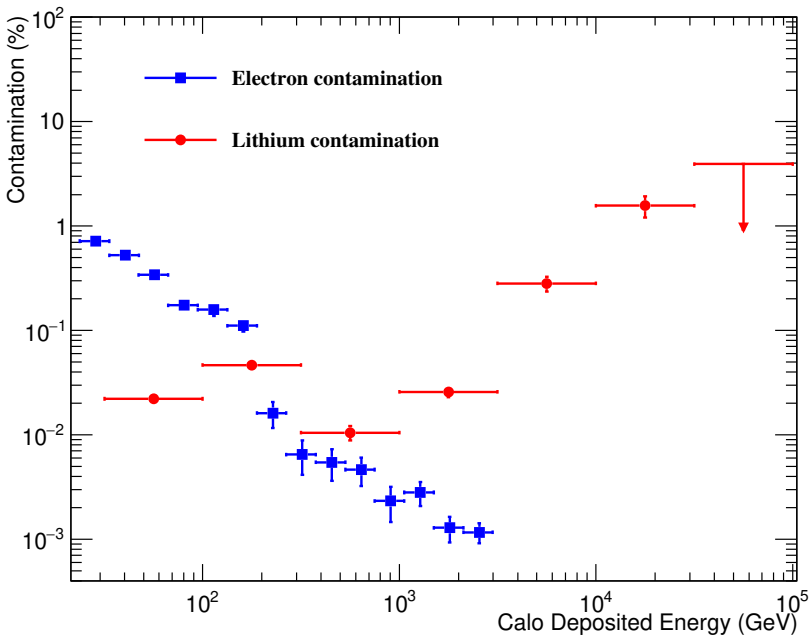

Figure 3.23: Background in the p+He spectrum, from electrons-positrons in blue, and lithium in red.

Chapter 4

Proton+helium: the energy spectrum

In the previous chapter, the selection of proton+helium events recorded by the DAMPE detector was described in detail. Starting from the selected events and the signal recorded in each of the DAMPE subdetectors, a few more steps are needed to obtain the p+He energy spectrum.

In this chapter the energy measurement procedure will be described, followed by the computation of the p+He flux along with the statistical and systematic errors associated with the spectral measurement and the analysis procedure. Afterwards, the comparison with the separate proton and helium spectra measured by DAMPE will be shown, along with the fit of the p+He spectrum. Finally, the p+He DAMPE spectrum resulting from this work will be compared with other direct and indirect experimental results.

4.1 Energy measurement and unfolding procedure

4.1.1 Corrections to the energy deposited in the calorimeter

When particles and nuclei deposit more than $\sim$ 4 TeV in a single BGO bar, some readout channels could saturate as indicated with white boxes in Fig. 4.1. It follows that a correction is needed to recover the signal of the saturated bars and have a good estimation of the energy deposited in the calorimeter. The details of this method are given in Appendix B and in [54].

On the other hand, when the energy deposition is lower than $\sim$ TeV, the BGO crystal response can be affected by the quenching effect [81]. Specifically, low-energy secondaries could deposit their energy after traveling very short distances and their

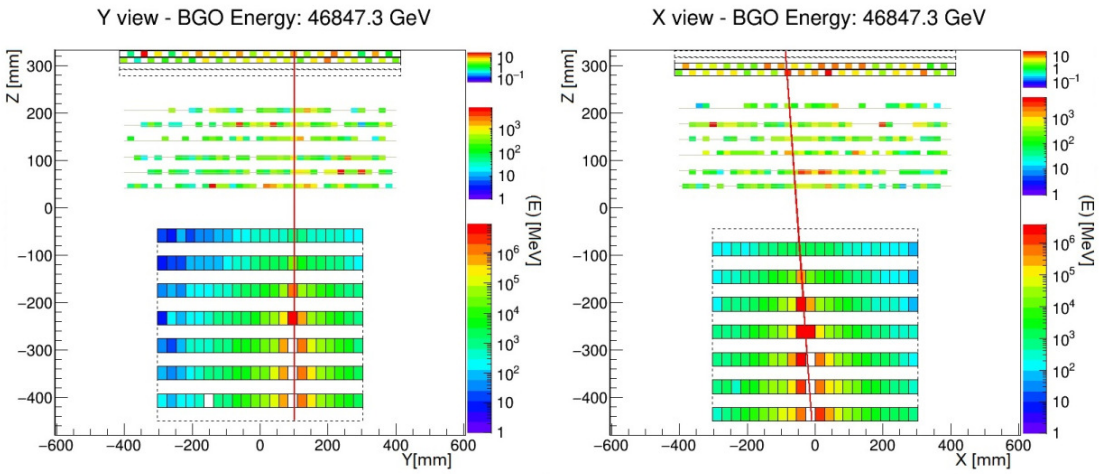

Figure 4.1: Event display of helium MC events in which the signal recorded from some BGO bars is saturated. The color scale represents the intensity of the signal in the logarithm of the energy. In the core of the shower, where the signal should be high, some boxes are white indicating a saturated signal.

energy could be underestimated because of Birk's quenching effect, which translates to a shower energy underestimation, as well. This effect has been studied for the BGO calorimeter of DAMPE with beam tests and flight data, resulting in a more significant effect for particles with high charge and low-velocity [82] while being negligible for protons. The correction parameters for helium nuclei were obtained and included in the MC simulations to investigate how Birk's quenching affects the deposited energy. The results show that this effect has its maximum for primary energies around $\sim$ 80 GeV, where the detected energy deposition would be $\sim$ 2% lower than it should be. The effect is added to the simulation by using the function below, which has been obtained by comparing helium MC events with and without the quenching effect.

$$E_{BGO} = \left[1 + 0.075 \cdot \left(\frac{E_{\text{true}}}{10\text{GeV/n}}\right)^{-0.38}\right] \cdot E_{BGO,SAT}. \tag{4.1}$$

The energy deposited by MC helium nuclei in the calorimeter of DAMPE was corrected using the previous formula, including the effect of saturation.

4.1.2 Shower containment in the calorimeter

The depth of the DAMPE calorimeter in terms of nuclear interaction lengths is $\sim$ 1.6, which implies partial containment of the hadronic showers inside the calorime-

ter volume. To investigate this effect, MC proton+helium selected events can be used. Specifically, the ratio between the deposited energy in the calorimeter and the primary energy, for various bins, is shown in Fig. 4.2. The mean value and the sigma of each distribution are extracted by fitting them using an asymmetric Gaussian function.

The parameters obtained with the aforementioned procedure are shown in Fig. 4.3 and 4.4 with respect to the primary energy of proton and helium nuclei.

It follows that the fraction of energy deposited in the calorimeter for protons and helium nuclei goes from $\sim 48\%$ at ~ 75 GeV to $\sim 32\%$ at ~ 75 TeV. This is expected considering that the depth of the calorimeter is ~ 1.6 nuclear interaction lengths and ~ 32 radiation lengths (X_0). Indeed, the first nuclear interaction happens on average at 2/3 of the calorimeter depth which corresponds to $\sim 20\ X_0$, and the remaining 1/3 of the calorimeter ($\sim 10\ X_0$) is sufficient to absorb the electromagnetic part of the hadronic shower ($\sim 1/3$ of the total energy of the primary particle). When low energy particles are considered, taking also into account the detector material that they traverse before reaching the BGO volume, they can interact in the first bars of the calorimeter, causing a larger percentage of shower containment (i.e. $\sim 48\%$ at 75 GeV, as shown in Fig. 4.3).

4.1.3 Unfolding procedure

Given that the hadronic shower is not fully contained in the calorimeter, a method has to be used in order to infer the real p+He spectrum starting from the observed one, while taking into account the bin-to-bin migration of the events. Specifically, an unfolding procedure based on the Bayes' theorem [83], previously also adopted in other experiments such as Fermi-LAT [84–86], is applied. The detector response is predicted using MC simulations of p+He after applying all the selection cuts described in the previous chapter. The number of selected p+He events in the BGO energy bin i, $N(E_O^i)$, caused by a certain number of p+He events in the jth bin of primary energy $N(E_T^j)$, observed with a probability $P\left(E_O^i|E_T^j\right)$, is:

$$N(E_O^i) = \sum_{j=1}^{n} P\left(E_O^i|E_T^j\right) N(E_T^j). \tag{4.2}$$

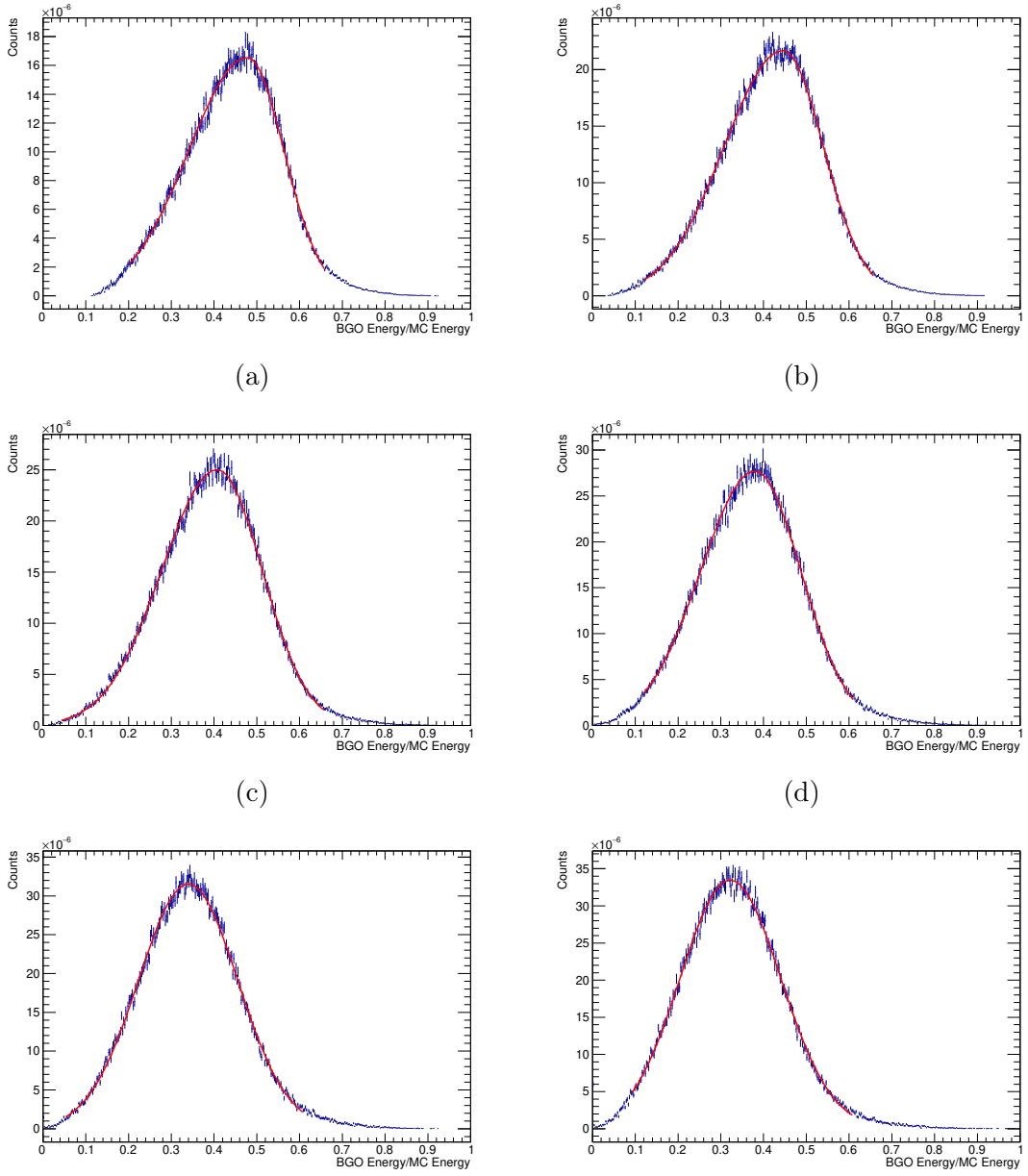

Figure 4.2: Ratio between energy deposited in the BGO (BGO Energy) and primary energy (MC Energy) for p+He MC selected events in various bins of primary energy: (a) 100.0 GeV - 177.8 GeV, (b) 316.2 GeV - 562.3 GeV, (c) 1.0 TeV - 1.8 TeV, (d) 3.2 TeV - 5.6 TeV, (e) 17.8 TeV - 31.6 TeV, (f) 56.2 TeV - 100.0 TeV. The distributions are fit with an asymmetric Gaussian function, shown with a red line.

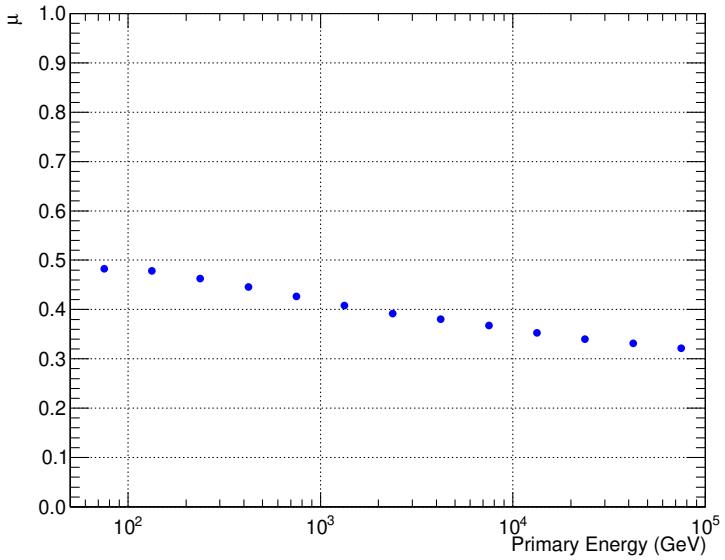

Figure 4.3: Mean value of the ratio between BGO energy and primary energy extracted from the asymmetric Gaussian fit with respect to the primary energy of the particles. Error bars are smaller than the marker size.

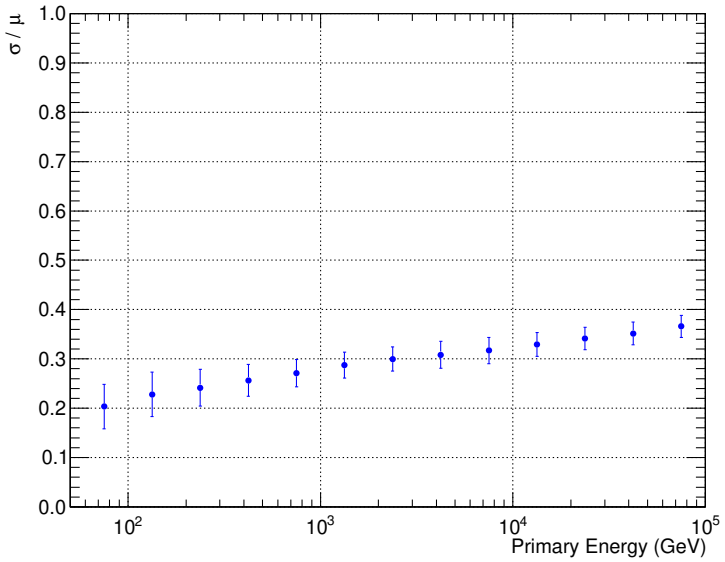

Figure 4.4: Sigma over mean of the ratio between BGO energy and primary energy extracted from the asymmetric Gaussian fit, with respect to the primary energy of the particles.

The number $N(E_O^i)$ of observed events, is shown in Fig. 4.5. The probability $P\left(E_O^i|E_T^j\right)$ (called *smearing matrix*) is obtained from p+He MC simulations, after applying all the selection cuts and re-weighting the events according to a power-law of the energy $\mathrm{E}^{-2.6}$. In order to obtain the real number of events $N(E_T^j)$, the smearing matrix is inverted iteratively using the Bayes' theorem to retrieve the so-called *response matrix*, which is shown in Fig. 4.6 and can be expressed as follows:

$$P\left(E_T^i|E_O^j\right) = \frac{P\left(E_O^i|E_T^j\right) P\left(E_T^j\right)}{\sum_{k=1}^{n} P\left(E_O^i|E_T^k\right) P\left(E_T^k\right)}. \tag{4.3}$$

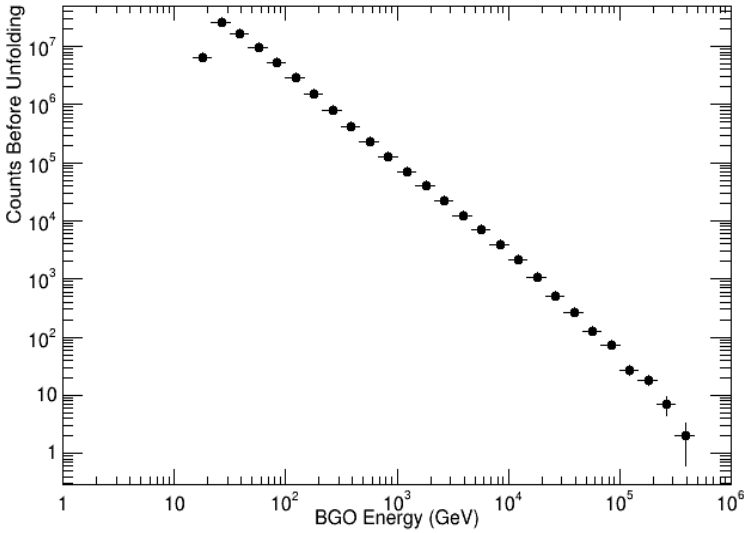

Figure 4.5: Distribution of energy deposit in the BGO for selected p+He flight events before the unfolding procedure.

The color scale on the z-axis of the matrix represents the conditional probability that the p+He candidates with incident energy E_T^i, are observed with an energy E_O^j deposited in the calorimeter. Finally, the number of p+He events in bins of primary energy is obtained using the formula:

$$N(E_T^i) = \sum_{j=1}^{n} P\left(E_T^i|E_O^j\right) N(E_O^j). \tag{4.4}$$

The reconstructed energy distribution after the unfolding procedure is shown in Fig. 4.7.

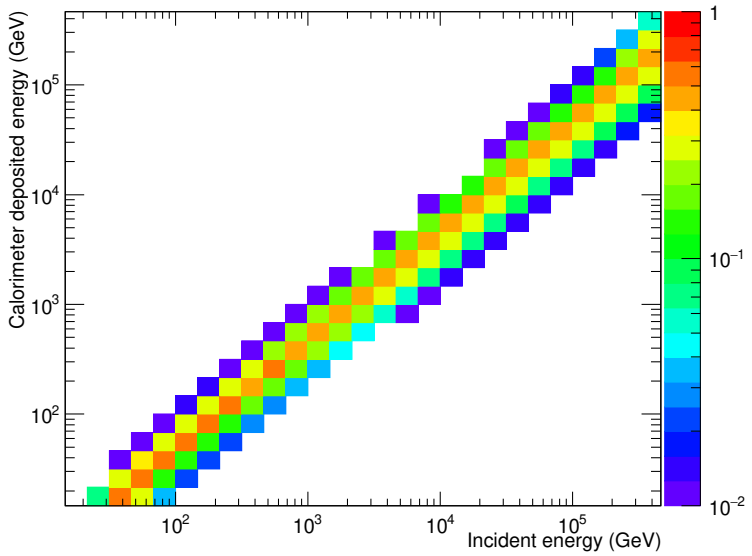

Figure 4.6: Response matrix derived from MC simulations of p and He after applying the selection cuts. The colors represent the probability that the event in a bin of incident energy, migrates to different bins of energy deposited in the BGO calorimeter.

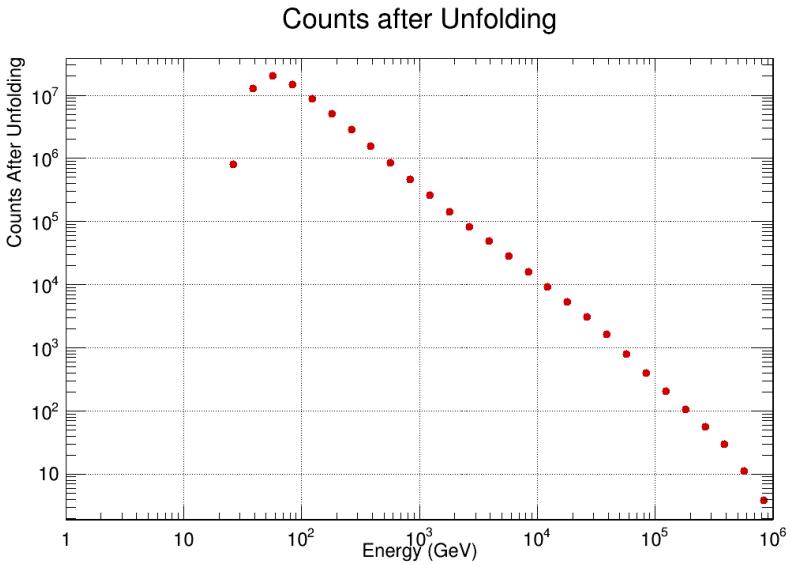

Figure 4.7: Reconstructed energy distribution for selected p+He flight events after the unfolding procedure. Error bars are smaller than the marker size.

4.2 Statistical uncertainties

The statistical uncertainties in the flux are related to the fluctuations in the number of detected events following a Poisson distribution. The statistical uncertainties estimation could be affected by the bin-to-bin migration, due to the unfolding procedure used to obtain the primary particle energy. To overcome this problem, a toy-MC method, consisting of the following steps, has been used:

- 10000 p+He counts distributions are generated in various energy bins following a Poisson probability with the mean value given by the real number of events in each energy bin;
- the generated distributions are unfolded using the same procedure that is used for the spectrum;
- after the unfolding, the number of events in each bin follows a Gaussian distribution as shown in Fig. 4.8, for some of them;
- the resulting distributions are fit with a Gaussian function, from which mean value (μ) and standard deviation (σ) are extracted;
- the $\frac{\sigma}{\mu}$ values, shown in Fig. 4.9 give an estimation of the fractional statistical uncertainty.

In Fig. 4.10 statistical uncertainties resulting from the unfolding procedure and from the toy-MC method are compared, showing the underestimation of uncertainties from the unfolding alone, especially at the highest energies. The statistical uncertainties obtained with the toy-MC procedure will be used for the proton+helium spectrum.

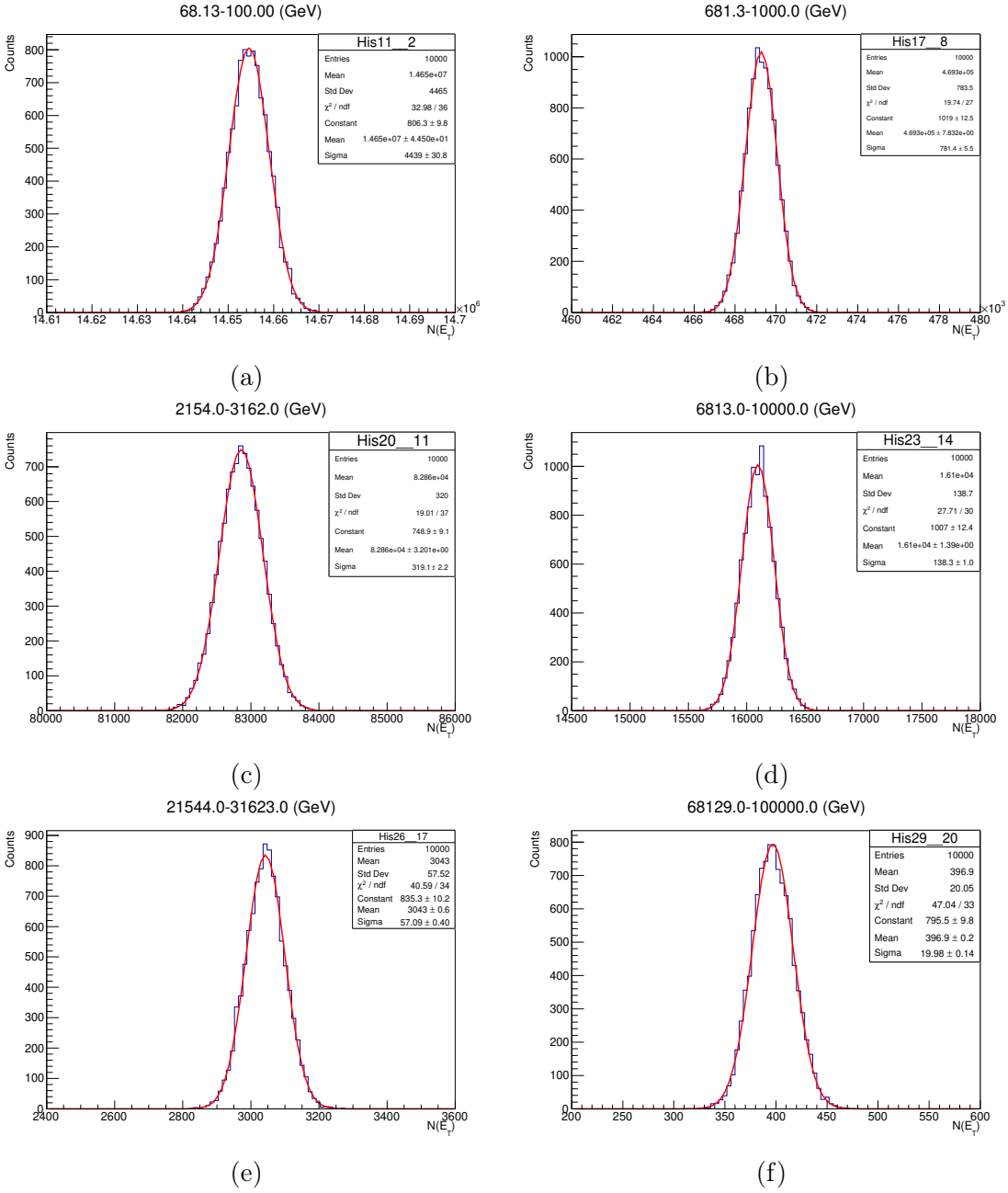

Figure 4.8: Generated counts distributions after the unfolding, in various bins of primary energy. The Gaussian fit function is shown in red and the parameters resulting from the fit are reported in the panel.

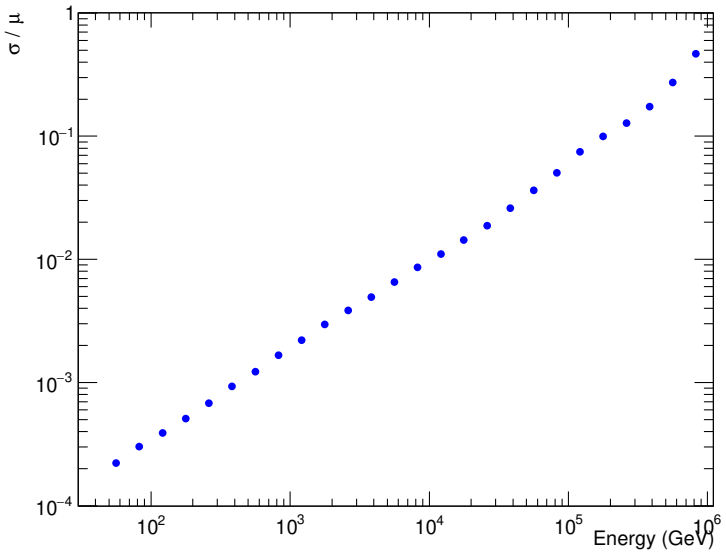

Figure 4.9: Fractional statistical errors obtained with the Toy-MC method. The σ and μ values are the standard deviation and the mean value obtained with the fits shown in Fig. 4.8.

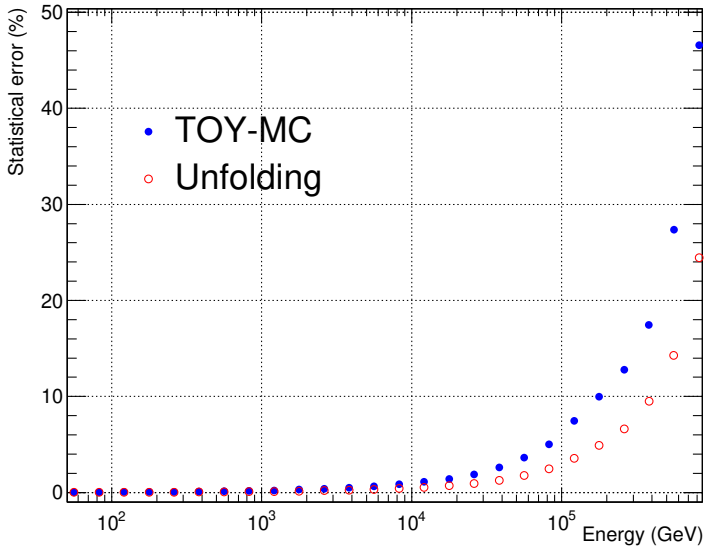

Figure 4.10: Comparison between statistical errors obtained (red empty circles) directly from the unfolding and (blue filled circles) with the toy-MC method. In this case, the linear scale is used on the Y-axis, to better appreciate the difference between the two approaches at high energy.

4.3 Flux calculation

The flux for each energy bin (Φ_i) can be written as follows:

$$\Phi_i = \frac{\Delta N_i}{\Delta T \times A_i \times \Delta E_i} \tag{4.5}$$

with ΔN_i number of events in the i-th energy bin after the unfolding (see Fig. 4.7), ΔT total live time (see section 3.1.1), A_i acceptance in the i-th bin (see Fig. 3.18), and ΔE_i width of the i-th energy interval. The p+He flux is shown in Fig. 4.11 in the energy range 46 GeV - 316 TeV, multiplied by $E^{2.7}$. Error bars represent the 1σ statistical uncertainties obtained using the toy-MC procedure described in the previous section.

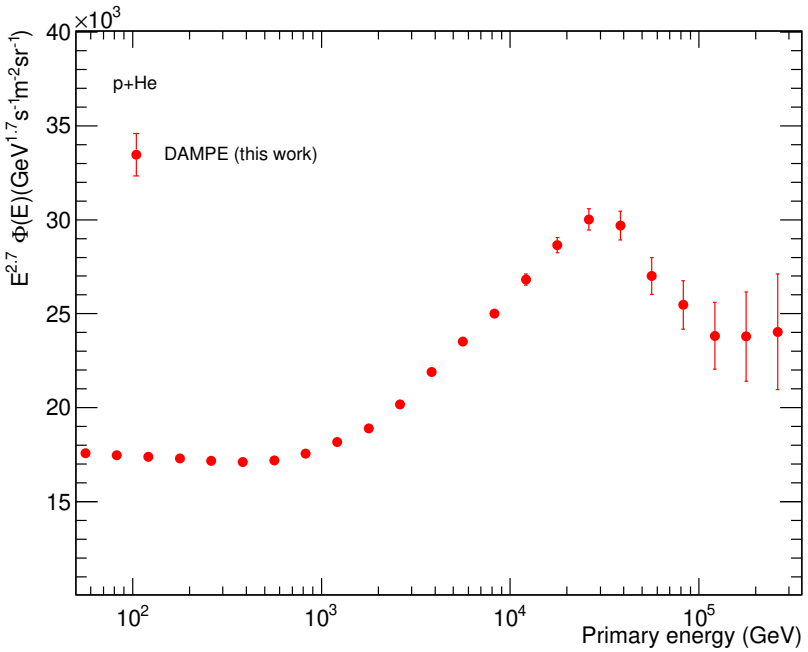

Figure 4.11: The p+He energy spectrum obtained with this analysis in the energy range 46 GeV - 316 TeV, multiplied by $E^{2.7}$ and with error bars representing the statistical uncertainties only.

4.4 Systematic uncertainties

The applied selection cuts and the choices or assumptions made during the analysis procedure can result in systematic uncertainties in the p+He flux measurement. They will be described and evaluated in this section.

4.4.1 Efficiency validations

As shown in equation 3.5, fundamental ingredients for the calculation of the effective acceptance are the selection cut efficiencies (i.e. high energy trigger, track reconstruction, charge selection). An eventual difference in efficiency between MC and flight data can be a source of systematic uncertainty on the final spectrum. For this reason, the efficiency evaluation and the MC/data difference will be described in this section, finally quantifying their contribution to the systematic uncertainties on the p+He flux.

High Energy Trigger efficiency

The activation of the High Energy Trigger (HET) is required in this analysis (see section 3.2.1). Apart from the HET, there are other three implemented triggers in DAMPE and among these, the Unbiased Trigger (UNBT) has minimum requirements (the DAMPE trigger logic is described in section 2.7), therefore the HET efficiency can be estimated using the following formula:

$$\epsilon_{HET} = \frac{N_{HET|UNBT}}{N_{UNBT}}, \tag{4.6}$$

where $N_{HET|UNBT}$ is the number of events satisfying both HET and UNBT trigger criteria. The HET efficiency for the p+He analysis is presented in Fig. 4.12, showing the comparison between MC and flight data. The difference between the two is shown in the bottom panel of Fig. 4.12, and the value of $\sim 4\%$ is taken as systematic uncertainty on the HET efficiency. As explained in section 2.7, different triggers have different pre-scaling factors and in particular, the UNBT trigger has a pre-scale factor of 1/512 (1/2048) when the satellite operates in (out of) the geographical latitude range [-20°; 20°]. For this reason, the flight data error bars in Fig. 4.12 become large when going to high energy, where fluxes are much lower.

Charge selection efficiency

In order to evaluate the charge selection efficiency, instead of taking the PSD global energy deposit given by the averaged signal recorded by the 2 PSD layers, the charge measurement is performed using the PSD layers X and Y separately. The smearing correction is also applied on the MC PSD signal differentiating layers X and

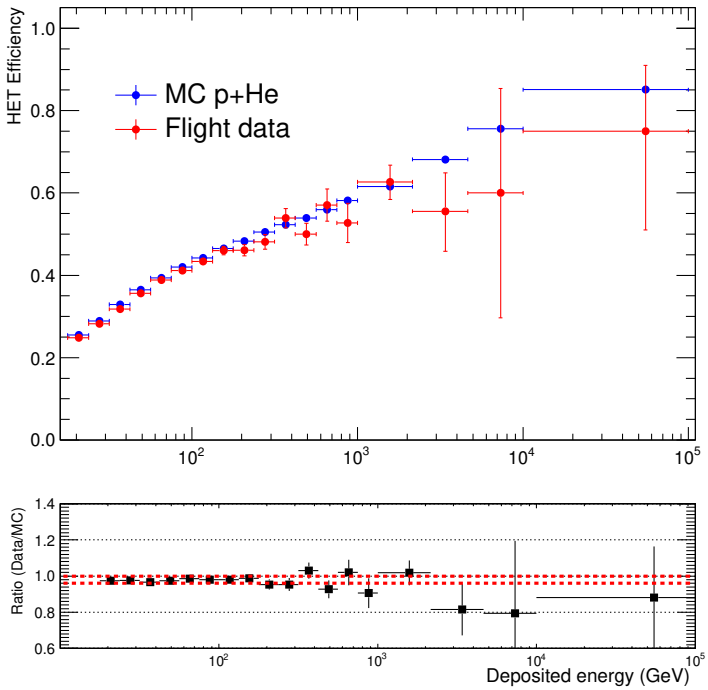

Figure 4.12: HET efficiency considering MC (in blue) and flight data (in red) of p+He. In the bottom panel, the ratio between MC and flight data is shown.

Y. In appendix C a sub-sample of the plots produced to perform the charge selection on layers X and Y, for flight data and MC, are reported. As said before, the STK can also be used for charge selection roughly up to Z=8, but with lower resolution with respect to the PSD (see section 2.4). Therefore, in addition to the signal read by the PSD, the information given by the STK can also be used to evaluate the charge selection efficiency. This is done by (i) requiring a signal in the first STK plane (on both X and Y layers), (ii) taking the combined STK signal defined as: $(STK_X+STK_Y)/2$, (iii) looking at the proton and helium peaks in the STK and (iv) selecting a range in ADC counts in which we expect to find proton and helium. The STK signal was divided in bins of BGO energy showing that a constant cut of STK signal lower than 400 ADC is adequate to select a p+He sample (see figures in appendix C). The efficiency for the two PSD layers can finally be computed as follows:

$$\epsilon_{PSD_1} = \frac{N_{PSD_1|PSD_2|STK_1}}{N_{PSD_2|STK_1}}, \tag{4.7}$$

$$\epsilon_{PSD_2} = \frac{N_{PSD_1|PSD_2|STK_1}}{N_{PSD_1|STK_1}}. \tag{4.8}$$

In eq. 4.7 and 4.8, ϵ_{PSD_1} (ϵ_{PSD_2}) represents the charge selection efficiency for the first (second) PSD layer, $N_{PSD_1|PSD_2|STK_1}$ is the number of p+He events selected using the information from both PSD layers and the STK plane, and $N_{PSD_2|STK_1}$ ($N_{PSD_1|STK_1}$) are the events selected using only the second (first) PSD layer and the STK signal. The charge selection efficiencies for both PSD layers are shown in Fig. 4.13 and 4.14. The results from flight data are compared with MC data showing a negligible difference up to $\sim$ 100 GeV, which becomes $\sim$ 1% for higher energy, and reaches $\sim$ 3% for energy larger than 1 TeV only for the first layer.

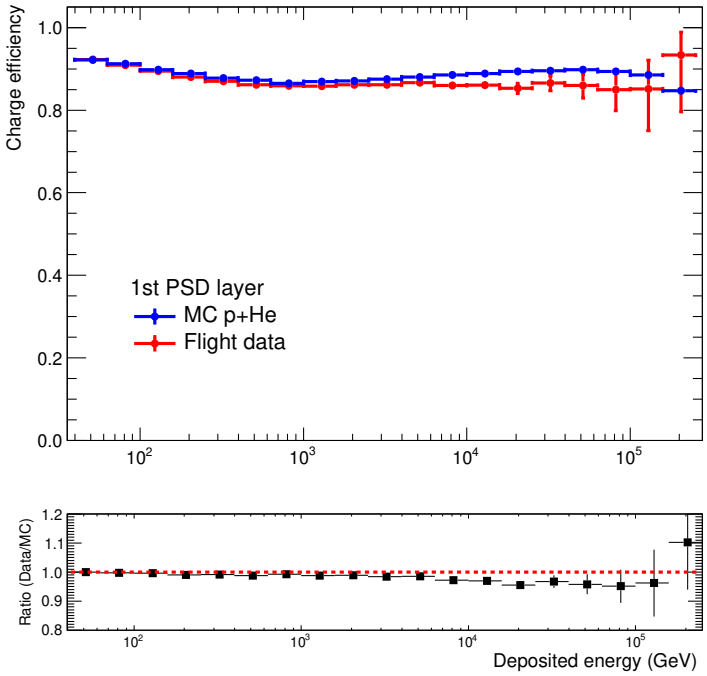

Figure 4.13: In the top panel the efficiency for the first layer of the PSD, for MC (in blue) and flight data (in red) of p+He. In the bottom panel, the ratio between MC and flight data is presented.

Track reconstruction efficiency

The event selection procedure includes the track reconstruction. It follows that also the difference in track selection efficiency for MC and flight data can be a source of systematic uncertainties. To estimate such efficiency, the p+He selection procedure is repeated from the beginning exploiting the BGO track selection capabilities and removing completely the STK contribution. The STK track efficiency

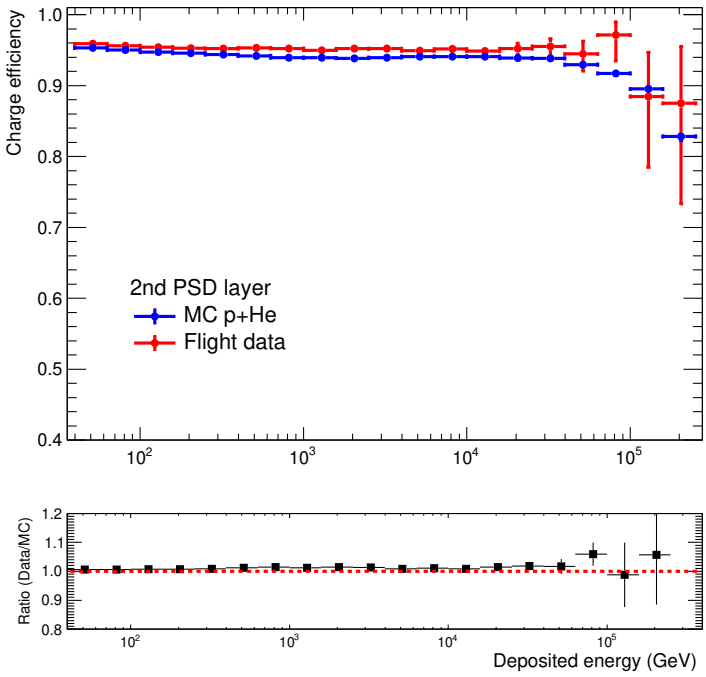

Figure 4.14: In the top panel the efficiency for the second layer of the PSD, for MC (in blue) and flight data (in red) of p+He. In the bottom panel, the ratio between MC and flight data is presented.

can therefore be expressed as:

$$\epsilon_{track} = \frac{N_{STK|BGO|PSD}}{N_{BGO|PSD}}, \tag{4.9}$$

where $N_{BGO|PSD}$ is the number of events selected with the BGO track and PSD charge, and $N_{STK|BGO|PSD}$ is the number of events passing the STK track selection (as done in the standard analysis procedure). The STK track efficiency for MC and flight data is shown in Fig. 4.15, with the bottom panel representing their ratio. The difference is found to be $\sim 2\%$ and it's added in quadrature to the previously discussed systematic uncertainties.

4.4.2 Hadronic interaction model

The total systematic uncertainties are dominated by the hadronic interaction model (also called *physics list*) chosen for the MC simulations. For this work, the GEANT4-FTFP_BERT[1] interaction model is used because it is in better agree-

[1] `https://geant4-userdoc.web.cern.ch/UsersGuides/PhysicsListGuide/html/reference_PL/FTFP_BERT.html`

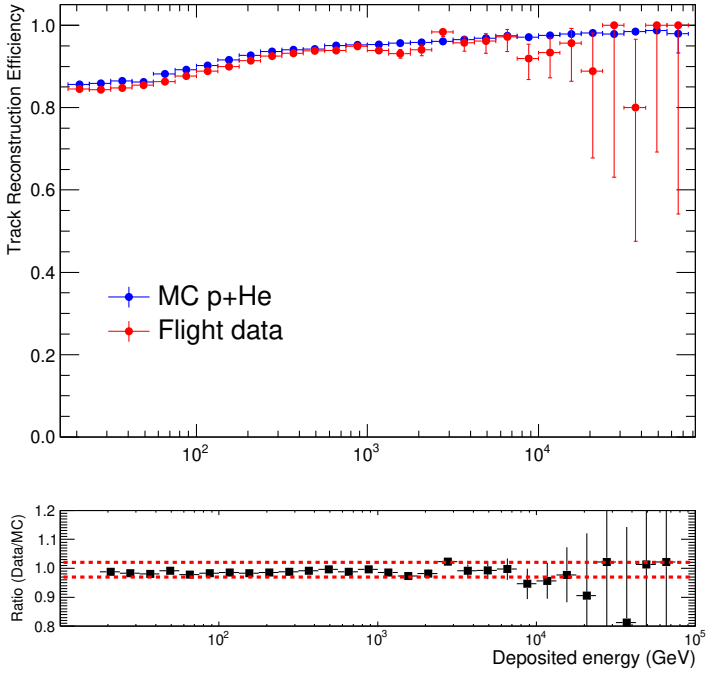

Figure 4.15: Track selection efficiency considering MC (in blue) and flight data (in red) of p+He. In the bottom panel, the ratio between MC and flight data is shown.

ment with flight and test beam data [51, 60, 87] with respect to other models. The systematic uncertainty introduced by this choice can be evaluated by computing the spectrum using different models and comparing the results. As reported in section 3.1.2, additional MC samples were produced using the FLUKA DPMJET-3 [73–76] physics list for helium and the GEANT4-QGSP_BERT[2] for protons. The spectra obtained with different hadronic models are shown in Fig. 4.16 along with their ratio (in the bottom panel). Their difference reaches a maximum value of ∼15% at 100 TeV. This is also the limit of the simulated MC proton QGSP_BERT sample and for this reason, the difference could be overestimated. Nonetheless, as a safe choice, the systematic uncertainty on the hadronic model is set at ∼15% from 100 TeV onwards.

4.4.3 Spectral weight

The p and helium MC events are produced with a power-law spectrum with an energy dependence E^{-1}. The MC samples are then re-weighted according to an $E^{-2.6}$

[2] https://geant4-userdoc.web.cern.ch/UsersGuides/PhysicsListGuide/html/reference_PL/QGSP_BERT.html

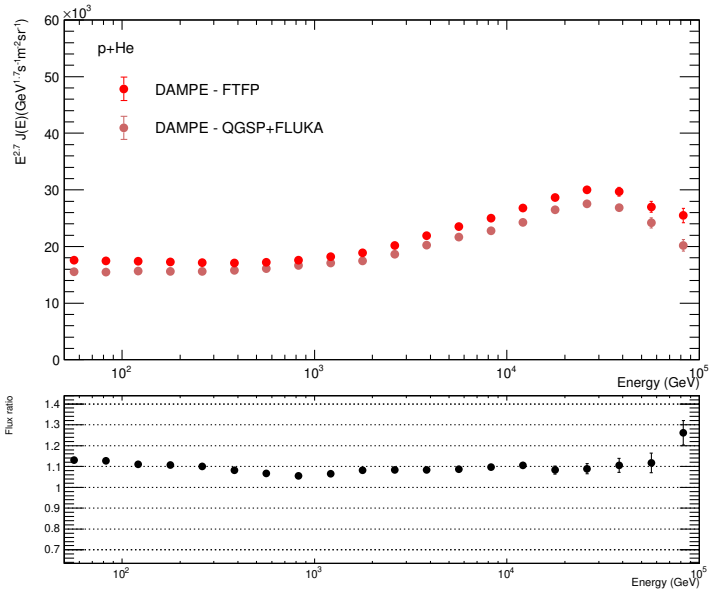

Figure 4.16: Comparison between the p+He spectra computed using different hadronic interaction models for the MC simulations. The spectra are shown in the top panel and their ratio is reported in the bottom panel.

power law, following both theoretical expectations and experimental observations (see sections 1.2 and 1.4). The effect of applying different weights such as $E^{-2.5}$ and $E^{-2.7}$ was investigated resulting in a negligible difference in the final p+He spectrum. For this reason, the spectral weight was not included in the systematic uncertainties.

4.4.4 MC proton and helium mixture

In the energy range of interest for this work (from tens of GeV to hundreds of TeV), the CR proton and helium abundances are of the same order of magnitude. Nonetheless, recent results from DAMPE on the proton and helium spectra [3, 9] show that protons are more abundant than helium up to $\sim$ tens of TeV, and helium nuclei start becoming predominant at higher energy. The flux resulting from the analysis presented in this thesis was obtained by assuming the same amount of proton and helium in the MC simulations (50% proton and 50% helium). The systematic error related to this choice is evaluated by computing the p+He spectrum anew assuming an energy-dependent proton and helium abundance obtained by fitting the DAMPE proton and helium spectra [3, 9]. The resulting fluxes and their ratio are shown in Fig. 4.17, with a difference of $\sim$ 5% at low energy and $\sim$ 2% for energies higher than 10 TeV. These percentages are taken as further systematic uncertainty to the final flux.

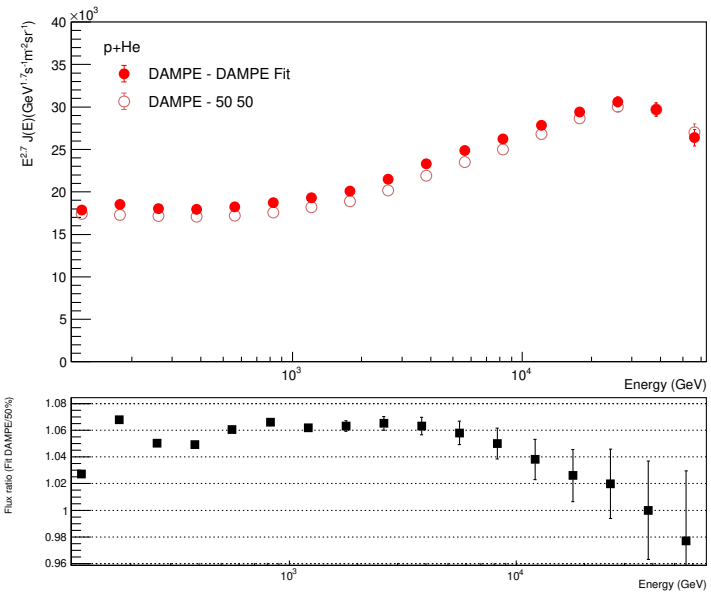

Figure 4.17: In the top panel the p+He spectrum computed assuming in the unfolding procedure (open circles) the same proton and helium abundance and (filled circles) an energy-dependent abundance extracted from the fits to the DAMPE proton and helium spectra [3, 9]. In the bottom panel the ratio between the two spectra. See text for more details.

4.4.5 BGO saturation correction

In section 4.1.1 the corrections to the energy deposited in the calorimeter were introduced. In particular, the correction for the saturation of the signal in the BGO was found to be more important for helium nuclei (see Appendix B and [54]) and for this reason, the parameters used to account for the saturation, in this analysis, are the ones extrapolated when considering helium. Since protons are included in this analysis as well, the spectrum was computed again by applying the proton correction parameters. The difference between the two spectra is shown in Fig. 4.18 and is included in the systematic uncertainties.

4.5 Results: the p+He energy spectrum

The statistical and systematic uncertainties discussed in the previous sections are shown in Fig. 4.19. The different contributions to the systematic uncertainty are shown both individually with different colors and summed together (in quadrature) with a dark grey line. From Fig. 4.19, it's evident that the main source of uncertainty in the spectrum comes from the comparison between different hadronic interaction

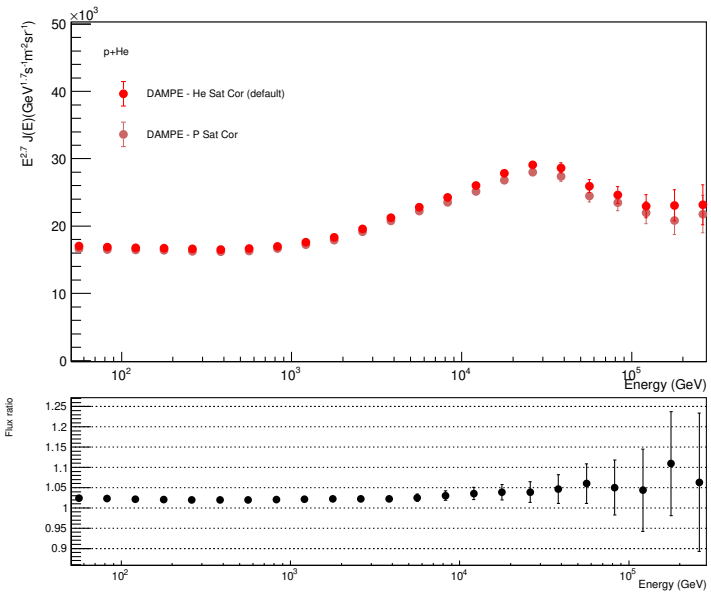

Figure 4.18: In the top panel the spectrum computed correcting the saturation of the signal in the BGO using the helium parameters is compared with the one computed using the proton parameters. In the bottom panel their ratio is presented.

models.

In Fig. 4.20 the p+He flux is presented in the energy range from 46 GeV to 316 TeV, multiplied by $E^{2.7}$ for better visualization of the spectral features. Error bars represent the 1σ statistical error while the continuous bands represent the systematic uncertainties on the analysis procedure (inner band) and the total systematic uncertainties, including also the uncertainty on the hadronic interaction model (outer band).

The results from this work are shown in Table 4.1. E, E_{low} and E_{high} are the median energy and bin edges of the corresponding p+He flux Φ. The uncertainties are indicated with σ_{stat} (statistical uncertainty), σ_{sys}^{ana} and σ_{sys}^{had} (systematic uncertainties on the analysis procedure and on the hadronic interaction model, respectively).

4.6 Fit of the spectrum and comparison with DAMPE results on proton and helium alone

The proton+helium spectrum exhibits a clear spectral hardening around 600 GeV consistent with results obtained by other experiments [2, 4–6, 10–17, 40] and previous DAMPE results on the proton [3] and helium [9] spectra. Additionally, the p+He

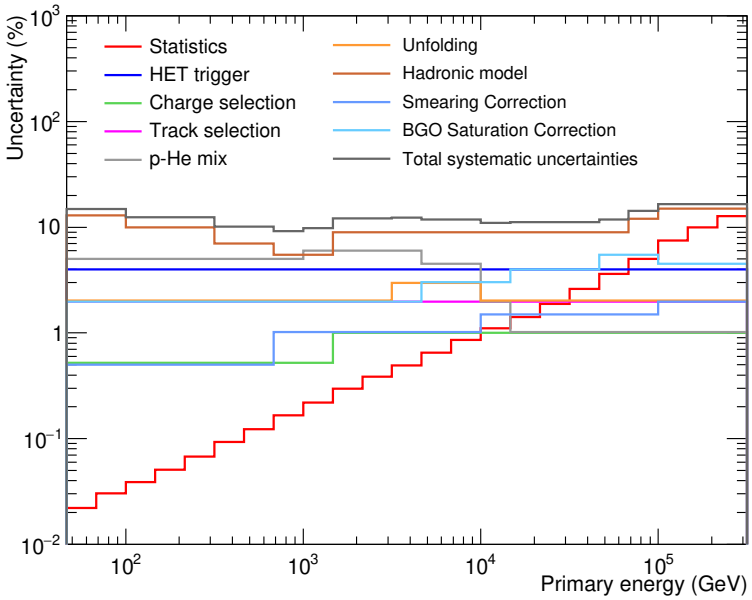

Figure 4.19: Statistical and systematic uncertainties for the p+He spectrum.

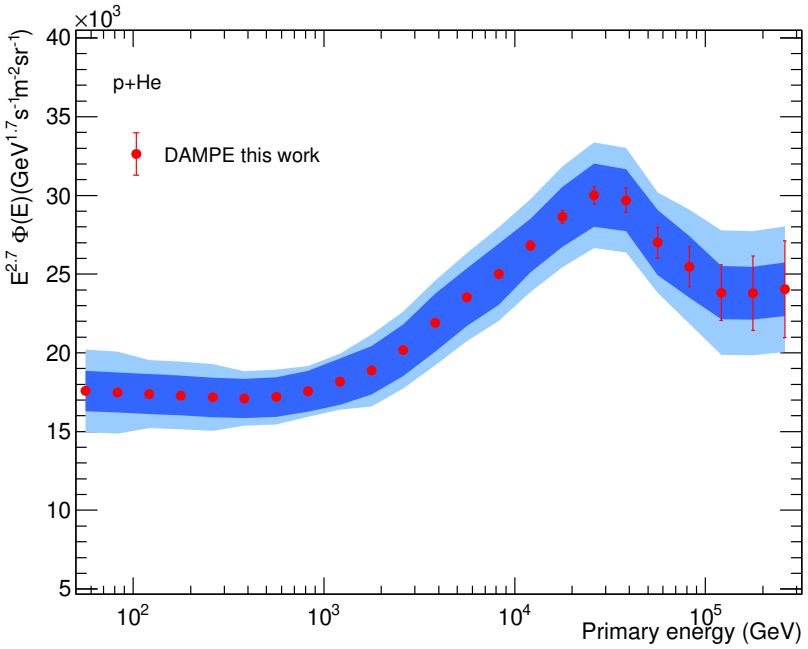

Figure 4.20: The p+He energy spectrum measured with this work, between 46 GeV and 316 TeV. Statistical uncertainties (1σ) are represented by error bars, while the continuous bands represent the systematic uncertainties on the analysis (inner band) and the total systematic uncertainties, including the one on the hadronic model (outer band).

Table 4.1: The p+He flux along with the 1σ statistical error and the systematic uncertainties coming from the analysis and hadronic interaction models respectively. E, E_{low} and E_{high} are the median energy and bin edges of the corresponding flux Φ.

E [GeV]	E_{low} [GeV]	E_{high} [GeV]	$\Phi \pm \sigma_{stat} \pm \sigma_{sys}^{ana} \pm \sigma_{sys}^{had}$ [$GeV^{-1}m^{-2}s^{-1}sr^{-1}$]
56.23	46.42	68.13	$(3.31 \pm 0.00073 \pm 0.24 \pm 0.49) \times 10^{-01}$
82.54	68.13	100.00	$(1.17 \pm 0.00035 \pm 0.08 \pm 0.17) \times 10^{-01}$
121.15	100.00	146.78	$(4.12 \pm 0.0016 \pm 0.30 \pm 0.51) \times 10^{-02}$
177.83	146.78	215.44	$(1.45 \pm 0.0074 \pm 0.11 \pm 0.18) \times 10^{-02}$
261.02	215.44	316.23	$(5.13 \pm 0.035 \pm 0.37 \pm 0.63) \times 10^{-03}$
383.12	316.23	464.16	$(1.81 \pm 0.017 \pm 0.13 \pm 0.18) \times 10^{-03}$
562.34	464.16	681.29	$(6.46 \pm 0.079 \pm 0.47 \pm 0.65) \times 10^{-04}$
825.40	681.29	1000.00	$(2.34 \pm 0.039 \pm 0.17 \pm 0.22) \times 10^{-04}$
1211.53	1000.00	1467.80	$(8.60 \pm 0.19 \pm 0.69 \pm 0.84) \times 10^{-05}$
1778.28	1467.80	2154.44	$(3.17 \pm 0.094 \pm 0.26 \pm 0.38) \times 10^{-05}$
2610.16	2154.44	3162.28	$(1.20 \pm 0.046 \pm 0.10 \pm 0.15) \times 10^{-05}$
3831.19	3162.28	4641.59	$(4.63 \pm 0.23 \pm 0.39 \pm 0.57) \times 10^{-06}$
5623.40	4641.60	6812.90	$(1.76 \pm 0.12 \pm 0.14 \pm 0.21) \times 10^{-06}$
8254.00	6812.90	10000.00	$(6.65 \pm 0.57 \pm 0.52 \pm 0.79) \times 10^{-07}$
12115.30	10000.00	14678.00	$(2.53 \pm 0.28 \pm 0.16 \pm 0.28) \times 10^{-07}$
17782.80	14678.00	21544.30	$(0.96 \pm 0.14 \pm 0.06 \pm 0.11) \times 10^{-07}$
26101.60	21544.30	31622.80	$(3.57 \pm 0.67 \pm 0.24 \pm 0.40) \times 10^{-08}$
38311.90	31622.80	46415.90	$(1.25 \pm 0.33 \pm 0.08 \pm 0.14) \times 10^{-08}$
56234.00	46416.00	68129.00	$(4.04 \pm 0.15 \pm 0.31 \pm 0.48) \times 10^{-09}$
82540.00	68129.00	100000.00	$(1.35 \pm 0.068 \pm 0.10 \pm 0.19) \times 10^{-09}$
121153.0	100000.0	146780.0	$(4.49 \pm 0.33 \pm 0.32 \pm 0.74) \times 10^{-10}$
177828.0	146780.0	215444.0	$(1.59 \pm 0.16 \pm 0.11 \pm 0.26) \times 10^{-10}$
261016.0	215444.0	316228.0	$(5.70 \pm 0.73 \pm 0.40 \pm 0.95) \times 10^{-11}$

spectrum shows a softening feature in the energy region around 25 TeV which was detected for the first time by DAMPE in both proton and helium spectra ([3], [9]). The evidence of the softening in the p+He analysis is a robust cross-check on this feature for the proton or helium alone analyses. Indeed, the proton spectrum is affected by the background coming from helium nuclei and vice versa, while the combination of the two nuclei eliminates this source of uncertainty and assures the significance of the softening feature. It follows that the flux, $\Phi(E)$, deviates from a single power law model and can be well described by a smoothly broken power law

(SBPL) function, such as:

$$\Phi(E) = \Phi_0 \left(\frac{E}{\text{TeV}}\right)^{-\gamma} \left[1 + \left(\frac{E}{E_B}\right)^{s}\right]^{\Delta\gamma/s}, \tag{4.10}$$

where Φ_0 is the flux normalization, γ the spectral index before the break energy (E_B), $\Delta\gamma$ the difference between the spectral index before and after the break and s the smoothness of the break. Moreover, to take into account the systematic uncertainties, the χ^2 function is defined as follows:

$$\chi^2 = \sum_{i=a}^{b} \left[\frac{\Phi\left(E_i\right) S\left(E_i, w\right) - \Phi_i}{\sigma_{stat,i}}\right]^2 + \sum_{j=1}^{m} \left(\frac{1 - w_j}{\tilde{\sigma}_{sys,j}}\right)^2, \tag{4.11}$$

where Φ_i is the measured p+He flux, $\Phi(E_i)$ the SBPL model predicted flux in each corresponding energy bin, $S(E_i, w)$ is a piece-wise function defined by its value w_j in a specific energy range covered by the j-th nuisance parameter (w), $\sigma_{stat,i}$ the statistical uncertainty of the measurement in the i-th energy bin, and $\sigma_{sys,j}$ is the relative systematic uncertainty of the data in such an energy range, defined as $\sigma_{sys,j} = \left(\sqrt{(\sigma_{sys}^{ana})^2 + (\sigma_{sys}^{had})^2}\right)/\Phi$. An analogous procedure was adopted in [66], [3], [9] and [65]. To investigate the softening feature, the p+He flux is fit in the energy range from 7 TeV to 130 TeV, using the formulae 4.10 and 4.11, with 2 nuisance parameters w (assigned to the energy ranges before and after the predicted softening, respectively) and fixing the smoothness (s) to 10, for consistency with the DAMPE proton and helium fit of the softening [3, 9]. The fit is shown in Fig. 4.21 and the results are reported in Table 4.2.

Table 4.2: Results of the SBPL fit in the softening energy region for the p+He spectrum (this work).

Φ_0 ($\text{GeV}^{-1}\text{m}^{-2}\text{s}^{-1}\text{sr}^{-1}$)	$(1.36 \pm 0.09) \times 10^{-4}$
E_b (TeV)	26.4 ± 3.6
γ	2.52 ± 0.02
$\Delta\gamma$	0.38 ± 0.06
s	10 (fixed)
χ^2/dof	0.25/2

The significance of the softening is estimated by fitting the same energy region (from 7 TeV to 130 TeV) with a single power law function. The latter gives the result of $\chi^2/\text{dof} = 48.14/4$, which translates to a significance of 6.69σ in favor of the SBPL

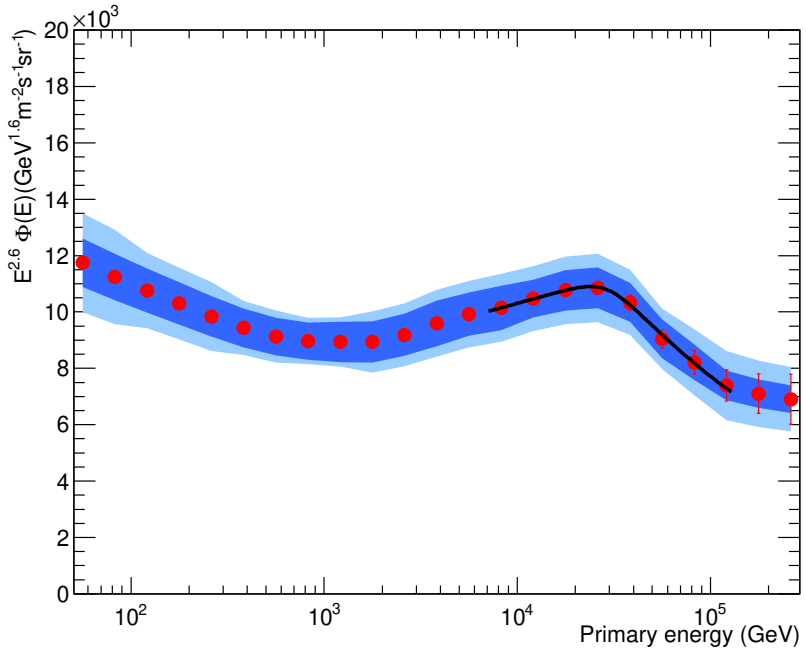

Figure 4.21: Fit of the p+He spectrum (in red) with a SBPL function (in black). Statistical uncertainties are represented by error bars. In shaded bands the systematic uncertainties on the analysis (inner band) and total, including the contribution from the hadronic model (outer band).

model, the highest significance of the softening measured so far. In the highest energy part, the p+He spectrum shows a possible additional hardening around 150 TeV, also suggested by the HAWC collaboration [88]. In this work, the significance of this third feature is still too low but it could eventually be confirmed in the future by collecting more statistics and adopting novel analysis techniques.

Furthermore, this work can be compared with the previously published DAMPE proton and helium results [3, 9]. In Fig. 4.22 the three DAMPE spectra are plotted together and compared showing good internal consistency considering also that the three works were performed by different working groups, using independent analysis methods. The parameters estimated with the SBPL fit of the softening in the three analyses are compared in Table 4.3. The values obtained for E_b suggest a rigidity-dependent softening feature, even though a mass dependence will eventually be ruled out only by collecting additional statistics and improving the analysis towards reducing the systematic uncertainties, or from the analysis of heavier nuclei spectra.

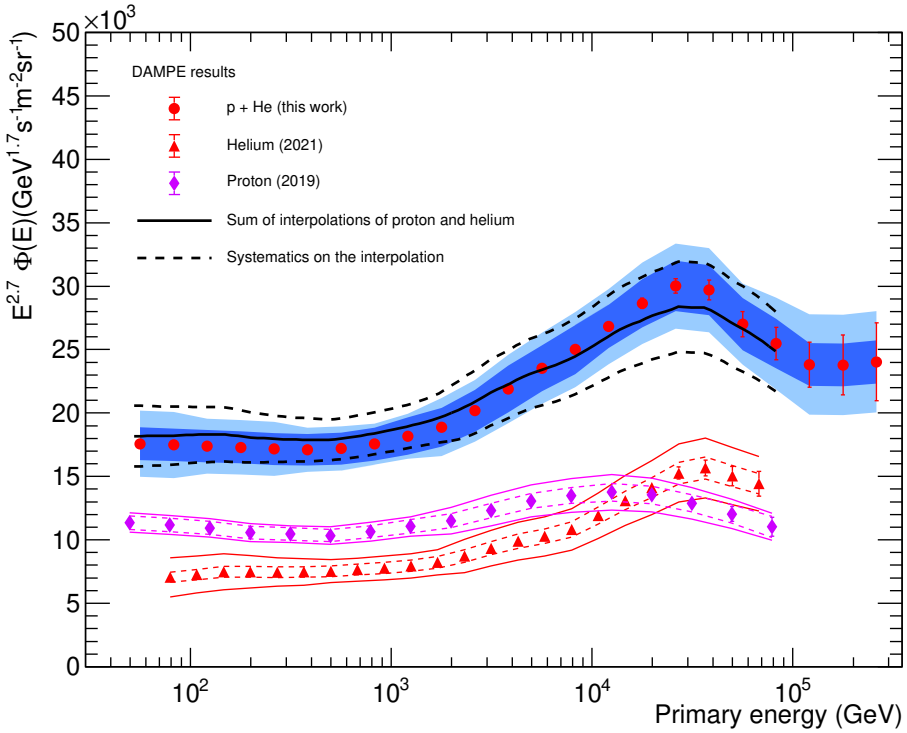

Figure 4.22: Comparison between (red circles) p+He spectrum, (red triangles) DAMPE helium spectrum [9] and (magenta diamonds) DAMPE proton spectrum [3]. The systematic uncertainties are shown with blue and light-blue bands for the p+He spectrum, while they are indicated with dashed and continuous lines for the proton and helium spectra. The outer band (or continuous lines) represents the total systematic uncertainties while the inner band (dashed lines) doesn't include the uncertainty on the hadronic model. Error bars correspond to the 1σ statistical uncertainties.

Table 4.3: Results of the SBPL fit in the softening energy region for the DAMPE proton [3], helium [9] and p+He spectra (this work). For the helium results, the systematic uncertainties from the hadronic model are represented by the second error.

	Proton	Helium	Proton+Helium
E_b (TeV)	$13.6^{+4.1}_{-4.8}$	$34.4^{+6.7+11.6}_{-9.8-0.0}$	26.4 ± 3.6
γ	2.60 ± 0.01	$2.41^{+0.02+0.02}_{-0.02-0.00}$	2.52 ± 0.02
$\Delta\gamma$	-0.25 ± 0.07	$-0.51^{+0.18+0.01}_{-0.20-0.00}$	-0.38 ± 0.06

4.7 Comparison with other experimental results

The last part of this chapter concerns the comparison between this work and the p+He results obtained by other experiments. The DAMPE p+He flux is presented in Fig. 4.23 multiplied by $E^{2.7}$ with other direct measurements and in Fig. 4.24 multiplied by $E^{2.6}$, compared with indirect p+He measurements.

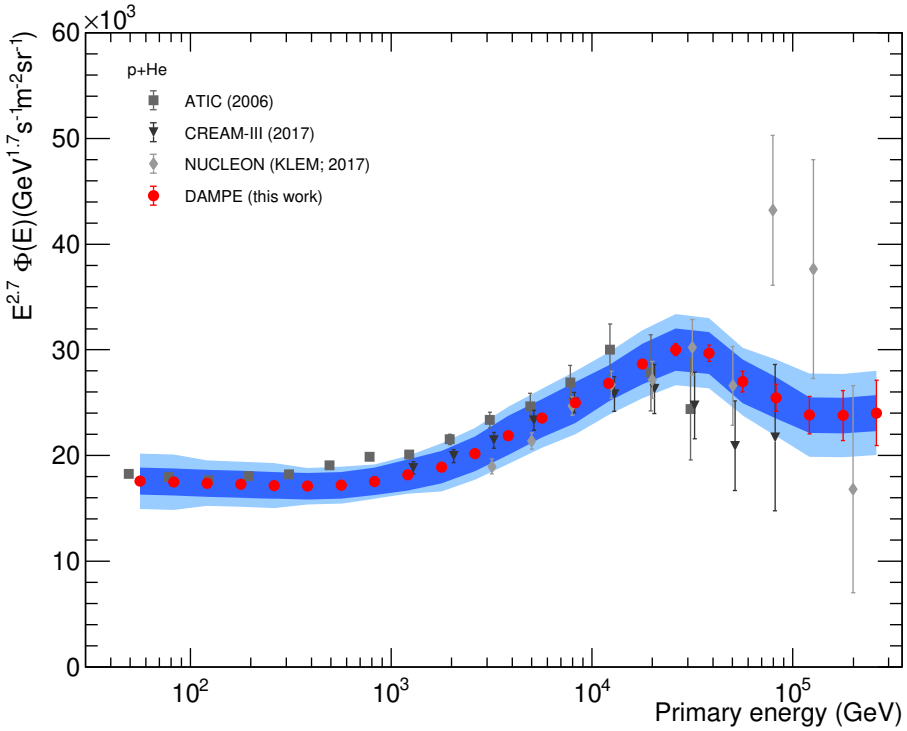

Figure 4.23: The p+He energy spectrum measured with this work, between 46 GeV and 316 TeV, compared with direct measurements of p+He made by ATIC-02 [7], NUCLEON [6] and CREAM [10]. Statistical uncertainties (1σ) are represented by error bars, while the continuous bands represent the systematic uncertainties on the analysis (inner band) and the total systematic uncertainties, including the one on the hadronic model (outer band).

As can be seen, the DAMPE p+He spectrum extends for the first time, with unprecedented precision, up to 316 TeV, showing clear evidence of the softening at 26.4 ± 3.6 TeV with the high significance of 6.7σ. The high-energy limit reached by ATIC is $\sim$ 30 TeV, CREAM-III goes up to $\sim$ 90 TeV, while NUCLEON extends to more than 200 TeV, but the reported uncertainties are large and the spectral behavior in the highest energy region is not well defined. Apart from the extension to higher energy, the result from this work shows smaller uncertainties, while being in agreement with other direct measurements at low energies.

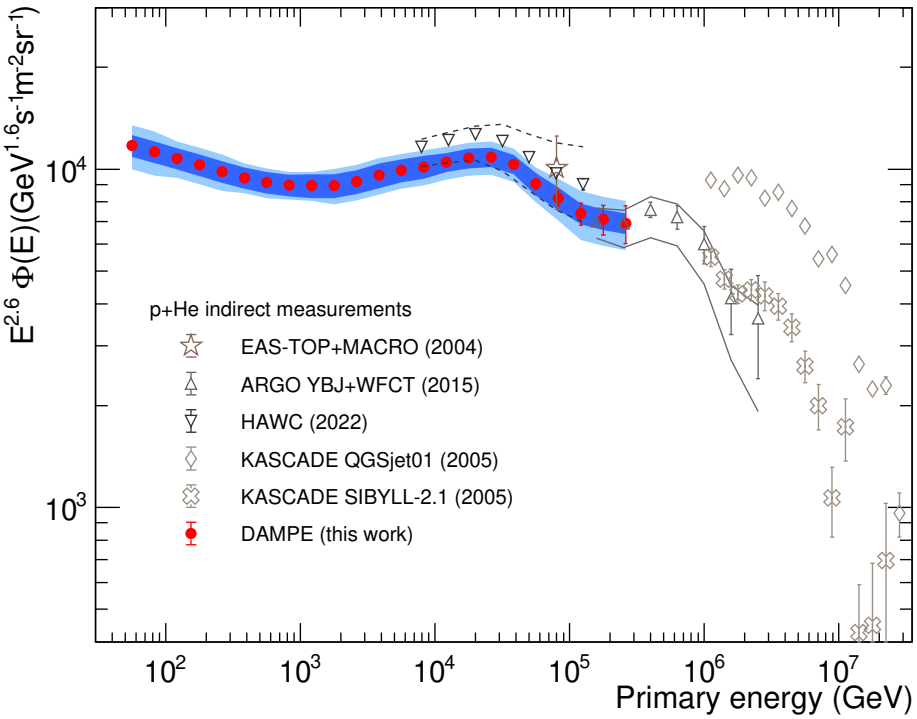

Figure 4.24: The p+He energy spectrum measured with this work, between 46 GeV and 316 TeV, compared with indirect measurements from ARGO-YBJ+WFCT [42], HAWC [43], KASCADE [44] and EAS-TOP+MACRO [45]. Statistical uncertainties (1σ) are represented by error bars, while the continuous bands represent the systematic uncertainties on the analysis (inner band) and the total systematic uncertainties, including the one on the hadronic model (outer band).

Another interesting outcome of this work (which is also one of the main motivations behind performing this spectral measurement) is the possibility of having a comparison between direct and indirect detection experiments. In general, the latter can hardly separate different CR species, but some of them were able to distinguish light and heavy CR components, consequently giving the possibility of comparing measurements performed from the ground and from space. The DAMPE spectrum is in agreement with the results reported from HAWC, MACRO+EAS-TOP and ARGO-YBJ, further confirming the softening and giving the hint of a second hardening for energy larger than 100 TeV (also proposed by HAWC in [88]), before a possible knee below 1 PeV. As described in section 1.4, the CR all-particle spectrum exhibits two major features which are the knee at $\sim$ 3 PeV and the ankle at $\sim$ 5 EeV. Focusing on the first feature, various interpretations were given on its nature over the past years (see section 1.6.3 for further detail) one of these being the transition of the CR composition from light to heavy. If this is the case, the observed knee at $\sim$ 3 PeV should be the result of the superimposition of different CR species knees, starting from lower energy for the light component and progressively going to higher energy for heavier nuclei. In this context, the measurement of ARGO-YBJ suggests the presence of a light-component knee at $\sim$ 700 TeV while also showing a very good agreement with DAMPE at low energies. In addition to this scenario, KASCADE suggested two possible evolutions of the p+He spectrum, based on the selected hadronic interaction model (QGSjet01 or SIBYLL-2.1), as shown in Fig. 4.24. The aforementioned results open multiple possibilities for the p+He spectrum. A light component knee could be present just below 1 PeV (before the all-particle knee) as suggested by ARGO-YBJ. The spectrum could soften slowly from $\sim$ 100 TeV to tens of PeV, following the higher-energy knee reported by KASCADE-SIBYLL-2.1. There could be another hardening at hundreds of TeV, linking the DAMPE spectrum with the KASCADE-QGSjet01 one, with the knee foreseen at PeV energies (as the previous one). Finally, new unexpected features could come out from a precise direct measurement at higher energy. A direct investigation of the PeV energy region would possibly aid in answering fundamental questions of CR physics such as the nature of the knee, finally giving a hint on the maximum achievable energy of galactic accelerators. Moreover, considering that indirect measurements rely on interaction models more than direct ones (leading to larger uncertainties in the measurements), it is essential to compare ground-based

results with precise measurements from space since this could give a sort of calibration at low energies, thus reducing the uncertainties at larger energies. A significant contribution was given by this result on the p+He spectrum.

In conclusion, the comparison with both space-based and ground-based experiments shows a generally good agreement, within the uncertainties while also unveiling new spectral features. The DAMPE p+He spectrum allowed measuring the softening at tens of TeV with unprecedented significance while exploring the high-energy region with remarkably small uncertainties, which could become even lower by collecting more statistics and with improved analysis methods (i.e. adopting machine learning techniques as described in [89], [90], [91] and performing accurate studies on the hadronic models). Moreover, in the future, the spectrum could be extended to higher energies with upcoming space-based experiments such as HERD [21], eventually confirming the presence of a light-component knee at energies below the knee of the all-particle spectrum. Additionally, the study of heavier nuclei can shed new light on the nature of the softening, finally defining whether it is a mass or charge dependent feature, and confirming the transition to a heavier GCR population in the knee energy region. Precise measurements made by space-borne instruments in the unexplored TeV-PeV energy region are fundamental to finally revealing distinctive features of high-energy CRs.

Conclusion

This work described the p+He spectral measurement in the energy range between 46 GeV and 316 TeV using 72 months of data collected with the DAMPE satellite.

The motivation behind this study has its roots in investigating fundamental cosmic ray (CR) properties. It follows that a description of CR physics is needed to introduce this work. For this reason, after a short introduction, in Chapter 1 CRs were characterized starting from their discovery more than 100 years ago and continuing with the development of various experimental techniques, optimized for their study, going from deep underwater to outside the Earth's atmosphere. At the same time, CR models were in development with the aim of explaining the observations and predicting what could be happening in extreme corners of the universe. Throughout the years, improved measurements provided extremely precise results on the energy spectra of CR nuclei revealing unexpected features. Specifically, the single power-law energy spectrum predicted for galactic CRs, below the all-particle knee, seems to be not valid anymore and has been replaced by a smoothly-broken power-law spectrum with at least two changes of slope. The first one consists of a hardening of the GCR spectra at hundreds of GeV and has been extensively measured and confirmed by several direct measurements. The second one is a novel softening feature at tens of TeV, measured for the first time by DAMPE in the proton and helium spectra and recently confirmed by the CALET collaboration for protons. While the hardening feature seems to be due to a change in the diffusion coefficient and has been widely studied in recent years, the change of slope at tens of TeV (softening) raised new questions and needs to be further investigated in order to clarify its nature (e.g., acceleration, propagation, or maybe the presence of nearby sources). Specifically, more precise measurements could exclude any contamination or detector effect. Moreover, further analyses on other nuclei or with lower statistical and systematic uncertainties could clarify whether the softening is a mass-dependent

or charge-dependent feature.

Direct measurements made with calorimetric experiments explored the high-energy region up to tens of TeV, with small uncertainties. Beyond this energy, only ground-based experiments were able to provide results, often affected by large uncertainties. Indeed, indirect measurements of the combined p+He spectrum, obtained discrepant results regarding the exact energy of the knee, possibly suggesting a light component knee occurring at lower energy than the all-particle one.

This scenario led to the study discussed in this thesis. A combined p+He analysis allows applying loose analysis cuts while keeping the contamination low with respect to studying proton or helium separately. This implies a noticeable increase in statistics, thus the possibility of extending the spectrum to energies previously unexplored from space, building an overlapping region between direct and indirect CR measurements.

The p+He spectrum has been studied using the data collected with the DAMPE satellite. In order to provide a better understanding of this analysis, Chapter 2 presented a description of the experiment. The scientific goals and a selection of the obtained results have been reported, along with the various sub-detectors, each one playing an important and distinct role in achieving the p+He measurement.

The following two chapters fully described the analysis procedure. Chapter 3 gave a detailed account of the event selection process, highlighting the specific contributions of each individual DAMPE sub-detector and how they are combined in order to extract information about incoming particles and nuclei. Finally, the chapter concluded with the definition of the p+He sample of interest, selected from the millions of data collected every day by the DAMPE satellite.

Afterwards, in Chapter 4, the energy reconstruction process has been described. The procedure begins with the calorimeter measurement that is coupled with accurate MC simulations, to obtain the energy of the primary particle adopting a Bayesian unfolding procedure. The chapter also covers the evaluation of statistical and systematic uncertainties associated with this measurement. Finally, the p+He energy spectrum has been presented and compared with DAMPE results on proton and helium alone, as an internal cross-check.

The p+He spectrum presented in this study confirms the hardening and softening features observed in the proton and helium spectra. The softening has been studied through a smoothly-broken power-law fit, yielding the remarkable signifi-

cance of 6.7σ, thus discarding any contamination or detector effect. The DAMPE p+He spectrum obtained in this thesis extended the direct measurements to a previously unexplored energy region with unprecedented uncertainties. This work has been therefore submitted for publication and can be found at [20]. The obtained result suggests the presence of unexpected features while also giving important contributions to a better understanding of the effect of hadronic interaction model uncertainties. The emerging picture strongly suggests the need for a next-generation (larger exposure) calorimetric space-based experiment, able to fully explore the PeV region for protons and heavier nuclei.

Appendix A

Proton+Helium Charge Selection

The selection of proton+helium (p+He) candidates has been illustrated in section 3.2.3. Specifically, the signal recorded in the Plastic Scintillator Detector (PSD) of DAMPE is mainly defined by the particle's charge (according to the Bethe-Bloch formula) and also depends on the particle's primary energy. In order to take into account the aforementioned characteristics, the signal recorded in the PSD is combined with the energy deposited in the BGO calorimeter (*BGO Energy* hereafter) event per event, resulting in an energy-dependent charge selection. For what concerns this analysis, the signal acquired using the 4 PSD layers, is combined in a single value of deposited energy that was identified with the name of *PSD Global energy* and is defined in eq. 3.1. The proton+helium PSD global energy deposit results in two peaks (as shown in the figures reported in this appendix) and is fit in different bins of BGO energy, using a Landau (to consider the expected energy distribution of energy deposit by an ionizing particle) convoluted with a Gaussian function (representing the detector effects). The same procedure is applied to data from the satellite (called *flight data*), shown in Fig. A.1, A.2 and A.3 and Monte Carlo simulated data (MC), reported in Fig. A.4, A.5 and A.6.

A.1 PSD deposited energy distribution for flight data

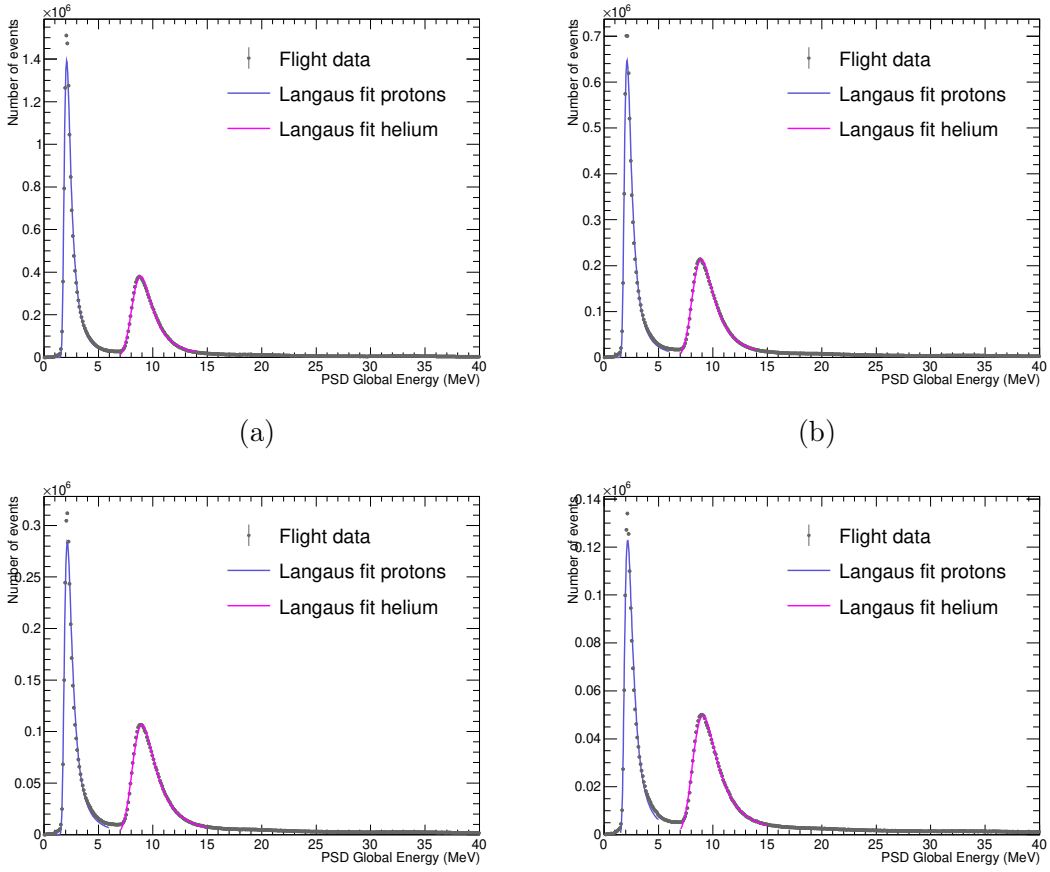

Figure A.1: Distributions of PSD Global energy for various BGO energy bins: (a) 25 GeV - 39 GeV, (b) 39 GeV - 63 GeV, (c) 63 GeV - 100 GeV, (d) 100 GeV - 158 GeV. The flight data distributions of proton and helium are shown with grey points, along with their LanGaus fits, in blue for protons and magenta for helium.

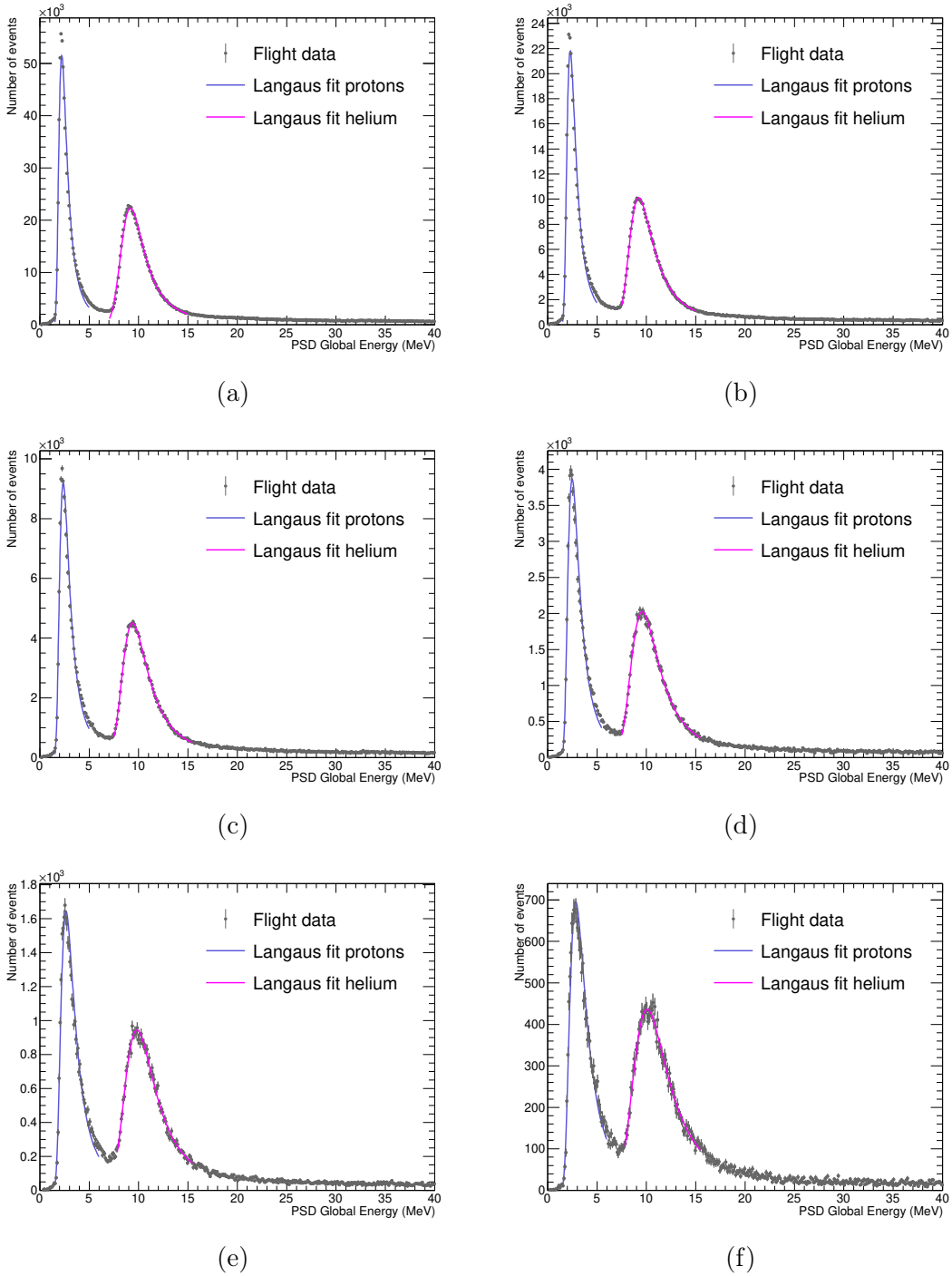

Figure A.2: Distributions of PSD Global energy for various BGO energy bins: (a) 158 GeV - 251 GeV, (b) 251 GeV - 398 GeV, (c) 398 GeV - 630 GeV, (d) 630 GeV - 1000 GeV, (e) 1.0 TeV - 1.6 TeV, (f) 1.6 TeV - 2.5 TeV. The flight data distributions of proton and helium are shown with grey points, along with their LanGaus fits, in blue for protons and magenta for helium.

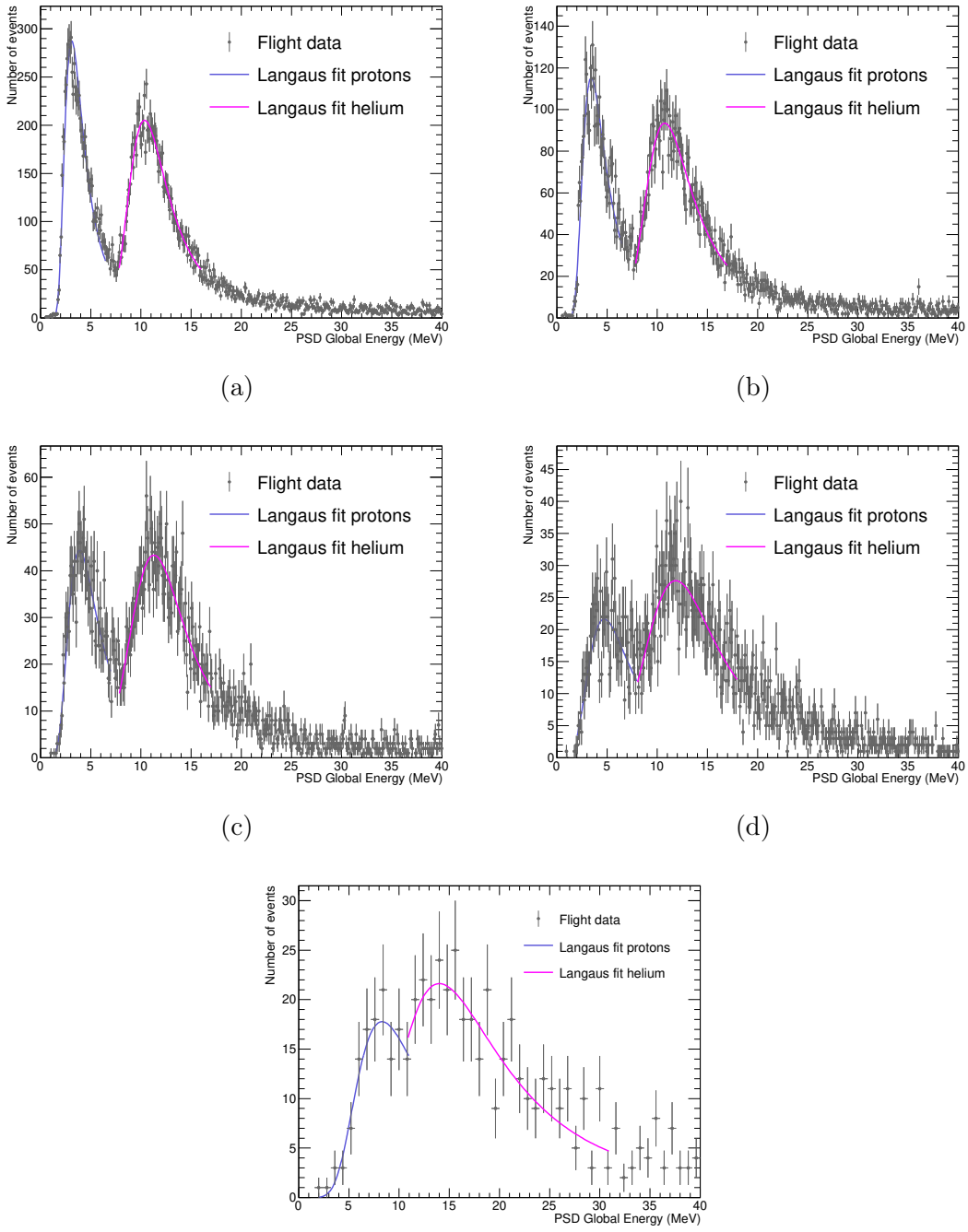

Figure A.3: Distributions of PSD Global energy for various BGO energy bins: (a) 2.5 TeV - 4.0 TeV, (b) 4.0 TeV - 6.3 TeV, (c) 6.3 TeV - 10.0 TeV, (d) 10.0 TeV - 31.6 TeV, (e) 31.6 TeV - 100.0 TeV. The flight data distributions of proton and helium are shown with grey points, along with their LanGaus fits, in blue for protons and magenta for helium.

A.2 PSD deposited energy distribution for MC data

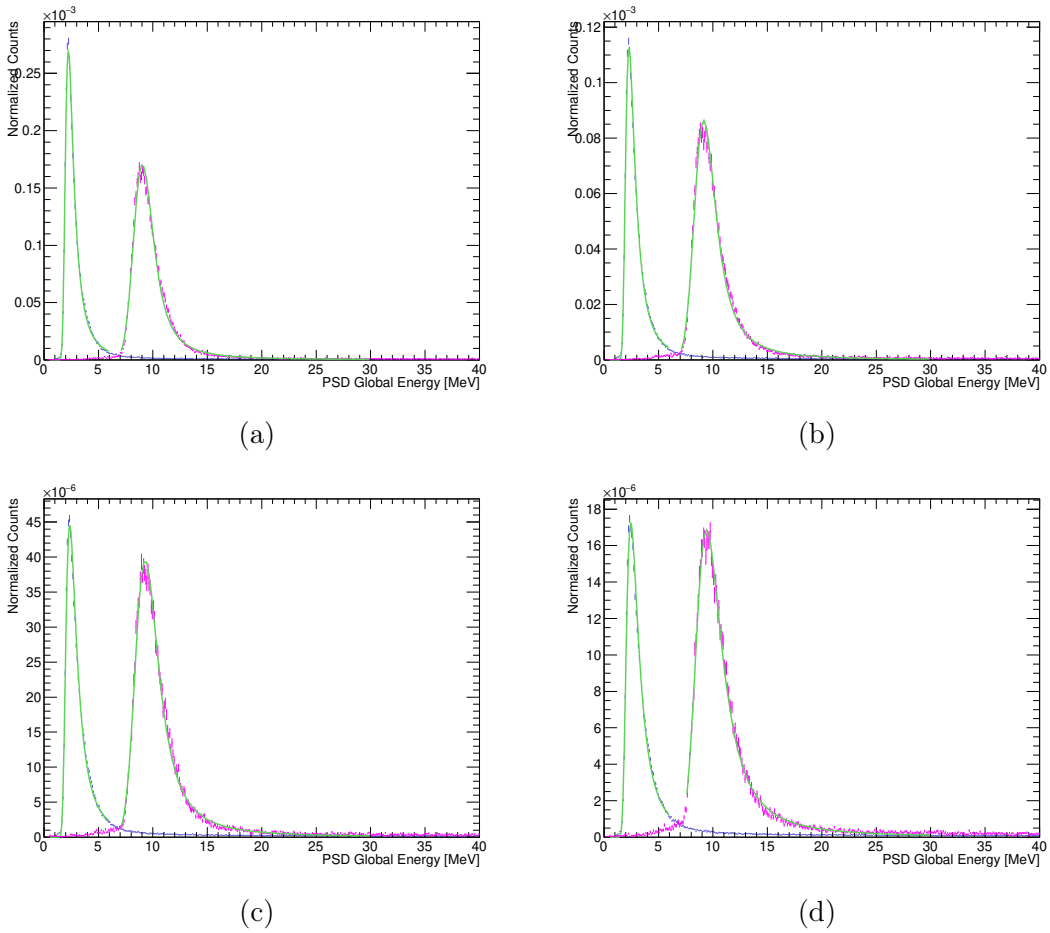

Figure A.4: Distributions of PSD Global energy for various BGO energy bins: (a) 25 GeV - 39 GeV, (b) 39 GeV - 63 GeV, (c) 63 GeV - 100 GeV, (d) 100 GeV - 158 GeV. The MC distributions of proton (in blue) and helium (in magenta) are shown, along with their LanGaus fits (green lines).

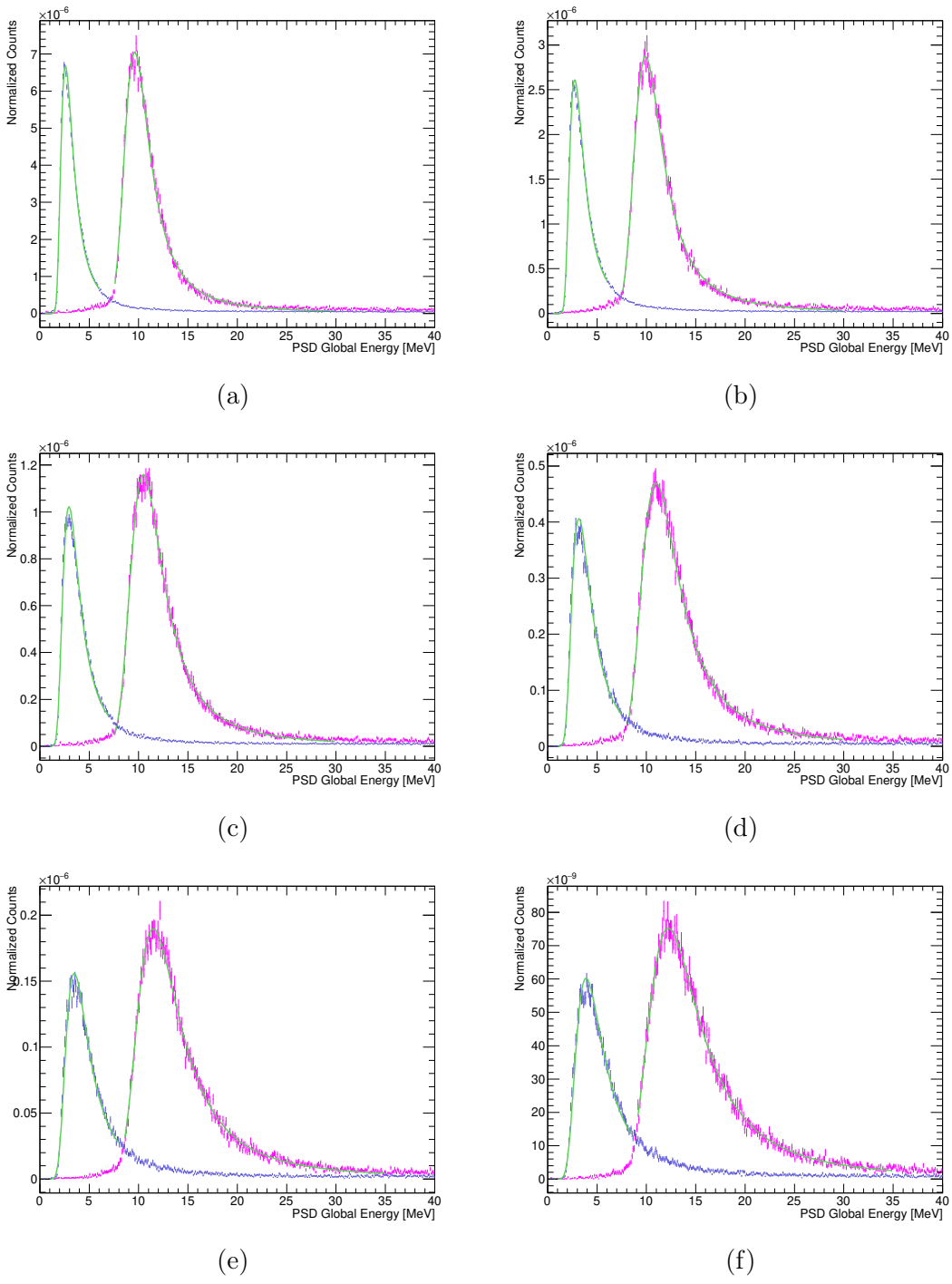

Figure A.5: Distributions of PSD Global energy for various BGO energy bins: (a) 158 GeV - 251 GeV, (b) 251 GeV - 398 GeV, (c) 398 GeV - 630 GeV, (d) 630 GeV - 1000 GeV, (e) 1.0 TeV - 1.6 TeV, (f) 1.6 TeV - 2.5 TeV. The MC distributions of protons (in blue) and helium (in magenta) are shown, along with their LanGaus fits (green lines).

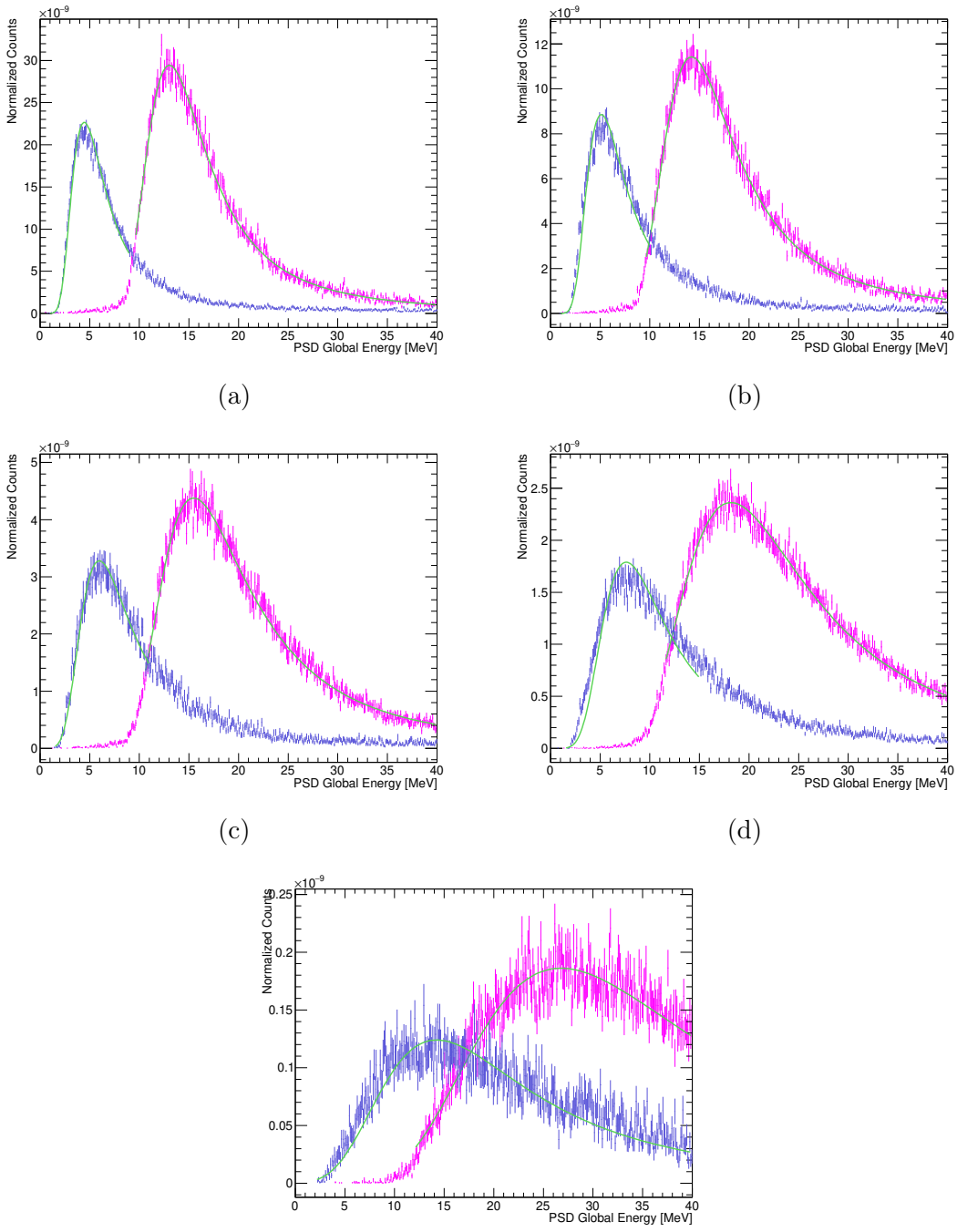

Figure A.6: Distributions of PSD Global energy for various BGO energy bins: (a) 2.5 TeV - 4.0 TeV, (b) 4.0 TeV - 6.3 TeV, (c) 6.3 TeV - 10.0 TeV, (d) 10.0 TeV - 31.6 TeV, (e) 31.6 TeV - 100.0 TeV. The MC distributions of protons (in blue) and helium (in magenta) are shown, along with their LanGaus fits (green lines).

Appendix B

BGO saturation correction

The BGO calorimeter is the DAMPE fundamental detector for energy measurement and for electron-proton separation (the description of this sub-detector is given in section 2.5). Each BGO crystal is read out on both ends by one PMT instrumented with 3 dynodes, each one with a different gain, resulting in a wide dynamic range (see Fig. 2.12). One of the DAMPE main scientific goals is to measure CR nuclei up to hundreds of TeV. For the highest-energy events, the energy deposited in a single BGO bar can exceed tens of TeV, causing the saturation of the low gain channel, thus losing the deposited energy information, for that particular high-energy event. Specifically, for proton and helium nuclei, this effect starts taking place from an energy deposit of $\sim$ 20 TeV. An example of helium saturated event is presented in Fig. B.1.

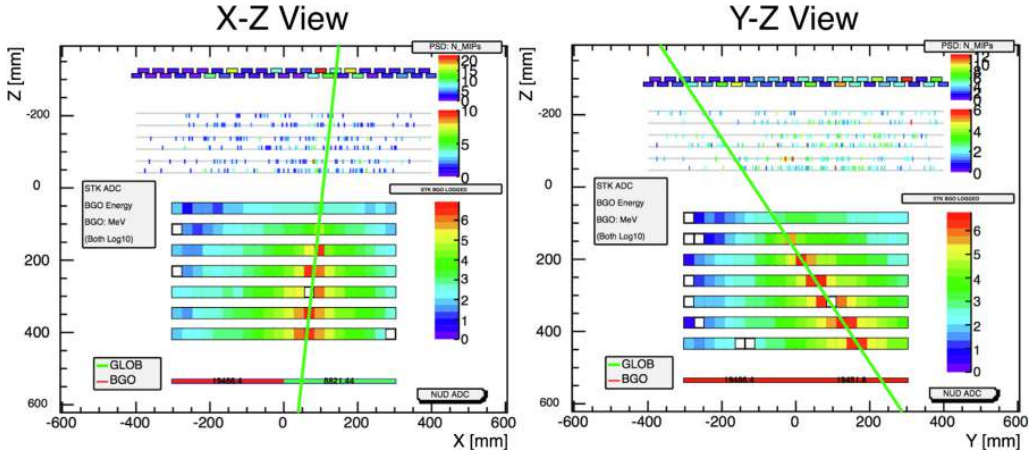

Figure B.1: Event display representing a helium event in the DAMPE detector with a saturated BGO bar. The white box on the shower axis is the saturated bar, while the other white boxes are bars in which there is no energy deposit, or a deposition lower than the threshold [54].

Considering that the energy information in the saturated bar is lost, a method has been developed to estimate this missing value, based on the energy deposited in the neighboring BGO crystals. The details of this method are illustrated in [54] and will be briefly reported hereafter. The correction is performed in two steps. The first step consists in estimating the energy deposit in the saturated bar by looking at the signal in its left and right neighboring bars, through the variable η_{LR} defined as follows:

$$\eta_{\mathrm{LR},j} = \frac{E_{\mathrm{Max},j}}{E_{\mathrm{Max},j} + E_{\mathrm{Left},j} + E_{\mathrm{Right},j}}. \tag{B.1}$$

$E_{\mathrm{Max},j}$ represents the maximum deposited energy in the *j-th* BGO layer while $E_{\mathrm{Left},j}$ and $E_{\mathrm{Right},j}$ are the energy deposit in the left and right neighboring bars. Afterwards, $\eta_{\mathrm{LR},j}$ is computed for different values of primary energy and fit with a polynomial function of the energy deposit in a layer. Considering that the bar with the maximum energy deposition will be the saturated one, an initial assumption is made on the energy deposit which is $E_{\mathrm{Sat},j} = 5.5 \cdot (E_{\mathrm{Left},j} + E_{\mathrm{Right},j})$. Combining the aforementioned initial assumption with the results from the fit, $\eta_{\mathrm{LR},j}$ is estimated again and the energy of the saturated bar is evaluated as:

$$E_{\mathrm{Sat},j} = \frac{\eta_{\mathrm{LR},j}}{1 - \eta_{\mathrm{LR},j}} \cdot (E_{\mathrm{Left},j} + E_{\mathrm{Right},j}) \,. \tag{B.2}$$

A first energy estimation for the saturated crystal is obtained with the procedure described above. As a second step, a more accurate energy value for the saturated bar can be obtained by considering the longitudinal development of the shower, hence looking at the energy deposit in the layers above and below the saturated bar. Consequently, an additional variable η_{UD} is defined as:

$$\eta_{\mathrm{UD},j} = \frac{E_{\mathrm{Max},j}}{E_{\mathrm{Max},j} + E_{\mathrm{Left},j} + E_{\mathrm{Right},j} + E_{\mathrm{Up},j} + E_{\mathrm{Down},j}}. \tag{B.3}$$

The estimated $\eta_{\mathrm{UD},j}$ is computed for different values of primary energy and fit with a polynomial function of the total deposited energy (estimated using the first step of this correction procedure). Also $\eta_{\mathrm{UD},j}$ is estimated anew, leading to a more accurate evaluation of the energy of the saturated bar, given by the following for-

mula:

$$E_{\mathrm{Sat},j} = \frac{\eta_{\mathrm{UD},j}}{1-\eta_{\mathrm{UD},j}} \times (E_{\mathrm{Left},j} + E_{\mathrm{Right},j} + E_{\mathrm{Up},j} + E_{\mathrm{Down},j}) \tag{B.4}$$

The reported method is valid when there is no more than one saturated BGO crystal in the same layer, and it showed good performance in reconstructing the energy released in the calorimeter for events up to 200 TeV, with uncertainty associated with the correction at the level of $\sim 2\%$. In order to reach higher energies, the method has been improved to consider and correct also the situation in which more than one saturated bar is present on the same BGO layer. Specifically, a correction variable η is defined as:

$$\eta = \frac{Min(E_L, E_R)}{Max(E_L, E_R)}, \tag{B.5}$$

where E_L (E_R) is the energy recorded in the bar on the left (right) of the saturated one. This correction is computed for all the BGO layers, up to 1 PeV of primary energy, and then associated with the left-right correction (η_{LR}). The ratio between simulated energy (E_{simu}) and deposited energy after correction for saturation (E_{cor}) is shown in Fig. B.2 for MC helium nuclei from 10 TeV to 1 PeV of primary energy. The *old method* represents the correction with only one saturated bar per layer, while the *new method* is valid also for adjacent saturated bars.

As can be inferred from Fig. B.2, this method works well for recovering the energy deposit in saturated BGO crystals. The same ratio E_{cor}/E_{simu} is shown in Fig. B.3 for various energy of the incident helium nuclei. The performance of this correction is very good up to $\sim$ 600-700 TeV, and some loss of linearity is present above this energy.

The developed method is fundamental and well-performing for the extension of CR energy spectra up to hundreds of TeV energy.

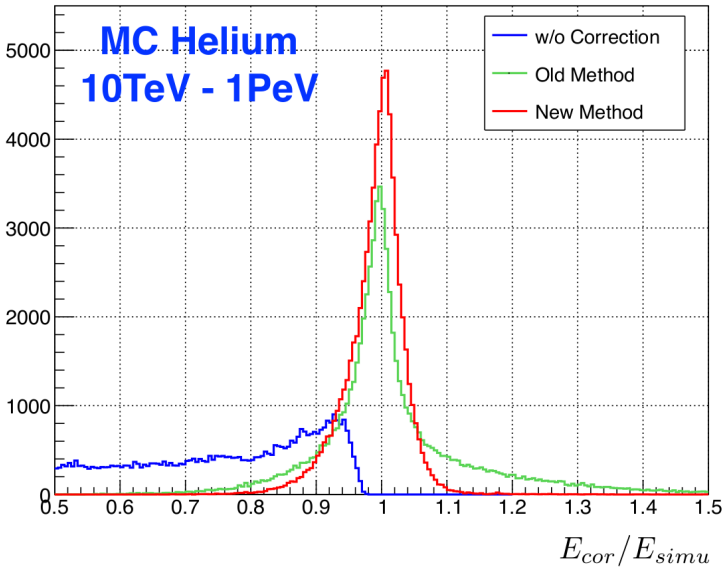

Figure B.2: Performance of the BGO saturation correction method for MC helium nuclei with energy between 10 TeV and 1 PeV. The histograms represent the ratio between simulated energy and deposited energy in the calorimeter in blue before the correction, in green with the correction applied only with one saturated bar per layer, and in red when more bars saturate (with the latter being important for primary energies larger than 200 TeV) [92].

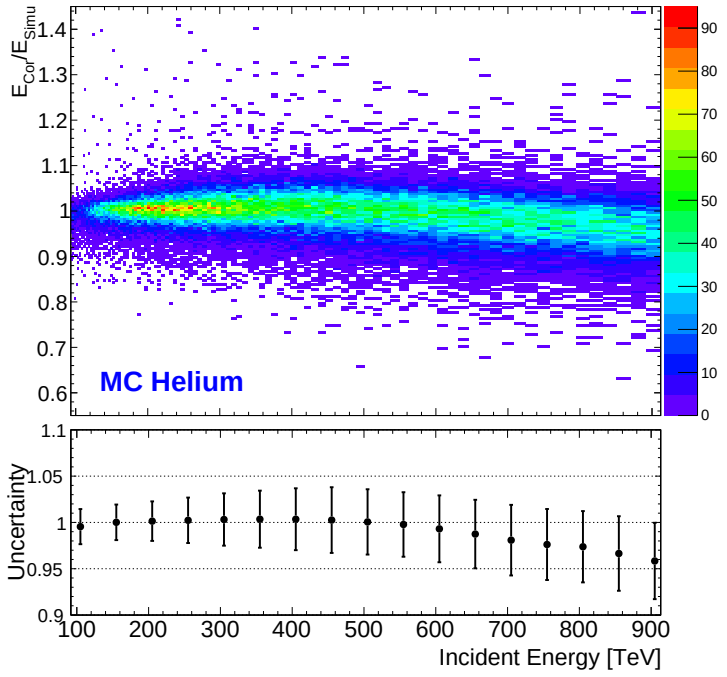

Figure B.3: Ratio between deposited energy after the latest correction for the BGO saturation (case of adjacent saturated bars) and simulated energy for MC helium. The method is effective up to hundreds of TeV, showing a slight loss of linearity after 600-700 TeV. The bottom panel shows the 1σ uncertainty on the correction [92].

Appendix C

Charge selection efficiency

After applying the selection cuts, their efficiencies are evaluated to compute the effective acceptance, which is a fundamental ingredient for performing the flux measurement. The same selection procedure is applied to MC data and flight data, and their efficiencies are compared, in order to evaluate their impact on the systematic uncertainties. Specifically, the charge selection efficiency has been discussed in section 4.4.1, and a sub-sample of the plots needed in the efficiency estimation process are reported in this appendix. The charge selection efficiency evaluation is performed by looking at the signal recorded with the PSD layers X and Y separately, in various bins of energy deposited in the BGO (*BGO energy*), for MC and flight data, as shown in Fig. C.1, C.2, C.3, C.4. The MC distributions are then corrected based on the energy deposit of flight data in the PSD, using the formula 3.2. The distributions are fit using a Landau convoluted with a Gaussian function (LanGaus) to extract the parameters reported in Fig. C.5, C.6, C.7, C.8, before the smearing correction and in Fig. C.9, C.10, C.11, C.12, after the smearing correction. The charge selection efficiency is evaluated using the following equations:

$$\epsilon_{PSD_1} = \frac{N_{PSD_1+PSD_2+STK_1}}{N_{PSD_2+STK_1}}, \tag{C.1}$$

$$\epsilon_{PSD_2} = \frac{N_{PSD_1+PSD_2+STK_1}}{N_{PSD_1+STK_1}}. \tag{C.2}$$

where ϵ_{PSD_1} (ϵ_{PSD_2}) represents the charge selection efficiency for the first (second) PSD layer, $N_{PSD_1+PSD_2+STK_1}$ is the number of p+He events selected using the information from both PSD layers and the STK plane, and $N_{PSD_2+STK_1}$ ($N_{PSD_1+STK_1}$) are the events selected using only the second (first) PSD layer and the STK signal.

The signal recorded in the STK is reported in Fig. C.14 and C.13. More details on the STK charge selection procedure are given in section 4.4.1. The efficiencies resulting from this process are given in Fig. 4.13 and 4.14, where the comparison between flight data and MC data shows that their difference is negligible up to $\sim$ 100 GeV and it reaches the maximum value of $\sim$ 3% for energy larger than 1 TeV only for the first PSD layer.

C.1 Distributions of energy deposit in PSD Layer X for flight data

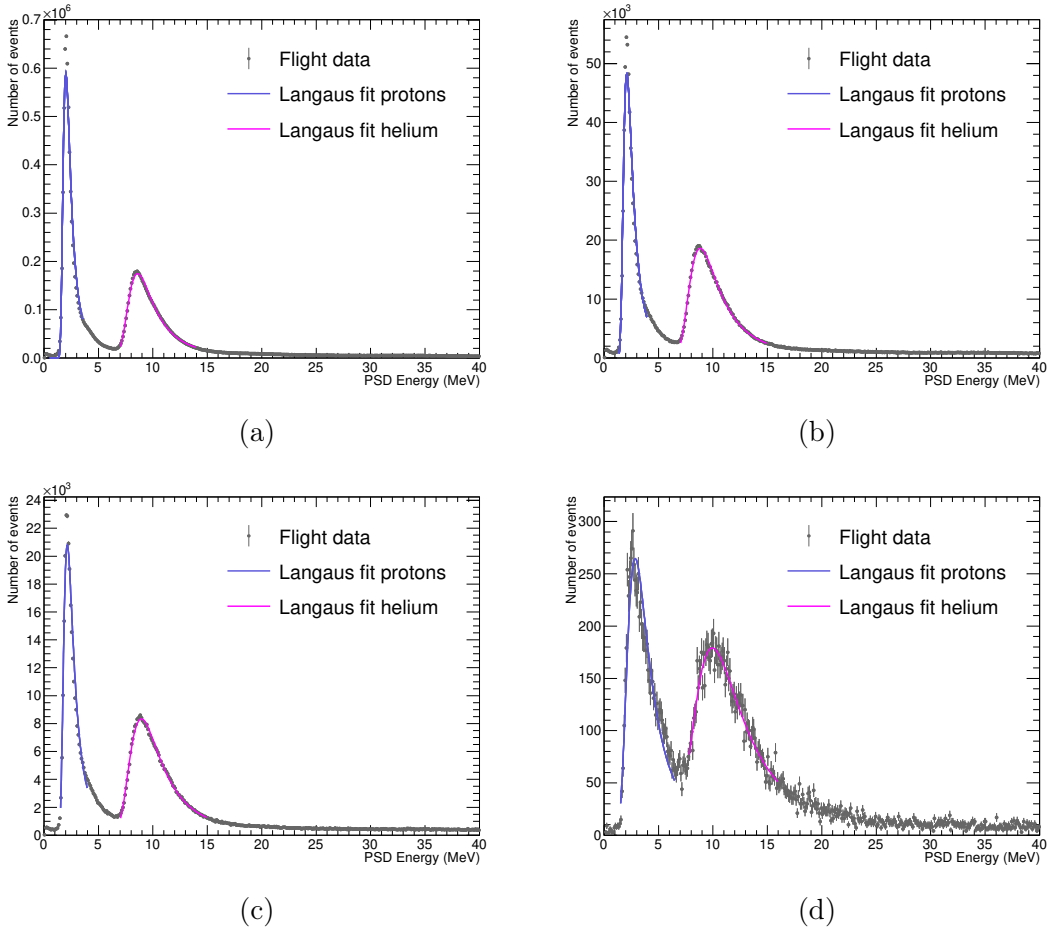

Figure C.1: Distributions of energy deposited in the layer X of the PSD for various BGO energy bins: (a) 39 GeV - 63 GeV, (b) 158 GeV - 251 GeV, (c) 398 GeV - 630 GeV, (d) 2.5 TeV - 4.0 TeV. The Flight data distributions of proton and helium are shown, along with their LanGaus fits.

C.2 Distributions of energy deposit in PSD Layer Y for flight data

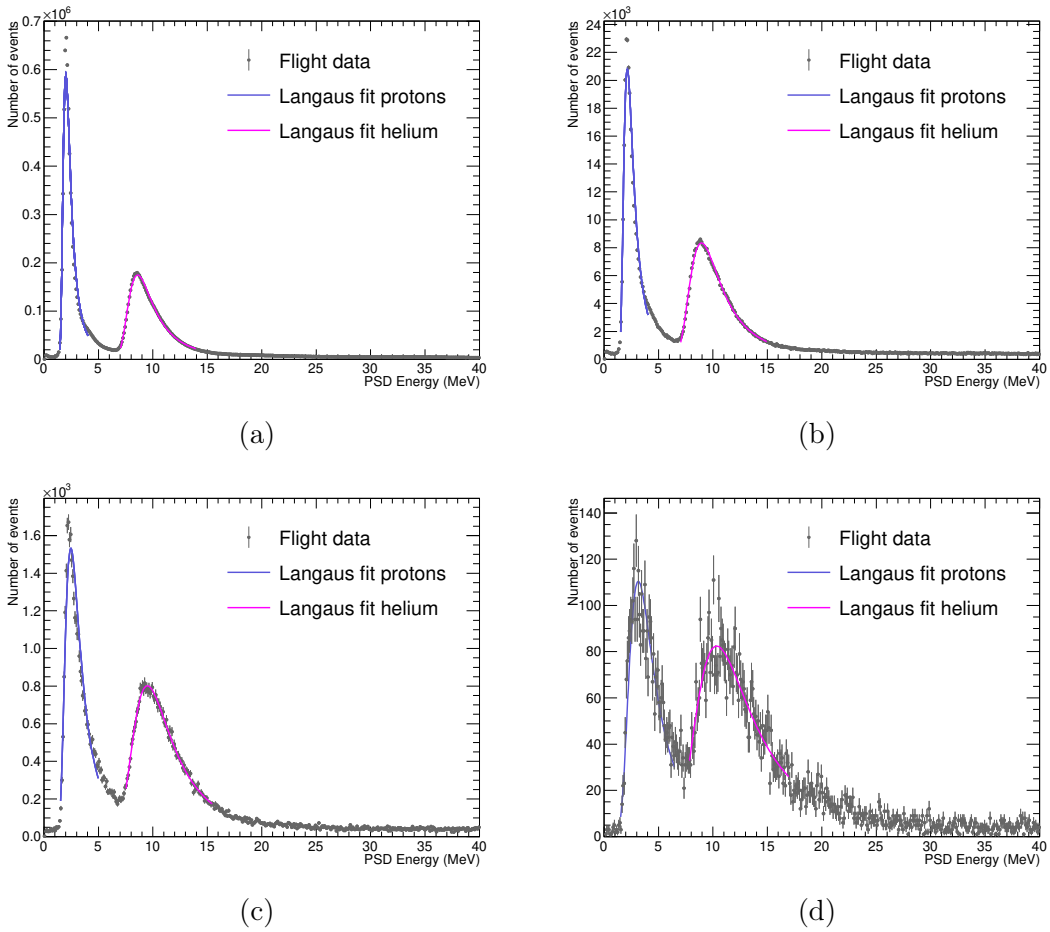

Figure C.2: Distributions of energy deposited in layer Y of the PSD for various BGO energy bins: (a) 39 GeV - 63 GeV, (b) 251 GeV - 398 GeV, (c) 1.0 TeV - 1.6 TeV, (d) 4.0 TeV - 6.3 TeV. The Flight data distributions of proton and helium are shown, along with their LanGaus fits.

C.3 Distributions of energy deposit in PSD Layer X for MC data

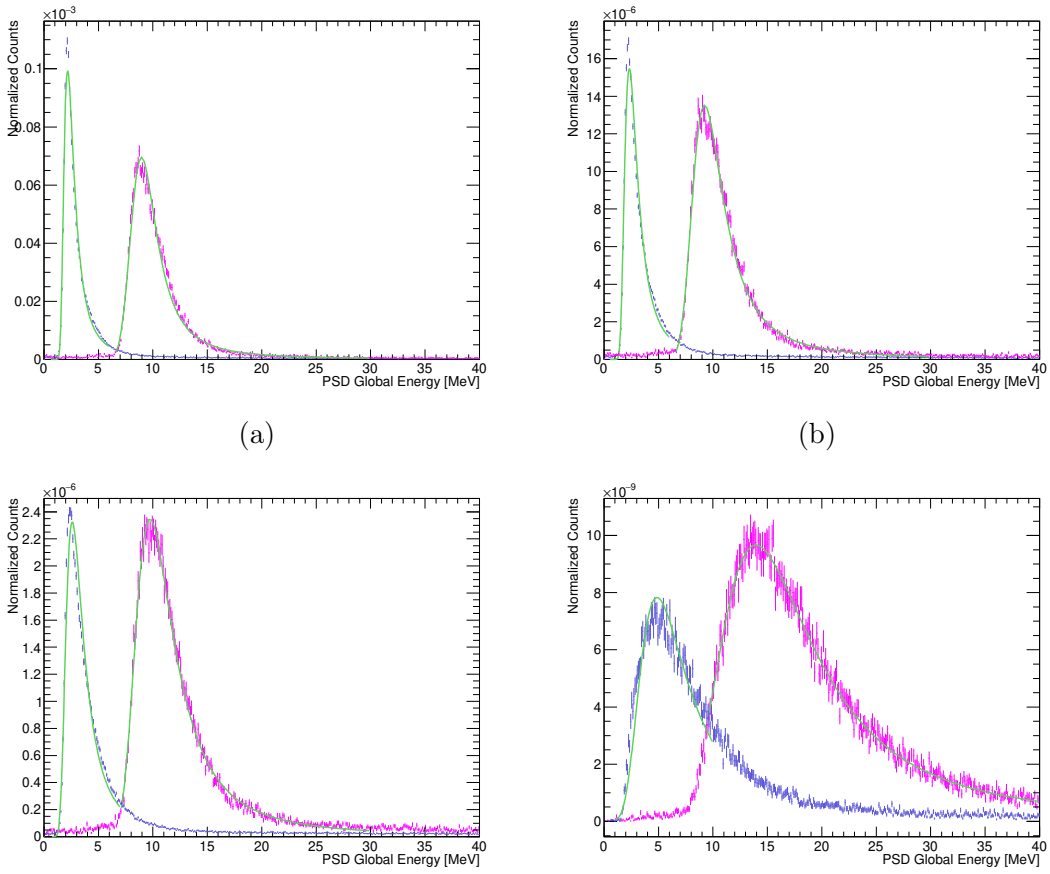

Figure C.3: Distributions of energy deposited in layer X of the PSD for various BGO energy bins: (a) 39 GeV - 63 GeV, (b) 100 GeV - 158 GeV, (c) 251 GeV - 398 GeV, (d) 4.0 TeV - 6.3 TeV. The MC distributions of proton (in blue) and helium (in magenta) are shown, along with their LanGaus fits (green line).

C.4 Distributions of energy deposit in PSD Layer Y for MC data

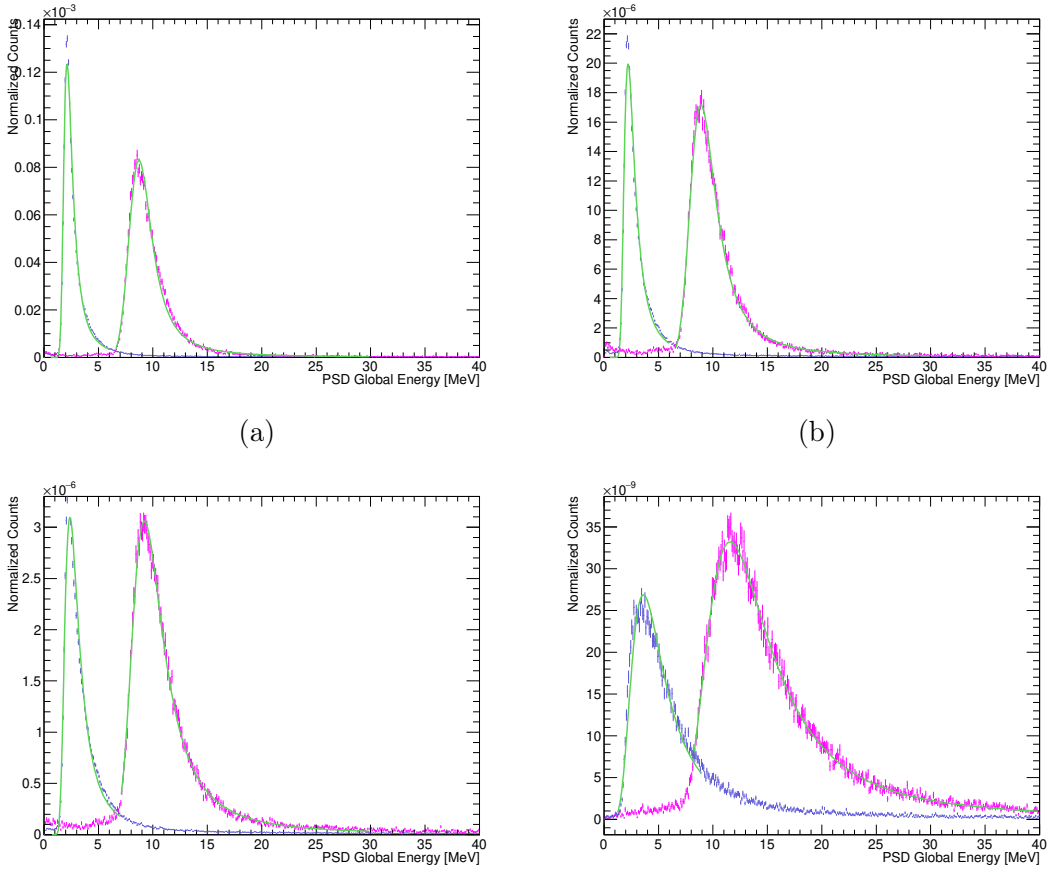

Figure C.4: Distributions of energy deposited in layer Y of the PSD for various BGO energy bins: (a) 39 GeV - 63 GeV, (b) 100 GeV - 158 GeV, (c) 251 GeV - 398 GeV, (d) 2.5 TeV - 4.0 TeV. The MC distributions of proton (in blue) and helium (in magenta) are shown, along with their LanGaus fits (green line).

C.5 MPV and Width before the smearing correction

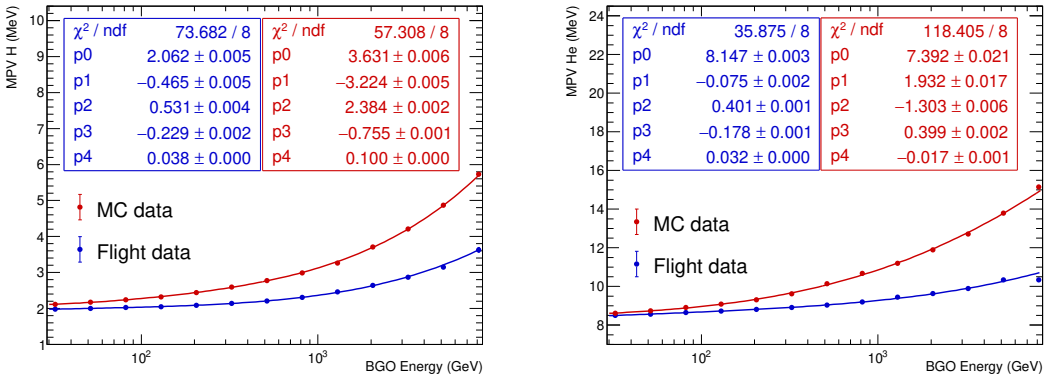

(a) (b)

Figure C.5: Most probable value (MPV) of the LanGaus fit for (a) protons and (b) helium in the X layer of the PSD, with respect to the energy deposited in the BGO. MC data (in red) and flight data (in blue) are shown, along with their fit functions and with the parameters extracted from the fit.

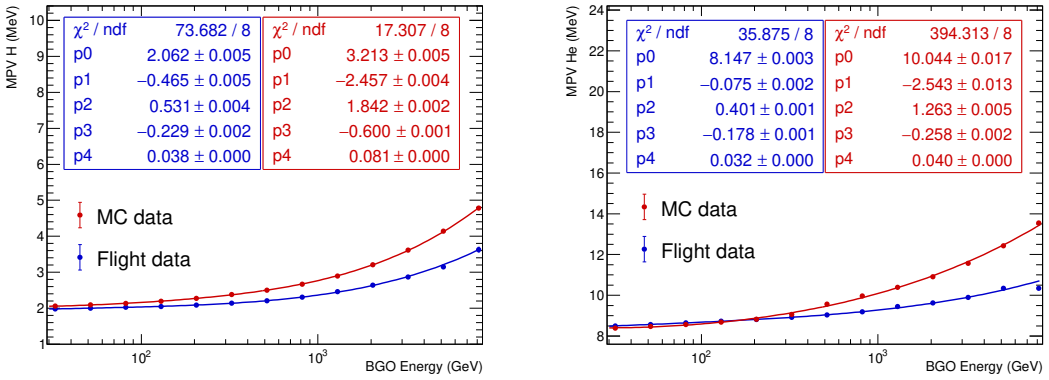

(a) (b)

Figure C.6: Most probable value (MPV) of the LanGaus fit for (a) protons and (b) helium in the Y layer of the PSD, with respect to the energy deposited in the BGO. MC data (in red) and flight data (in blue) are shown, along with their fit functions and with the parameters extracted from the fit.

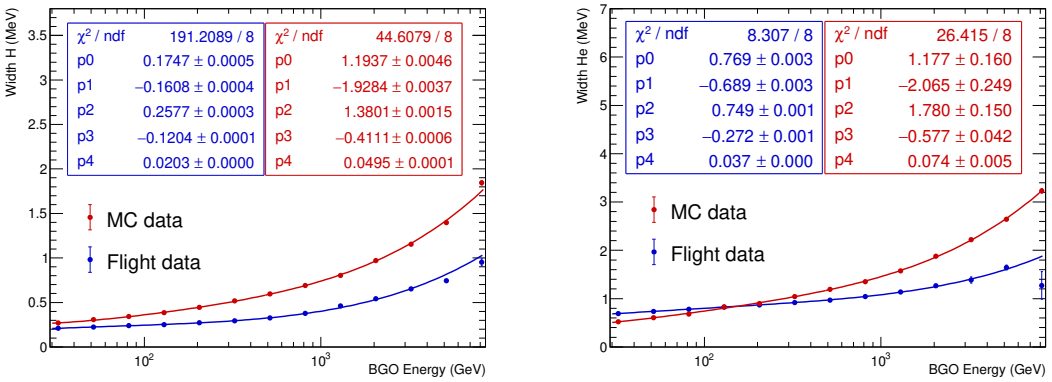

(a) (b)

Figure C.7: Width of the LanGaus fit for (a) protons and (b) helium in the X layer of the PSD, with respect to the energy deposited in the BGO. MC data (in red) and flight data (in blue) are shown, along with their fit functions and with the parameters extracted from the fit.

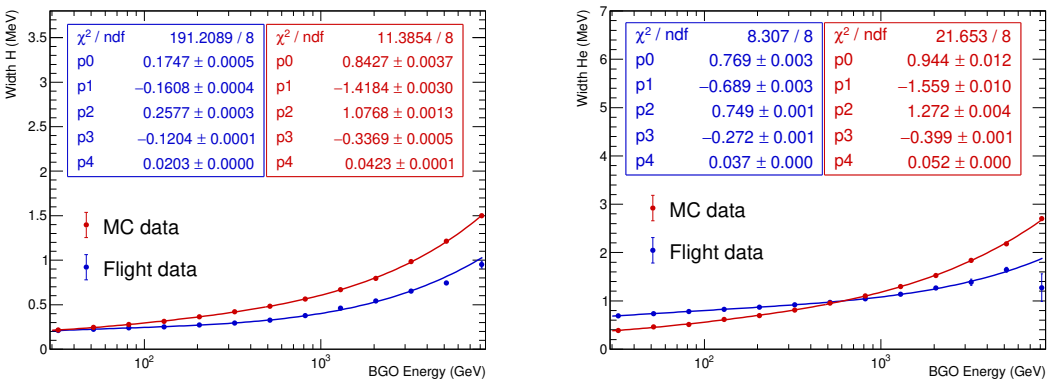

(a) (b)

Figure C.8: Width of the LanGaus fit for (a) protons and (b) helium in the Y layer of the PSD, with respect to the energy deposited in the BGO. MC data (in red) and flight data (in blue) are shown, along with their fit functions and with the parameters extracted from the fit.

C.6 MPV and Width after the smearing correction

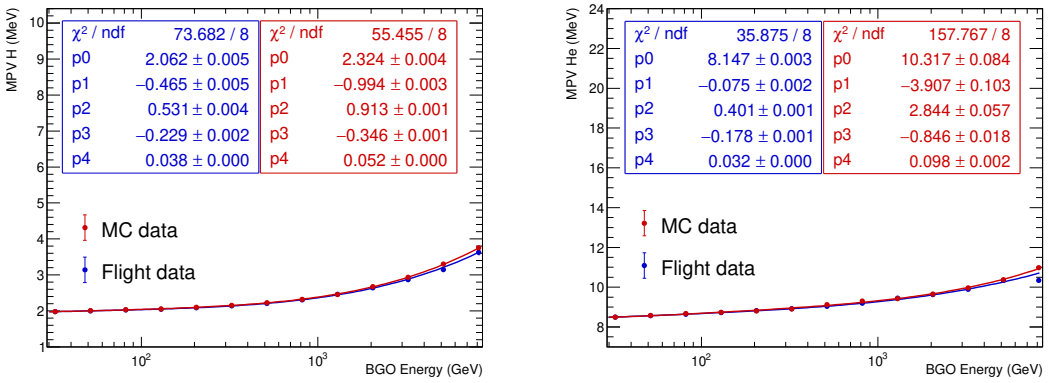

(a) (b)

Figure C.9: Most probable value (MPV) of the LanGaus fit for (a) protons and (b) helium in the X layer of the PSD after the smearing correction, with respect to the energy deposited in the BGO. MC data (in red) and flight data (in blue) are shown, along with their fit functions and with the parameters extracted from the fit.

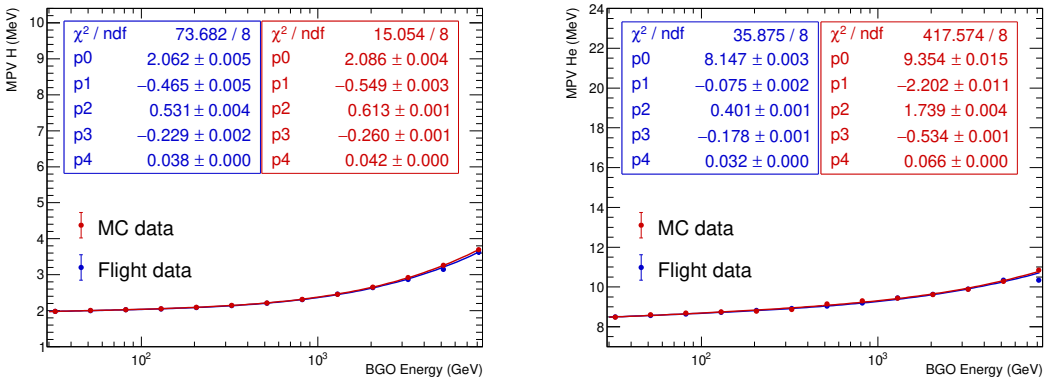

(a) (b)

Figure C.10: Most probable value (MPV) of the LanGaus fit for (a) protons and (b) helium in the Y layer of the PSD after the smearing correction, with respect to the energy deposited in the BGO. MC data (in red) and flight data (in blue) are shown, along with their fit functions and with the parameters extracted from the fit.

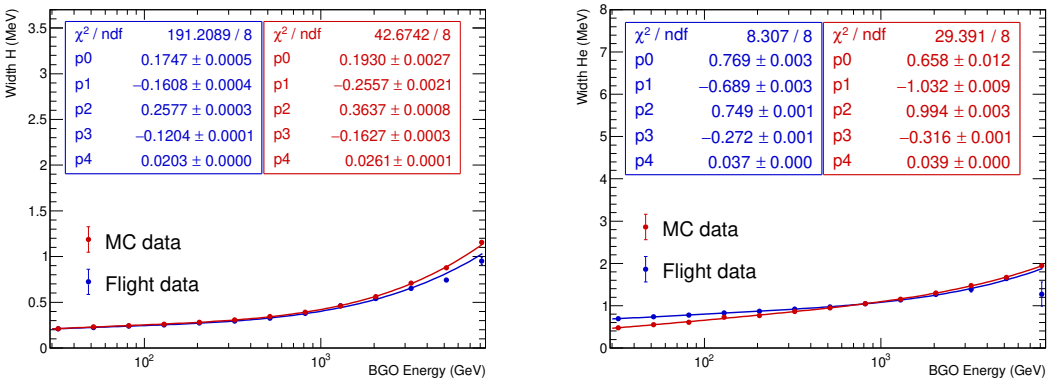

(a) (b)

Figure C.11: Width of the LanGaus fit for (a) protons and (b) helium in the X layer of the PSD after the smearing correction, with respect to the energy deposited in the BGO. MC data (in red) and flight data (in blue) are shown, along with their fit functions and with the parameters extracted from the fit.

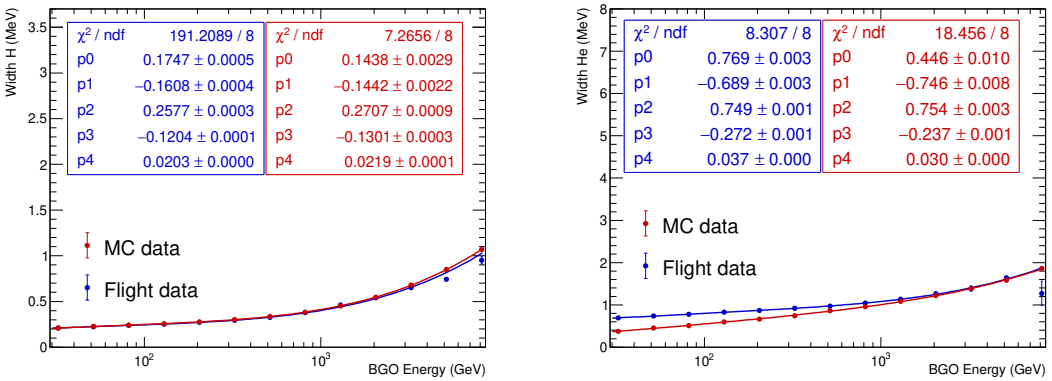

(a) (b)

Figure C.12: Width of the LanGaus fit for (a) protons and (b) helium in the Y layer of the PSD after the smearing correction, with respect to the energy deposited in the BGO. MC data (in red) and flight data (in blue) are shown, along with their fit functions and with the parameters extracted from the fit.

C.7 Distributions of energy deposit in the STK for MC data

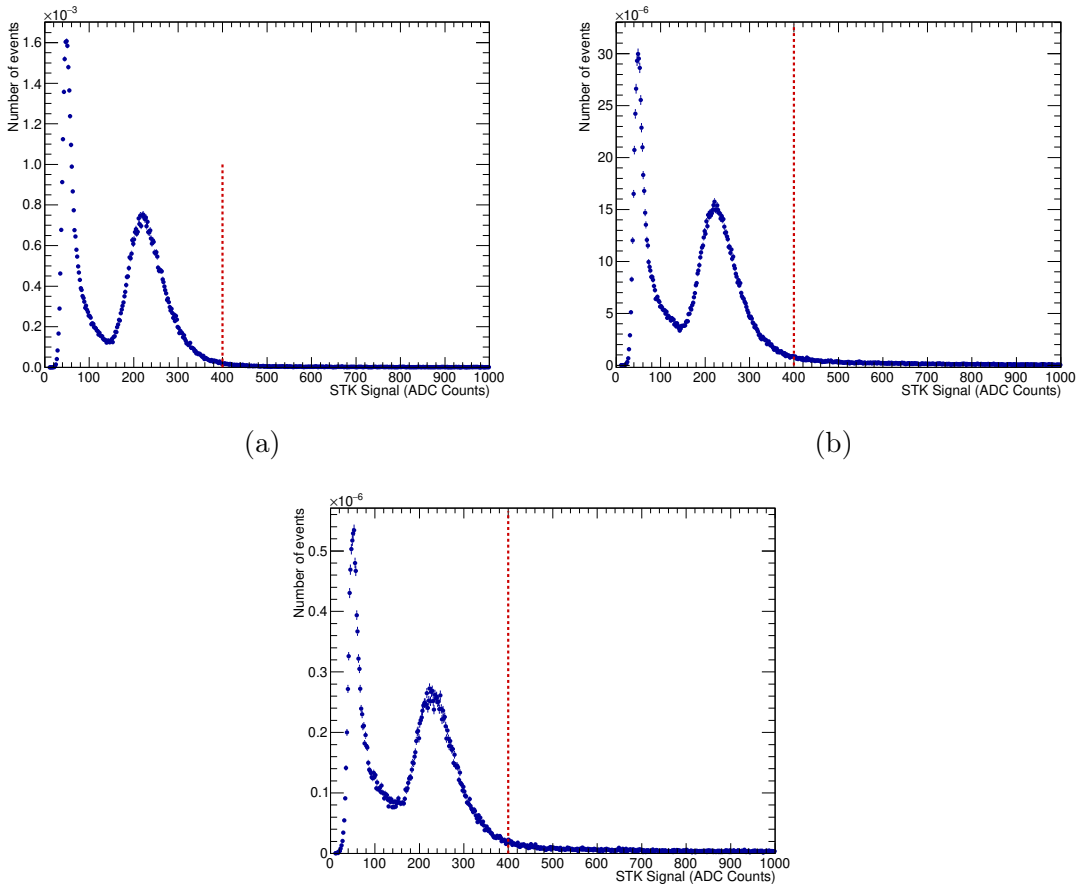

Figure C.13: Proton and helium simulated STK signal for energy deposited in the calorimeter in the range (a) 100 GeV - 1 TeV, (b) 1-10 TeV and (c) 10-100 TeV. The red dashed line represents the cut at 400 ADC Counts applied to compute the charge selection efficiency.

C.8 Distributions of energy deposit in the STK for flight data

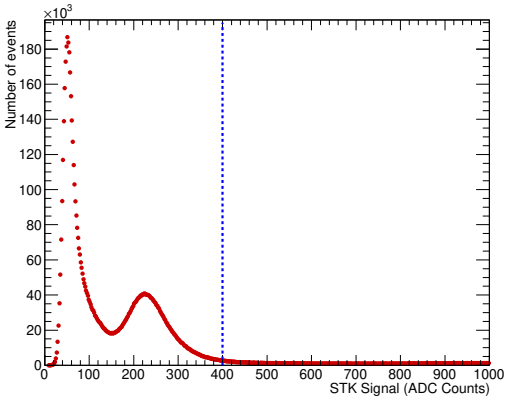

(a)

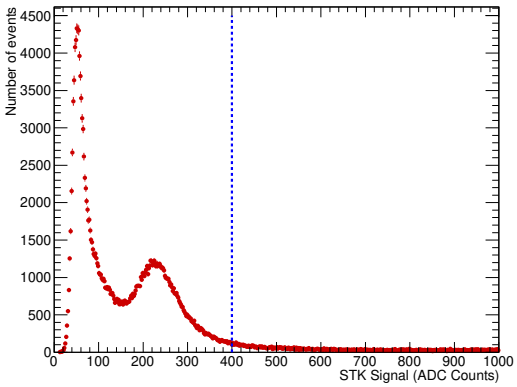

(b)

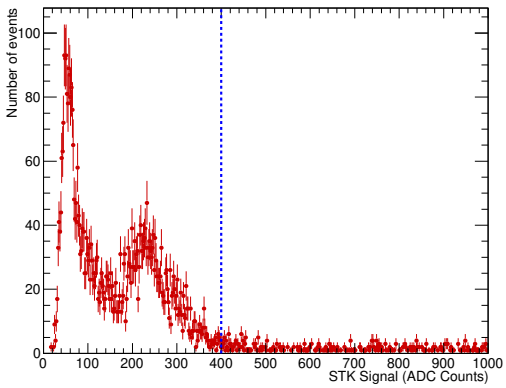

(c)

Figure C.14: Proton and helium STK signal in the data collected with the DAMPE satellite for energy deposited in the calorimeter in the range (a) 100 GeV - 1 TeV, (b) 1-10 TeV and (c) 10-100 TeV. The blue dashed line represents the cut at 400 ADC Counts applied to compute the charge selection efficiency.

Appendix D

Report of Ph.D. Activities

D.1 Publications

- "Measurement of the cosmic p+He energy spectrum from 46 GeV to 316 TeV with the DAMPE space mission", F. Alemanno et al. (DAMPE Collaboration) [20]. A paper based on this thesis. Submitted to PRL.

- "Detection of spectral hardenings in cosmic-ray boron-to-carbon and boron-to-oxygen flux ratios with DAMPE", F. Alemanno et al. (DAMPE Collaboration) [8].

- "Preliminary tests of Plastic Scintillator Detector for the High Energy cosmic-Radiation Detection (HERD) experiment", F. Alemanno, C. Altomare, F.C.T. Barbato, P. Bernardini, P.W. Cattaneo, I. De Mitri, F. De Palma, L. Di Venere, M. Di Santo, P. Fusco, F. Gargano, D. Kyratzis, F. Loparco, S. Loporchio, G. Marsella, M.N. Mazziotta, F.R. Pantaleo, A. Parenti, R. Pillera, M. Pullia, A. Rappoldi, G.L. Raselli, M. Rossella, D. Serini, L. Silveri, A. Surdo, L. Wu, for the HERD collaboration [93].

- "Assembly and test of prototype scintillator tiles for the plastic scintillator detector of the High Energy Cosmic Radiation Detection (HERD) facility", C. Altomare, F. Alemanno, F.C.T. Barbato, P. Bernardini, P.W. Cattaneo, I. De Mitri, F. De Palma, P. Dipinto, L. Di Venere, M. Di Santo, P. Fusco, F. Gargano, D. Kyratzis, F. Liciulli, F. Loparco, S. Loporchio, G. Marsella, M.N. Mazziotta, M. Mongelli, F.R. Pantaleo, M. Papagni, A. Parenti, R. Pillera, A. Rappoldi, G.L. Raselli, M. Rossella, D. Serini, L. Silveri, A. Surdo, R. Triggiani, for the HERD collaboration [94].

- "A complete MC optical photons tracking simulation of Plastic Scintillator Detectors for the next generation of satellite experiments", C. Altomare, F. Alemanno, F.C.T. Barbato, P. Bernardini, P.W. Cattaneo, I. De Mitri, F. De Palma, L. Di Venere, M. Di Santo, P. Fusco, F. Gargano, D. Kyratzis, F. Loparco, S. Loporchio, G. Marsella, M.N. Mazziotta, F.R. Pantaleo, A.

Parenti, R. Pillera, A. Rappoldi, G.L. Raselli, M. Rossella, D. Serini, L. Silveri, A. Surdo, for the HERD collaboration [95].

- "Latest results from the DAMPE space mission", Francesca Alemanno on behalf of the DAMPE collaboration [96].
- "Search for relativistic fractionally charged particles in space", F. Alemanno et al. (DAMPE Collaboration) [97].
- "The DAMPE Space Mission: Status and Main Results", Francesca Alemanno on behalf of the DAMPE collaboration [98].
- "Search for gamma-ray spectral lines with the DArk Matter Particle Explorer", F. Alemanno et al. (DAMPE Collaboration) [67].
- "Observations of Forbush Decreases of Cosmic-Ray Electrons and Positrons with the Dark Matter Particle Explorer", F. Alemanno et al. (DAMPE Collaboration) [99].
- "A neural network classifier for electron identification on the DAMPE experiment", D. Droz, A. Tykhonov, X. Wu, F. Alemanno, G. Ambrosi, E. Catanzani, M. Di Santo, D. Kyratzis, S. Zimmer [89].
- "Measurement of the light component (p+He) energy spectrum with the DAMPE Space Mission", F. Alemanno, P. Bernardini, A. De Benedittis, I. De Mitri, Z. Wang [100].
- "The Plastic Scintillator Detector of the HERD space mission", D. Kyratzis, F. Alemanno, C. Altomare, F.C.T. Barbato, P. Bernardini, P.W. Cattaneo, I. De Mitri, F. de Palma, L. Di Venere, M. Di Santo, P. Fusco, F. Gargano, F. Loparco, S. Loporchio, G. Marsella, M.N. Mazziotta, F.R. Pantaleo, A. Parenti, R. Pillera, A. Rappoldi, G. Raselli, M. Rossella, D. Serini, L. Silveri, A. Surdo, L. Wu [101].
- "Direct Measurement of the Cosmic-Ray Iron Spectrum with the Dark Matter Particle Explorer", Z. Xu, F. Alemanno, P. Ma, L. Silveri, Q. Yuan [102].
- "Measurement of the Cosmic Ray Helium Energy Spectrum from 70 GeV to 80 TeV with the DAMPE Space Mission", F. Alemanno et al. (DAMPE Collaboration) [9].
- "A preliminary study of influence of backsplash on the plastic scintillator detector design in HERD experiment", P. Hu, Z. Wang, F. Gargano, F. Alemanno, C. Altomare, T. Bao, Y. Dong, V. Formato, D. Kyratzis, N. Mori, L. Pacini, Z. Quan, D. Serini, J. Wang, R. Wang, M. Xu, B. Wu [103].
- "Correction Method for the Readout Saturation of the DAMPE Calorimeter", C. Yue, P. Ma, M. Di Santo, L. Wu, F. Alemanno, P. Bernardini, D. Kyratzis, G. Yuan, Q. Yuan, Y. Zhang [54].

- "Comparison of proton shower developments in the BGO calorimeter of the Dark Matter Particle Explorer between GEANT4 and FLUKA simulations", W. Jiang, C. Yue, M. Cui, X. Li, Q. Yuan, F. Alemanno, P. Bernardini, Z. Chen, T. Dong, G. Donvito, D. F. Droz, P. Fusco, F. Gargano, D. Guo, D. Kyratzis, S. Lei, Y. Liu, F. Loparco, P. Ma, G. Marsella, M. N. Mazziotta, I. De Mitri, X. Pan, W. Peng, A. Surdo, A. Tykhonov, Y. Wei, Y. Yu, J. Zang, Y.-P. Zhang, Y.-J. Zhang, Y.-L. Zhang [61].

- "The Quenching Effect of BGO Crystals on Relativistic Heavy Ions in the DAMPE Experiment", Y. Wei, Y. Zhang, Z. Zhang, L. Wu, H. Dai, C. Liu, C. Zhao, Y. Wang, Y. Zhao, P. Jiang, Y. Wang, F. Alemanno, M. Di Santo, E. Catanzani, X. Wang, Z. Xu, G. Huang [82].

D.2 Workshop and Conferences (talks and organization)

- UHECR2022: 6th International Symposium on Ultra High Energy Cosmic Rays, Oct 2022, L'Aquila, Italy. Part of the local organizing committee.

- Vulcano Workshop 2022 - Frontier Objects in Astrophysics and Particle Physics, Sep 2022, Elba Island, Italy. **Invited talk**: "Measurement of Cosmic Ray spectra with DAMPE and future prospects with the HERD space mission".

- COSPAR 2022 - 44th Scientific Assembly, Jul 2022, Athens, Greece. **Talk**: "Measurement of proton and helium energy spectra with the DAMPE space mission".

- Recontres de Moriond - Very High Energy Phenomena in the Universe, Mar 2022, La Thuile (AO), Italy. **Invited talk**: "Latest results from the DAMPE space mission". Chair of one of the cosmic ray sessions.

- Twentieth Lomonosov Conference on Elementary Particle Physics, Aug 2021, Online. **Talk**: "The DAMPE space mission: status and main results".

- 37th International Cosmic-Ray Conference (ICRC 2021), Jul 2021, Online. **Talk**: "Measurement of the light component (p+He) energy spectrum with the DAMPE space mission".

- 106° Congresso Nazionale SIF, Sep 2020, Online. **Talk**: "Measuring light elements in space with the DAMPE mission".

- 105° Congresso Nazionale SIF, Sep 2019, L'Aquila, Italy. **Talk**: "Measurement of the cosmic-ray proton + helium spectrum with DAMPE". Volunteer helping with conference activities.

D.3 Attended schools

- Twelfth I.N.F.N. International School on architectures, tools and methodologies for developing efficient large-scale scientific computing applications, Oct 2021, Bertinoro (FC), Italy. **Talk**: "The HERD space mission"
- VIII International Geant4 School, Nov 2019, Belgrade, Serbia.
- Joint 9th IDPASC SCHOOL and XXXI INTERNATIONAL SEMINAR of NUCLEAR and SUBNUCLEAR PHYSICS "Francesco Romano", Jun 2019, Otranto, Italy.

D.4 Collaboration meetings

- Bi-weekly working group meetings of DAMPE and HERD. Several presentations on work updates, in the period 2019-2023.
- 10th international DAMPE workshop, May 2022, online. **Talk**: "The p+He spectral measurement".
- DAMPE EU collaboration meeting, Jul 2020, online. **Talk**: "Update on the light element (p+He) analysis and studies towards the measurement of the heavy component (Fe)".
- 8th HERD Workshop, Dec 2019, Xi'an, China. **Talk**: "GEANT4-based simulation of light production/propagation/detection in bar-shaped PSD with SiPM readout @ GSSI".

D.5 Outreach activities

- SHARPER (European Researcher's night), Sep 2019 - Sep 2021, L'Aquila, Italy.
- 7th GSSI Astroparticle physics Science Fair, Mar 2021, Online. **Talk**: "The HERD space mission: overview and ongoing activities".
- International Cosmic Day (ICD), Nov 2019 - Nov 2020, L'Aquila, Italy.
- Premio Asimov (Asimov Prize), Apr 2019 - Apr 2020, Online.
- Outreach Cosmic Ray Activities (OCRA stage), Apr 2019, L'Aquila, Italy.

Bibliography

[1] R. Aloisio et al. "Selected Topics in Cosmic Ray Physics". In: *Multiple Messengers and Challenges in Astroparticle Physics*. Ed. by R. Aloisio, E. Coccia, and F. Vissani. Cham: Springer International Publishing, 2018, pp. 1–95. ISBN: 978-3-319-65425-6. DOI: 10.1007/978-3-319-65425-6_1. URL: https://doi.org/10.1007/978-3-319-65425-6_1.

[2] A. D. Panov et al. "Energy spectra of abundant nuclei of primary cosmic rays from the data of ATIC-2 experiment: Final results". In: *Bulletin of the Russian Academy of Sciences: Physics* 73 (2009), pp. 564–567.

[3] Q. An et al. "Measurement of the cosmic ray proton spectrum from 40 GeV to 100 TeV with the DAMPE satellite". In: *Science Advances* 5.9 (2019), eaax3793. DOI: 10.1126/sciadv.aax3793. eprint: https://www.science.org/doi/pdf/10.1126/sciadv.aax3793. URL: https://www.science.org/doi/abs/10.1126/sciadv.aax3793.

[4] O. Adriani et al. "Direct Measurement of the Cosmic-Ray Proton Spectrum from 50 GeV to 10 TeV with the Calorimetric Electron Telescope on the International Space Station". In: *Phys. Rev. Lett.* 122 (18 May 2019), p. 181102. DOI: 10.1103/PhysRevLett.122.181102. URL: https://link.aps.org/doi/10.1103/PhysRevLett.122.181102.

[5] H. S. Ahn et al. "DISCREPANT HARDENING OBSERVED IN COSMIC-RAY ELEMENTAL SPECTRA". In: *The Astrophysical Journal* 714.1 (Apr. 2010), pp. L89–L93. DOI: 10.1088/2041-8205/714/1/l89. URL: https://doi.org/10.1088/2041-8205/714/1/l89.

[6] E. Atkin et al. "First results of the cosmic ray NUCLEON experiment". In: *Journal of Cosmology and Astroparticle Physics* 2017.07 (July 2017), pp. 020–020. DOI: 10.1088/1475-7516/2017/07/020. URL: https://doi.org/10.1088/1475-7516/2017/07/020.

[7] H.S. Ahn et al. "The energy spectra of protons and helium measured with the ATIC experiment". In: *Advances in Space Research* 37.10 (2006). Astrophysics, pp. 1950–1954. ISSN: 0273-1177. DOI: https://doi.org/10.

1016/j.asr.2005.09.031. URL: https://www.sciencedirect.com/science/article/pii/S0273117705011233.

[8] F. Alemanno et al. "Detection of spectral hardenings in cosmic-ray boron-to-carbon and boron-to-oxygen flux ratios with DAMPE". In: *Science Bulletin* 67.21 (2022), pp. 2162–2166. ISSN: 2095-9273. DOI: https://doi.org/10.1016/j.scib.2022.10.002. URL: https://www.sciencedirect.com/science/article/pii/S2095927322004492.

[9] F. Alemanno et al. "Measurement of the Cosmic Ray Helium Energy Spectrum from 70 GeV to 80 TeV with the DAMPE Space Mission". In: *Phys. Rev. Lett.* 126 (20 May 2021), p. 201102. DOI: 10.1103/PhysRevLett.126.201102. URL: https://link.aps.org/doi/10.1103/PhysRevLett.126.201102.

[10] Y. S. Yoon et al. "Proton and Helium Spectra from the CREAM-III Flight". In: *The Astrophysical Journal* 839.1 (Apr. 2017), p. 5. DOI: 10.3847/1538-4357/aa68e4. URL: https://doi.org/10.3847/1538-4357/aa68e4.

[11] O. Adriani et al. "PAMELA Measurements of Cosmic-Ray Proton and Helium Spectra". In: *Science* 332.6025 (2011), pp. 69–72. DOI: 10.1126/science.1199172. URL: https://www.science.org/doi/abs/10.1126/science.1199172.

[12] O. Adriani et al. "Measurements of cosmic-ray proton and helium spectra with the PAMELA calorimeter". In: *Advances in Space Research* 51.2 (2013). The Origins of Cosmic Rays: Resolving Hess's Century-Old Puzzle, pp. 219–226. ISSN: 0273-1177. DOI: https://doi.org/10.1016/j.asr.2012.09.029. URL: https://www.sciencedirect.com/science/article/pii/S0273117712006199.

[13] M. Aguilar et al. "Precision Measurement of the Proton Flux in Primary Cosmic Rays from Rigidity 1 GV to 1.8 TV with the Alpha Magnetic Spectrometer on the International Space Station". In: *Phys. Rev. Lett.* 114 (17 Apr. 2015), p. 171103. DOI: 10.1103/PhysRevLett.114.171103. URL: https://link.aps.org/doi/10.1103/PhysRevLett.114.171103.

[14] M. Aguilar and et al. "Precision Measurement of the Helium Flux in Primary Cosmic Rays of Rigidities 1.9 GV to 3 TV with the Alpha Magnetic Spectrometer on the International Space Station". In: *Phys. Rev. Lett.* 115 (21 Nov. 2015), p. 211101. DOI: 10.1103/PhysRevLett.115.211101. URL: https://link.aps.org/doi/10.1103/PhysRevLett.115.211101.

[15] M. Aguilar et al. "Observation of the Identical Rigidity Dependence of He, C, and O Cosmic Rays at High Rigidities by the Alpha Magnetic Spectrometer on the International Space Station". In: *Phys. Rev. Lett.* 119 (25 Dec. 2017), p. 251101. DOI: 10.1103/PhysRevLett.119.251101. URL: https://link.aps.org/doi/10.1103/PhysRevLett.119.251101.

[16] M. Aguilar et al. "Observation of New Properties of Secondary Cosmic Rays Lithium, Beryllium, and Boron by the Alpha Magnetic Spectrometer on the International Space Station". In: *Phys. Rev. Lett.* 120 (2 Jan. 2018), p. 021101. DOI: 10.1103/PhysRevLett.120.021101. URL: https://link.aps.org/doi/10.1103/PhysRevLett.120.021101.

[17] M. Aguilar and et al. "Properties of Neon, Magnesium, and Silicon Primary Cosmic Rays Results from the Alpha Magnetic Spectrometer". In: *Phys. Rev. Lett.* 124 (21 May 2020), p. 211102. DOI: 10.1103/PhysRevLett.124.211102. URL: https://link.aps.org/doi/10.1103/PhysRevLett.124.211102.

[18] O. Adriani et al. "Observation of Spectral Structures in the Flux of Cosmic-Ray Protons from 50 GeV to 60 TeV with the Calorimetric Electron Telescope on the International Space Station". In: *Phys. Rev. Lett.* 129 (10 Sept. 2022), p. 101102. DOI: 10.1103/PhysRevLett.129.101102. URL: https://link.aps.org/doi/10.1103/PhysRevLett.129.101102.

[19] J. Chang et al. "The DArk Matter Particle Explorer mission". In: *Astroparticle Physics* 95 (2017), pp. 6–24. ISSN: 0927-6505. DOI: https://doi.org/10.1016/j.astropartphys.2017.08.005. URL: https://www.sciencedirect.com/science/article/pii/S0927650517300841.

[20] F. Alemanno et al. *Measurement of the cosmic p+He energy spectrum from 46 GeV to 316 TeV with the DAMPE space mission*. 2023. arXiv: 2304.00137 [astro-ph.HE].

[21] D. Kyratzis. "Overview of the HERD space mission". In: *Physica Scripta* 97.5 (Apr. 2022), p. 054010. DOI: 10.1088/1402-4896/ac63fc.

[22] V. F. Hess. ""Uber Beobachtungen der durchdringenden Strahlung bei sieben Freiballonfahrten". In: *Phys. Z.* 13 (1912), pp. 1084–1091.

[23] D. Pacini. "La radiazione penetrante alla superficie ed in seno alle acque". In: *Il Nuovo Cimento* 3.1 (Dec. 1912), pp. 93–100. DOI: 10.1007/BF0295744010.48550/arXiv.1002.1810. arXiv: 1002.1810 [physics.hist-ph].

[24] P. M. S. Blackett, G. P. S. Occhialini, and E. Rutherford. "Some photographs of the tracks of penetrating radiation". In: *Proceedings of the Royal Society of London. Series A, Containing Papers of a Mathematical and Physical Character* 139.839 (1933), pp. 699–726. DOI: 10.1098/rspa.1933.0048. eprint: https://royalsocietypublishing.org/doi/pdf/10.1098/rspa.1933.0048. URL: https://royalsocietypublishing.org/doi/abs/10.1098/rspa.1933.0048.

[25] C. D. Anderson. "The Apparent Existence of Easily Deflectable Positives". In: *Science* 76.1967 (1932), pp. 238–239. DOI: 10.1126/science.76.1967.238. eprint: https://www.science.org/doi/pdf/10.1126/science.76.1967.238. URL: https://www.science.org/doi/abs/10.1126/science.76.1967.238.

[26] B. Rossi. "Directional Measurements on the Cosmic Rays Near the Geomagnetic Equator". In: *Phys. Rev.* 45 (3 Feb. 1934), pp. 212–214. DOI: 10.1103/PhysRev.45.212. URL: https://link.aps.org/doi/10.1103/PhysRev.45.212.

[27] P. Auger et al. "Extensive Cosmic-Ray Showers". In: *Rev. Mod. Phys.* 11 (3-4 July 1939), pp. 288–291. DOI: 10.1103/RevModPhys.11.288. URL: https://link.aps.org/doi/10.1103/RevModPhys.11.288.

[28] W. Baade and F. Zwicky. "Remarks on Super-Novae and Cosmic Rays". In: *Phys. Rev.* 46 (1 July 1934), pp. 76–77. DOI: 10.1103/PhysRev.46.76.2. URL: https://link.aps.org/doi/10.1103/PhysRev.46.76.2.

[29] V. L. Ginzburg and S. I. Syrovatsky. "Origin of Cosmic Rays". In: *Progress of Theoretical Physics Supplement* 20 (June 1961), pp. 1–83. ISSN: 0375-9687. DOI: 10.1143/PTPS.20.1. eprint: https://academic.oup.com/ptps/article-pdf/doi/10.1143/PTPS.20.1/23001454/20-1.pdf. URL: https://doi.org/10.1143/PTPS.20.1.

[30] E. Fermi. "On the Origin of the Cosmic Radiation". In: *Phys. Rev.* 75 (8 Apr. 1949), pp. 1169–1174. DOI: 10.1103/PhysRev.75.1169. URL: https://link.aps.org/doi/10.1103/PhysRev.75.1169.

[31] E. Fermi. "Galactic Magnetic Fields and the Origin of Cosmic Radiation." In: *apj* 119 (Jan. 1954), p. 1. DOI: 10.1086/145789.

[32] G. F. Krymskii. "A regular mechanism for the acceleration of charged particles on the front of a shock wave". In: *Akademiia Nauk SSSR Doklady* 234 (June 1977), pp. 1306–1308.

[33] R. D. Blandford and J. P. Ostriker. "Particle acceleration by astrophysical shocks." In: *apjl* 221 (Apr. 1978), pp. L29–L32. DOI: 10.1086/182658.

[34] A. R. Bell. "The acceleration of cosmic rays in shock fronts – I". In: *Monthly Notices of the Royal Astronomical Society* 182.2 (Feb. 1978), pp. 147–156. ISSN: 0035-8711. DOI: 10.1093/mnras/182.2.147. eprint: https://academic.oup.com/mnras/article-pdf/182/2/147/3710138/mnras182-0147.pdf. URL: https://doi.org/10.1093/mnras/182.2.147.

[35] A. R. Bell. "The acceleration of cosmic rays in shock fronts – II". In: *Monthly Notices of the Royal Astronomical Society* 182.3 (Mar. 1978), pp. 443–455. ISSN: 0035-8711. DOI: 10.1093/mnras/182.3.443. eprint: https://academic.oup.com/mnras/article-pdf/182/3/443/3856040/mnras182-0443.pdf. URL: https://doi.org/10.1093/mnras/182.3.443.

[36] T. K. Gaisser, R. Engel, and E. Resconi. *Cosmic Rays and Particle Physics*. 2nd ed. Cambridge University Press, 2016. DOI: 10.1017/CBO9781139192194.

[37] C. Evoli. *The Cosmic-Ray Energy Spectrum*. Dec. 2020. DOI: 10.5281/zenodo.4396125. URL: https://doi.org/10.5281/zenodo.4396125.

[38] S. N. Zhang et al. "The high energy cosmic-radiation detection (HERD) facility onboard China's Space Station". In: *Space Telescopes and Instrumentation 2014: Ultraviolet to Gamma Ray*. Vol. 9144. SPIE, 2014, pp. 293–301. DOI: 10.1117/12.2055280.

[39] K. -H. Kampert et al. *Cosmic Rays in the Energy Range of the Knee - Recent Results from KASCADE –*. 2001. DOI: 10.48550/ARXIV.ASTRO-PH/0102266. URL: https://arxiv.org/abs/astro-ph/0102266.

[40] M. Aguilar et al. "Properties of Iron Primary Cosmic Rays: Results from the Alpha Magnetic Spectrometer". In: *Phys. Rev. Lett.* 126 (4 Jan. 2021), p. 041104. DOI: 10.1103/PhysRevLett.126.041104. URL: https://link.aps.org/doi/10.1103/PhysRevLett.126.041104.

[41] J. H. Han, H. S. Ahn, and Y. Amare. "Performance of the CREAM-V and CREAM-VI calorimeters in flight". In: *32nd International Cosmic Ray Conference*. Vol. 6. 2011, p. 395. DOI: 10.7529/ICRC2011/V06/1106.

[42] B. Bartoli et al. "Knee of the cosmic hydrogen and helium spectrum below 1 PeV measured by ARGO-YBJ and a Cherenkov telescope of LHAASO". In: *Phys. Rev. D* 92 (9 Nov. 2015), p. 092005. DOI: 10.1103/PhysRevD.92.092005. URL: https://link.aps.org/doi/10.1103/PhysRevD.92.092005.

[43] A. Albert et al. "Cosmic ray spectrum of protons plus helium nuclei between 6 and 158 TeV from HAWC data". In: *Phys. Rev. D* 105 (6 Mar. 2022), p. 063021. DOI: 10.1103/PhysRevD.105.063021. URL: https://link.aps.org/doi/10.1103/PhysRevD.105.063021.

[44] T. Antoni et al. "KASCADE measurements of energy spectra for elemental groups of cosmic rays: Results and open problems". In: *Astroparticle Physics* 24.1 (2005), pp. 1–25. ISSN: 0927-6505. DOI: https://doi.org/10.1016/j.astropartphys.2005.04.001. URL: https://www.sciencedirect.com/science/article/pii/S0927650505000691.

[45] M. Aglietta et al. "The cosmic ray proton, helium and CNO fluxes in the 100 TeV energy region from TeV muons and EAS atmospheric Cherenkov light observations of MACRO and EAS-TOP". In: *Astroparticle Physics* 21.3 (2004), pp. 223–240. ISSN: 0927-6505. DOI: https://doi.org/10.1016/j.astropartphys.2004.01.005. URL: https://www.sciencedirect.com/science/article/pii/S0927650504000325.

[46] J. R. Hörandel. "Models of the knee in the energy spectrum of cosmic rays". In: *Astroparticle Physics* 21.3 (2004), pp. 241–265. ISSN: 0927-6505. DOI: https://doi.org/10.1016/j.astropartphys.2004.01.004. URL: https://www.sciencedirect.com/science/article/pii/S0927650504000209.

[47] W.D. Apel et al. "Energy spectra of elemental groups of cosmic rays: Update on the KASCADE unfolding analysis". In: *Astroparticle Physics* 31.2 (2009), pp. 86–91. ISSN: 0927-6505. DOI: https://doi.org/10.1016/j.astropartphys.2008.11.008. URL: https://www.sciencedirect.com/science/article/pii/S0927650508001783.

[48] H. A. Bethe. "Passage of radiations through matter". In: *Experimental nuclear physics* (1953).

[49] Y. Yu et al. "The plastic scintillator detector for DAMPE". In: *Astroparticle Physics* 94 (2017), pp. 1–10. ISSN: 0927-6505. DOI: https://doi.org/10.1016/j.astropartphys.2017.06.004. URL: https://www.sciencedirect.com/science/article/pii/S0927650516302031.

[50] Y. Zhou et al. "A large dynamic range readout design for the plastic scintillator detector of DAMPE". In: *Nuclear Instruments and Methods in Physics Research Section A: Accelerators, Spectrometers, Detectors and Associated Equipment* 827 (2016), pp. 79–84. ISSN: 0168-9002. DOI: https://doi.org/10.1016/j.nima.2016.04.085. URL: https://www.sciencedirect.com/science/article/pii/S0168900216303023.

[51] Y. Zhang et al. "Results of heavy ion beam tests of DAMPE plastic scintillator detector". In: *Nuclear Instruments and Methods in Physics Research Section A: Accelerators, Spectrometers, Detectors and Associated Equipment* 953 (2020), p. 163139. ISSN: 0168-9002. DOI: https://doi.org/10.1016/j.nima.2019.163139. URL: https://www.sciencedirect.com/science/article/pii/S0168900219314585.

[52] T. Dong et al. "Charge measurement of cosmic ray nuclei with the plastic scintillator detector of DAMPE". In: *Astroparticle Physics* 105 (2019), pp. 31–36. ISSN: 0927-6505. DOI: https://doi.org/10.1016/j.astropartphys.2018.10.001. URL: https://www.sciencedirect.com/science/article/pii/S0927650518301786.

[53] P. Azzarello et al. "The DAMPE silicon–tungsten tracker". In: *Nuclear Instruments and Methods in Physics Research Section A: Accelerators, Spectrometers, Detectors and Associated Equipment* 831 (2016). Proceedings of the 10th International "Hiroshima" Symposium on the Development and Application of Semiconductor Tracking Detectors, pp. 378–384. ISSN: 0168-9002. DOI: https://doi.org/10.1016/j.nima.2016.02.077. URL: https://www.sciencedirect.com/science/article/pii/S0168900216002539.

[54] C. Yue et al. "Correction method for the readout saturation of the DAMPE calorimeter". In: *Nuclear Instruments and Methods in Physics Research Section A: Accelerators, Spectrometers, Detectors and Associated Equipment* 984 (2020), p. 164645. ISSN: 0168-9002. DOI: https://doi.org/10.1016/j.nima.2020.164645. URL: https://www.sciencedirect.com/science/article/pii/S0168900220310421.

[55] C. Wang et al. "Offline software for the DAMPE experiment*". In: *Chinese Physics C* 41.10 (Oct. 2017), p. 106201. DOI: 10.1088/1674-1137/41/10/106201. URL: https://dx.doi.org/10.1088/1674-1137/41/10/106201.

[56] Y.-Q. Zhang et al. "Design and on-orbit status of the trigger system for the DAMPE mission". In: *Research in Astronomy and Astrophysics* 19.9 (Sept. 2019), p. 123. DOI: 10.1088/1674-4527/19/9/123. URL: https://doi.org/10.1088/1674-4527/19/9/123.

[57] R. Brun and F. Rademakers. "ROOT: An object oriented data analysis framework". In: *Nucl. Instrum. Meth. A* 389 (1997). Ed. by M. Werlen and D. Perret-Gallix, pp. 81–86. DOI: 10.1016/S0168-9002(97)00048-X.

[58] S. Agostinelli et al. "Geant4—a simulation toolkit". In: *Nuclear Instruments and Methods in Physics Research Section A: Accelerators, Spectrometers, Detectors and Associated Equipment* 506.3 (2003), pp. 250–303. ISSN: 0168-9002. DOI: https://doi.org/10.1016/S0168-9002(03)01368-8. URL: https://www.sciencedirect.com/science/article/pii/S0168900203013688.

[59] Z. Zhang et al. "The calibration and electron energy reconstruction of the BGO ECAL of the DAMPE detector". In: *Nuclear Instruments and Methods in Physics Research Section A: Accelerators, Spectrometers, Detectors and Associated Equipment* 836 (2016), pp. 98–104. ISSN: 0168-9002. DOI: https:

//doi.org/10.1016/j.nima.2016.08.015. URL: https://www.sciencedirect.com/science/article/pii/S0168900216308336.

[60] Y. Wei et al. "Performance of the DAMPE BGO calorimeter on the ion beam test". In: *Nuclear Instruments and Methods in Physics Research Section A: Accelerators, Spectrometers, Detectors and Associated Equipment* 922 (2019), pp. 177–184. ISSN: 0168-9002. DOI: https://doi.org/10.1016/j.nima.2018.12.036. URL: https://www.sciencedirect.com/science/article/pii/S0168900218318333.

[61] W. Jiang et al. "Comparison of Proton Shower Developments in the BGO Calorimeter of the Dark Matter Particle Explorer between GEANT4 and FLUKA Simulations∗". In: *Chinese Physics Letters* 37.11 (Nov. 2020), p. 119601. DOI: 10.1088/0256-307x/37/11/119601. URL: https://doi.org/10.1088%5C%2F0256-307x%5C%2F37%5C%2F11%5C%2F119601.

[62] F. Aharonian et al. "Energy Spectrum of Cosmic-Ray Electrons at TeV Energies". In: *Phys. Rev. Lett.* 101 (26 Dec. 2008), p. 261104. DOI: 10.1103/PhysRevLett.101.261104. URL: https://link.aps.org/doi/10.1103/PhysRevLett.101.261104.

[63] F. Aharonian et al. "Probing the ATIC peak in the cosmic-ray electron spectrum with H.E.S.S.*". In: *A&A* 508.2 (2009), pp. 561–564. DOI: 10.1051/0004-6361/200913323. URL: https://doi.org/10.1051/0004-6361/200913323.

[64] M. Aguilar et al. "Precision Measurement of the $(e^+ + e^-)$ Flux in Primary Cosmic Rays from 0.5 GeV to 1 TeV with the Alpha Magnetic Spectrometer on the International Space Station". In: *Phys. Rev. Lett.* 113 (22 Nov. 2014), p. 221102. DOI: 10.1103/PhysRevLett.113.221102. URL: https://link.aps.org/doi/10.1103/PhysRevLett.113.221102.

[65] S. Abdollahi et al. "Cosmic-ray electron-positron spectrum from 7 GeV to 2 TeV with the Fermi Large Area Telescope". In: *Phys. Rev. D* 95 (8 Apr. 2017), p. 082007. DOI: 10.1103/PhysRevD.95.082007. URL: https://link.aps.org/doi/10.1103/PhysRevD.95.082007.

[66] G. Ambrosi et al. "Direct detection of a break in the teraelectronvolt cosmic-ray spectrum of electrons and positrons". In: *Nature* 552 (Dec. 2017). DOI: 10.1038/nature24475.

[67] F. Alemanno et al. "Search for gamma-ray spectral lines with the DArk Matter Particle Explorer". In: *Science Bulletin* 67.7 (2022), pp. 679–684. ISSN: 2095-9273. DOI: https://doi.org/10.1016/j.scib.2021.12.015. URL: https://www.sciencedirect.com/science/article/pii/S2095927321007672.

[68] M. Ackermann et al. "Updated search for spectral lines from Galactic dark matter interactions with pass 8 data from the Fermi Large Area Telescope". In: *Phys. Rev. D* 91 (12 June 2015), p. 122002. DOI: 10.1103/PhysRevD.91.122002. URL: https://link.aps.org/doi/10.1103/PhysRevD.91.122002.

[69] K.-K. Duan et al. "Observations of gamma-ray sources with DAMPE". In: *Proceedings of 37th International Cosmic Ray Conference — PoS(ICRC2021)*. Vol. 395. 2021, p. 631. DOI: 10.22323/1.395.0631.

[70] S. Abdollahi et al. "Fermi Large Area Telescope Fourth Source Catalog". In: *apjs* 247.1, 33 (Mar. 2020), p. 33. DOI: 10.3847/1538-4365/ab6bcb. arXiv: 1902.10045 [astro-ph.HE].

[71] T. Pierog et al. "EPOS LHC: Test of collective hadronization with data measured at the CERN Large Hadron Collider". In: *Phys. Rev. C* 92 (3 Sept. 2015), p. 034906. DOI: 10.1103/PhysRevC.92.034906. URL: https://link.aps.org/doi/10.1103/PhysRevC.92.034906.

[72] A. Tykhonov et al. "TeV–PeV hadronic simulations with DAMPE". In: *PoS* ICRC2019 (2019), p. 143. DOI: 10.22323/1.358.0143.

[73] T. T. Böhlen et al. "The FLUKA Code: Developments and Challenges for High Energy and Medical Applications". In: *Nuclear Data Sheets* 120 (2014), pp. 211–214. ISSN: 0090-3752. DOI: https://doi.org/10.1016/j.nds.2014.07.049. URL: https://www.sciencedirect.com/science/article/pii/S0090375214005018.

[74] R. Engel. "Photoproduction within the two component dual parton model. 1. Amplitudes and cross-sections". In: *Z. Phys. C* 66 (1995), pp. 203–214. DOI: 10.1007/BF01496594.

[75] S. Roesler, R. Engel, and J. Ranft. "The Monte Carlo event generator DPMJET-III". In: *International Conference on Advanced Monte Carlo for Radiation Physics, Particle Transport Simulation and Applications (MC 2000)*. Dec. 2000, pp. 1033–1038. DOI: 10.1007/978-3-642-18211-2_166. arXiv: hep-ph/0012252.

[76] A. Fedynitch. "Cascade equations and hadronic interactions at very high energies". PhD thesis. KIT, Karlsruhe, Dept. Phys., Nov. 2015. DOI: 10.5445/IR/1000055433.

[77] H. T. Dai et al. "Response of the BGO Calorimeter to Cosmic-Ray Nuclei in the DAMPE Experiment on Orbit". In: *IEEE Transactions on Nuclear Science* 67.6 (2020), pp. 956–961. DOI: 10.1109/TNS.2020.2992557.

[78] E. Thébault et al. "International Geomagnetic Reference Field: the 12th generation". In: *Earth, Planets and Space* 67, 79 (May 2015), p. 79. DOI: 10.1186/s40623-015-0228-9.

[79] A. Tykhonov et al. "Internal alignment and position resolution of the silicon tracker of DAMPE determined with orbit data". In: *Nuclear Instruments and Methods in Physics Research Section A: Accelerators, Spectrometers, Detectors and Associated Equipment* 893 (2018), pp. 43–56. ISSN: 0168-9002. DOI: https://doi.org/10.1016/j.nima.2018.02.105. URL: https://www.sciencedirect.com/science/article/pii/S0168900218302936.

[80] P.-X. Ma et al. "A method for aligning the plastic scintillator detector on DAMPE". In: *Research in Astronomy and Astrophysics* 19.6 (June 2019), p. 082. DOI: 10.1088/1674-4527/19/6/82. URL: https://doi.org/10.1088/1674-4527/19/6/82.

[81] J. B. Birks. "Scintillations from Organic Crystals: Specific Fluorescence and Relative Response to Different Radiations". In: *Proceedings of the Physical Society. Section A* 64.10 (Oct. 1951), pp. 874–877. DOI: 10.1088/0370-1298/64/10/303. URL: https://doi.org/10.1088/0370-1298/64/10/303.

[82] Y. Wei et al. "The Quenching Effect of BGO Crystals on Relativistic Heavy Ions in the DAMPE Experiment". In: *IEEE Transactions on Nuclear Science* 67.6 (2020), pp. 939–945. DOI: 10.1109/TNS.2020.2989191.

[83] G. D'Agostini. "A multidimensional unfolding method based on Bayes' theorem". In: *Nuclear Instruments and Methods in Physics Research Section A: Accelerators, Spectrometers, Detectors and Associated Equipment* 362.2 (1995), pp. 487–498. ISSN: 0168-9002. DOI: https://doi.org/10.1016/0168-9002(95)00274-X. URL: https://www.sciencedirect.com/science/article/pii/016890029500274X.

[84] M. N. Mazziotta. *A method to unfold the energy spectra of point like sources from the Fermi-LAT data*. 2009. DOI: 10.48550/ARXIV.0912.1236. URL: https://arxiv.org/abs/0912.1236.

[85] F. Loparco and M. N. Mazziotta. *Unfolding spectral analysis of the Fermi-LAT data*. 2009. DOI: 10.48550/ARXIV.0912.3695. URL: https://arxiv.org/abs/0912.3695.

[86] M. Ackermann et al. "Measurement of the high-energy gamma-ray emission from the Moon with the Fermi Large Area Telescope". In: *Phys. Rev. D* 93 (8 Apr. 2016), p. 082001. DOI: 10.1103/PhysRevD.93.082001. URL: https://link.aps.org/doi/10.1103/PhysRevD.93.082001.

[87] S. Vitillo. "Tracker charge identification and measurement of the proton flux in cosmic rays with the DAMPE experiment". eng. ID: unige:113361. PhD thesis. June 2018. URL: https://nbn-resolving.org/urn:nbn:ch:unige-1133614.

[88] A. U. Abeysekara et al. "HAWC measurements of the energy spectra of cosmic ray protons, helium and heavy nuclei in the TeV range". In: *PoS* ICRC2021 (2021), p. 374. DOI: 10.22323/1.395.0374.

[89] D. Droz et al. "A neural network classifier for electron identification on the DAMPE experiment". In: *Journal of Instrumentation* 16.07 (July 2021), P07036. DOI: 10.1088/1748-0221/16/07/P07036. URL: https://dx.doi.org/10.1088/1748-0221/16/07/P07036.

[90] A. Tykhonov et al. "A deep learning method for the trajectory reconstruction of cosmic rays with the DAMPE mission". In: *Astroparticle Physics* 146 (Apr. 2023), p. 102795. DOI: 10.1016/j.astropartphys.2022.102795. URL: https://doi.org/10.1016%5C%2Fj.astropartphys.2022.102795.

[91] M. Stolpovskiy et al. "Machine learning-based method of calorimeter saturation correction for helium flux analysis with DAMPE experiment". In: *Journal of Instrumentation* 17.06 (June 2022), P06031. DOI: 10.1088/1748-0221/17/06/P06031. URL: https://dx.doi.org/10.1088/1748-0221/17/06/P06031.

[92] Chuan Yue. *Figure provided by Dr. Chuan Yue in the DAMPE Collaboration.* Unpublished. 2022.

[93] F. Alemanno et al. "Preliminary tests of Plastic Scintillator Detector for the High Energy cosmic-Radiation Detection (HERD) experiment". In: *Journal of Physics: Conference Series* 2374.1 (Nov. 2022), p. 012120. DOI: 10.1088/1742-6596/2374/1/012120. URL: https://dx.doi.org/10.1088/1742-6596/2374/1/012120.

[94] C. Altomare et al. "Assembly and test of prototype scintillator tiles for the plastic scintillator detector of the High Energy Cosmic Radiation Detection (HERD) facility". In: *Journal of Physics: Conference Series* 2374.1 (Nov. 2022), p. 012127. DOI: 10.1088/1742-6596/2374/1/012127. URL: https://dx.doi.org/10.1088/1742-6596/2374/1/012127.

[95] C. Altomare et al. "A complete MC optical photons tracking simulation of Plastic Scintillator Detectors for the next generation of satellite experiments". In: *Journal of Physics: Conference Series* 2374.1 (Nov. 2022), p. 012050. DOI: 10.1088/1742-6596/2374/1/012050. URL: https://dx.doi.org/10.1088/1742-6596/2374/1/012050.

[96] Francesca Alemanno. *Latest results from the DAMPE space mission.* 2022. arXiv: 2209.06014 [astro-ph.HE].

[97] F. Alemanno et al. "Search for relativistic fractionally charged particles in space". In: *Phys. Rev. D* 106 (6 Sept. 2022), p. 063026. DOI: 10.1103/PhysRevD.106.063026. URL: https://link.aps.org/doi/10.1103/PhysRevD.106.063026.

[98] Francesca Alemanno and on Behalf of the DAMPE Collaboration. "The DAMPE Space Mission: Status and Main Results". en. In: *Moscow University Physics Bulletin* 77.2 (2022). Alemanno, F., on Behalf of the DAMPE Collaboration (2022). The DAMPE Space Mission: Status and Main Results. *Moscow University Physics Bulletin*, *77*(2), 280–283. https://doi.org/10.3103/S0027134922020060, pp. 280–283. ISSN: 1934-8460. DOI: 10.3103/S0027134922020060. URL: https://doi.org/10.3103/S0027134922020060.

[99] Francesca Alemanno et al. "Observations of Forbush Decreases of Cosmic-Ray Electrons and Positrons with the Dark Matter Particle Explorer". In: *The Astrophysical Journal Letters* 920.2 (Oct. 2021), p. L43. DOI: 10.3847/2041-8213/ac2de6. URL: https://dx.doi.org/10.3847/2041-8213/ac2de6.

[100] F. Alemanno et al. "Measurement of the light component (p+He) energy spectrum with the DAMPE space mission". In: *PoS* ICRC2021 (2021), p. 117. DOI: 10.22323/1.395.0117.

[101] Dimitrios Kyratzis et al. "The Plastic Scintillator Detector of the HERD space mission". In: *PoS* ICRC2021 (2021), p. 054. DOI: 10.22323/1.395.0054.

[102] ZhiHui Xu et al. "Direct Measurement of the Cosmic-Ray Iron Spectrum with the Dark Matter Particle Explorer". In: *PoS* ICRC2021 (2021), p. 115. DOI: 10.22323/1.395.0115.

[103] Peng Hu et al. "A preliminary simulation study of influence of backsplash on the plastic scintillator detector design in HERD experiment". In: *Radiation Detection Technology and Methods* (2021), pp. 1–7.

List of Figures

List of Tables

Acknowledgements

I am deeply grateful for the invaluable support provided by all the people who have helped me reach this important achievement.

I would like to thank my thesis advisor, Professor Ivan De Mitri, for his insightful advice and clear explanations, and for all the help during this thesis writing and reviewing process. Additionally, I want to thank you for introducing me to experimental particle physics (which became my passion) even before my Ph.D., and for suggesting the research described in this work, which led to writing a collaboration paper submitted together with this thesis.

Next, a big thank you to our working group at GSSI because all of you in some way took part in this journey. A special thanks goes to Andrea, Leandro, and Dimitris, who shared with me all the stressful moments, and all the work-related (and not) issues, showing that we can always find a solution if we work together and we support each other.

I am very grateful for the wonderful people I met from the first day I arrived in L'Aquila, for all the moments we spent together, and for the strength that you gave me continuously and unconditionally. I gained a lot from this piece of life that we shared, and I hope I was able to contribute to your lives in some way as well. My special thanks here goes to Tomislav, Vittoria, and Asish, for everything.

A place in my heart is dedicated to Elena, who always believed in me more than I did, in addition to being an irreplaceable friend and an amazing person. Thank you very much, and I hope our paths will cross again. I believe in you too.

I thank my family for their love and support throughout my entire life. A dedi-

cated thanks goes to Michela, who decided to join me in L'Aquila, making a piece of the family closer to me, even though far from home.

Lastly, I thank my friends at home, for being always my safe place in the world.

I couldn't mention everyone on this acknowledgments page, but I want you to know that it would have been hard without all of you. Thank you for the time you dedicated to me, for a word, a smile, and the constant feeling of not being alone in this fight.